A MEASUREMENT OF A CABIBBO-KOBAYASHI-MASKAWA MATRIX ELEMENT FROM SEMILEPTONIC DECAYS OF B MESONS TO CHARM MESONS

A Dissertation

Presented to the Faculty of the Graduate School

of Cornell University

in Partial Fulfillment of the Requirements for the Degree of

Doctor of Philosophy

by

Bonnie Lynn Valant-Spaight

August 2001

A MEASUREMENT OF A CABIBBO-KOBAYASHI-MASKAWA MATRIX ELEMENT FROM SEMILEPTONIC DECAYS OF B MESONS TO CHARM MESONS

Bonnie Lynn Valant-Spaight, Ph.D.

Cornell University 2001

We have studied the decay $D^{*0}\ell\nu$ using 3.0×10^6 $B\overline{B}$ events collected with the CLEO II detector at the Cornell Electron Storage Ring. We fully reconstruct the D^{*0} and lepton and use the angle between the D^{*0}-lepton pair and the parent B to distinguish $D^{*0}\ell\nu$ decays from other semileptonic B decays. We determine $|V_{cb}|F(1)$ and the $D^{*0}\ell\nu$ form factor parameter $\rho^2_{A_1}$ from the decay rate distribution $d\Gamma/dw$. We find $|V_{cb}|F(1) = 0.0427 \pm 0.0026 \pm 0.0023$ and $\rho^2_{A_1} = 1.54 \pm 0.18 \pm 0.25$, where the errors are statistical and systematic, respectively. Using these parameters, we derive $\Gamma(B \to D^*\ell\bar{\nu}) = 0.0400 \pm 0.0027 \pm 0.0037$, which implies a $D^{*0}\ell\nu$ branching fraction of $(6.62 \pm 0.45 \pm 0.61)\%$. From our measurement of $|V_{cb}|F(1)$ we extract $|V_{cb}| = 0.0468 \pm 0.0027 \pm 0.0025 \pm 0.0022$, where the first error is statistical, the second error is systematic, and the third error is from the theoretical error on $\mathcal{F}(1)$.

BIOGRAPHICAL SKETCH

Bonnie Valant-Spaight was born to Gary and Nancy Valant in Dallas, Texas. Her first and favorite playmate was her older brother, Michael. Growing up in the Dallas area, she attended public schools, graduating with honors from Plano East Senior High School. A great deal of her education came from her parents, from whom she learned the joy of reading, lifelong learning, and Alfa Romeos. During her high school years she was a member of the Chamberlain Ballet, a pre-professional ballet training company. She attended the Thacher Summer Science Program in Ojai, California, in 1989, a program which reinforced her desire to become a scientist.

At age 17 Bonnie met her future husband, John Tracy Spaight. She already had plans at that point to attend Texas A&M University on a Presidential Scholarship, but Tracy soon persuaded her to transfer to his school, Santa Clara University, after her freshman year. She attended SCU for three years, graduating *magna cum laude* and in the honors program with a B.S. in Physics. She was supported her final two years by a Clare Boothe Luce Scholarship. In her junior year she was inducted into Phi Beta Kappa, and in her senior year she was awarded the university's Orella Science Prize. While at SCU she pursued her love of dance as an active participant in many Department of Theatre and Dance productions. In 1994 her dance *Appassionata* was chosen to be part of the department's annual dance show.

Bonnie and Tracy were married in Texas on August 13, 1994, and the next day they left to enter graduate school at Cornell University. Bonnie's graduate school experience was marred by the loss of her father to cancer in 1996. Her father's death hurt her deeply but left her with a new appreciation of the small joys in life and the importance of spending time with loved ones. She revived her dancing "career" by joining the Ithaca Ballet in 1997, where she was privileged to choreograph three new works for the company. She received her M.S. in Physics from Cornell on May 8, 1998, which would have been her father's 54th birthday.

This work is dedicated to my mother, my husband Tracy,

and especially the memory of my father

ACKNOWLEDGEMENTS

Special thanks first go to my thesis adviser, Ritchie Patterson, for all of her help and understanding through the years. I have learned a tremendous amount from her about experimental physics, and I will always emulate her standard of excellence. Many thanks to Karl Ecklund and Bruce Berger, my partners in crime on $B \to D^* \ell \bar{\nu}$. It has been a pleasure both working with them and becoming friends. I'd also like to thank past $B \to D^* \ell \bar{\nu}$ contributer Mark Dickson for, among other things, generating my signal Monte Carlo. Thanks also go to Pablo Hopman for taking the time to make Monte Carlo for his work useful for mine as well. Also, thanks to the $B \to D^* \ell \bar{\nu}$ paper committee, consisting of David Cassel (chair), Yuichi Kubota, Mark Palmer, and Jon Thaler, for their patience and expertise. Finally, many thanks to my thesis committee members David Cassel and Peter Lepage.

Special thanks to those who were patient enough to proofread parts of this thesis: Bruce Berger, Veronique Boisvert, and Sara Keckler (whom I'm thrilled to be living near again!). Thanks also to Ritchie for her insightful comments and suggestions.

Hearty thanks to the CESR staff, without whom my work would not have been possible. Thanks also to all of the CLEO and Cornell faculty and staff, especially Persis Drell, who makes it all look so easy (and fun). And how would I have made it through without Deb Hatfield? Thank you also to Deb's family for welcoming Gretchen into their home.

CLEO is definitely a family, and I'd like to thank those mentioned above and the following members for help, friendship, and good conversations: Dan Bliss, Ken Bloom, Veronique Boisvert, Roy Briere, Dave Cinabro, Dave Crowcroft, Andy Foland, Romulus Godang, Andrei Gritsan, Jesse Ernst, Brian Heltsley, Lauren Hsu, Ye Liu, Adam Lyon, Tom Meyer, Charles Plager, Paula Pomianowski, Craig Prescott, Antonella Romano, Tony Rubiera, Gregg and Jana Thayer, and Elizabeth Young, with apologies to anyone I've left off. I am truly blessed to have made so many new friends at Wilson Lab. The skits we did at the Physics Department holiday parties and the time we devoted to Expanding You Horizons leave me with a warm glow. Special thanks and much love to Ye Liu for teaching me so much about physics and about her homeland of China. I will always trasure the years we spent cramped together in that office! (This goes for all my officemates.)

Of course, there's also life outside the lab. Thanks to everyone at the Ithaca Ballet for allowing me to choreograph and perform with them. Special thanks to the entire Fairbank clan, including Hobbes, for making Tracy, Gretchen, and me part of your family. Thanks to Narinder Dogra for giving me the once-in-a-lifetime opportunity to pose in a tutu and pointe shoes on a rock in Saguaro National Park. Thanks to everyone at Cornell Physical Therapy, which was practically my second home on campus, with special thanks to Chris McNamara for all the good care, sympathy, and wiener dog stories. Thanks also to Beth Paris, Joni Landau, and

Drs. Susan Miller and Beth Dollinger. Well-deserved thanks go to Katie Whitman for her help taking care of Gretchen when we were away.

Thanks also to all my non-lab friends for listening to what I'm sure were sometimes tedious descripitions of my problems at the lab. I'm still hoping that Craft Night will someday be revived with Suzanne Moon and Jean Donaldson (but it will always be there in spirit). Many thanks to the Donaldson Home for Wayward Scholars (and dogs) for another home-away-from-home. Thanks to Monica Plisch, a fellow new student in 1994, for giving me the perspective from the basement of Clark. Thanks to Becky Burke for being herself, and also for being such a good friend to Gretchen. Finally, thanks to my other S&TS friends Michael Dennis, Clark Miller, Karen Ellison, and Peter and Pauline Dear, with whom Tracy and I spent many a pleasant evening.

Of course I couldn't have made it to graduate school without at least a few exceptional teachers on the way. I can't imagine better high school physics teachers than Mr. Bruton and Mrs. Coe. It's been a true pleasure to have gotten to know Mrs. Patricia Irvin, my high school chemistry teacher with whom I reconnected when I became a member of Phi Beta Kappa. Love and thanks to Kathy Chamberlain, my ballet teacher in high school, who taught me what it means to persist. Thanks to my college professors Linda Brunauer, Bill Johanson, and Phil Kesten, who made Santa Clara University a wonderful place to learn.

While being included here won't mean anything to a dog (although you never know what they're up to when you're asleep), I feel I must acknowledge the huge part that my dog Gretchen, a short-haired red dachshund, played in my graduate school experience. She is always there with a lick and ready to make me smile, and she has made many a hard time easier. I hope I have taken as good of care of her as she has of me.

Words are not adequate to express thanks to my family, but I do want to mention who they are. I know I can always count on my grandparents to be my biggest fans. Thanks to Gene Vincent for his encouragement and support and for taking good care of my mother. My brother is very special to me, and he has helped me through by always being interested in what I do and by sharing the neat things that he learns. Special thanks to my husband, Tracy Spaight, for always believing in me, for broadening my horizons, and for giving me the courage to achieve my dreams. Finally, I owe a huge debt of graditude to my parents, who taught me so much by being such wonderful and interesting people. They gave me what is perhaps the most important thing a child could have, self-confidence, and they are always close in my thoughts.

TABLE OF CONTENTS

LIST OF TABLES

LIST OF FIGURES

CHAPTER 1

MOTIVATION

1.1 Introduction

This thesis describes a study of decays of the B meson to a D^* meson and leptons. The goal of this study is to measure $|V_{cb}|$, a parameter of a model that attempts to describe the interactions of all matter in the universe. More precise knowledge of this parameter will help test the validity of this model and advance our knowledge of how our universe works.

Chapter 1 describes the motivation behind our measurement of $|V_{cb}|$. Chapter 2 discusses the theoretical framework needed to make the measurement. Chapter 3 describes how our data is produced, collected, and processed so that we can reconstruct $B \to D^* \ell \bar{\nu}$ decays. Chapter 4 describes our reconstruction of $B \to D^* \ell \bar{\nu}$ decays, how we deal with backgrounds, the fit we perform to extract $|V_{cb}|$, and the results of our fit. Chapter 5 details our determination of the systematic errors on our measurement. Chapter 6 compares our measurement to other measurements of $|V_{cb}|$ and discusses the outlook for improvement on this measurement.

1.2 Weak Decays and the CKM Matrix

The weak force, which describes interactions between quarks and leptons, is one of the four fundamental forces of the Standard Model. The Standard Model is briefly described in Appendix A. The weak interactions proceed through two charged vector bosons ($W^{\pm}$) and one neutral vector boson (Z^0). Quark flavor is not conserved in weak decays, and quarks can decay across generations; for example, an s quark can decay to a u quark plus a W^-. If physical quark states were eigenstates of the weak interaction, these decays would not be allowed. Instead, the weak eigenstates must be a mixture of the mass eigenstates.

The interaction Lagrangian for charged weak processes can be written

$$\mathcal{L}_{int} = -\frac{g}{\sqrt{2}}(\mathcal{J}^{\mu} W_{\mu}^{+} + \mathcal{J}^{\mu\dagger} W_{\mu}^{-}), \tag{1.1}$$

where $\mathcal{J}^{\mu}$ is the charged weak current and couples to the charged weak boson field W_{μ}. The current is written

$$\mathcal{J}^{\mu} = \bar{u}_i \gamma^{\mu} \tfrac{1}{2}(1-\gamma_5) V_{ij} d_j, \tag{1.2}$$

where u stands for the quark states (u, c, t) and d for the quark states (d, s, b). The matrix V_{ij} describes the rotation of the physical quark states (d, s, b) to the weak eigenstates (d', s', b') and is known as the Cabibbo-Kobayashi-Maskawa (CKM) matrix [2]. Explicitly, this relationship is

$$\begin{pmatrix} d' \\ s' \\ b' \end{pmatrix} = \begin{pmatrix} V_{ud} & V_{us} & V_{ub} \\ V_{cd} & V_{cs} & V_{cb} \\ V_{td} & V_{ts} & V_{tb} \end{pmatrix} \begin{pmatrix} d \\ s \\ b \end{pmatrix}. \tag{1.3}$$

The matrix elements measure the coupling between quarks of different flavors and can be complex. The CKM matrix must satisfy the unitarity condition $VV^\dagger = 1$.

The matrix elements are inputs of the Standard Model; they are not predicted by the Standard Model and must be measured through experiment. At present only the magnitudes of the matrix elements can be measured. Only the first two rows of the CKM matrix have been measured directly; those values are [1]

$$\begin{pmatrix} 0.9735 \pm 0.0008 & 0.2196 \pm 0.0023 & 0.0036 \pm 0.0011 \\ 0.224 \pm 0.016 & 1.04 \pm 0.16 & 0.0402 \pm 0.0019 \\ - & - & - \end{pmatrix}, \tag{1.4}$$

where some values are the average of several measurements and the value for $|V_{ub}|$ actually comes from a measurement of $|V_{ub}|/|V_{cb}|$. Observations of the top quark at the CDF and DØ experiments give the following restraint on the final three elements [1]:

$$\frac{|V_{tb}|^2}{|V_{td}|^2 + |V_{ts}|^2 + |V_{tb}|^2} = 0.99 \pm 0.29. \tag{1.5}$$

The CKM matrix can be simplified from the nine parameters shown in Equation 1.3 to four independent, real parameters. This is accomplished by using the restraints of the unitarity condition and removing unphysical quark phases. One popular parameterization is the Wolfenstein parameterization [3], which divides the elements into those of order 1, λ, λ^2, and λ^3:

$$V = \begin{pmatrix} 1 - \lambda^2/2 & \lambda & A\lambda^3(\rho - i\eta) \\ -\lambda & 1 - \lambda^2/2 & A\lambda^2 \\ A\lambda^3(1 - \rho - i\eta) & -A\lambda^2 & 1 \end{pmatrix} + \mathcal{O}(\lambda^4). \tag{1.6}$$

A is a constant of order 1, and η gives the magnitude of the relative phase between the elements.

The unitarity of the CKM matrix implies that all rows and columns are orthogonal, which leads to a more convenient way to picture the unitarity condition. Taking the first and third columns of the matrix, we can write

$$V_{ud}V_{ub}^* + V_{cd}V_{cb}^* + V_{td}V_{tb}^* = 0. \tag{1.7}$$

Since V_{ud} and V_{tb} are of order 1 and $V_{cd} < 0$ (according to the Wolfenstein parameterization), we can rewrite this equation as

$$\frac{V_{ub}^*}{|V_{cd}V_{cb}|} + \frac{V_{td}}{|V_{cd}V_{cb}|} = 1, \tag{1.8}$$

which can represented as a triangle in the complex plane. Figure 1.1 shows this triangle; in term of the Wolfenstein parameterization, the corners of the triangle are at (0,0), (1,0), and (ρ,η). While this process can be used on any two rows or columns of the CKM matrix, this particular combination is one of only two triangles where the sides are all of the same order. The other triangle contains V_{ts}, but large theoretical uncertainties make it difficult to measure this element experimentally. The triangle displayed in Figure 1.1 is therefore frequently referred to as "the" unitarity triangle.

The Standard Model has been quite successful at describing observed particle physics properties, but there is still room within the current experimental uncertainties for new physics to be discovered. By measuring all the sides and angles of the unitarity triangle with increasing precision, we can make stronger tests of the actual unitarity of the CKM matrix; if the sides and angles do not make a closed

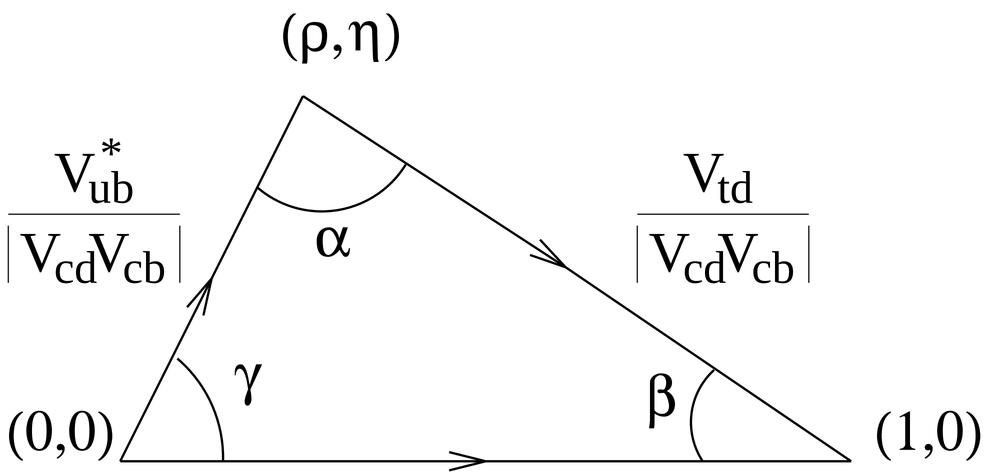

Figure 1.1: The unitarity triangle [4].

triangle, it would imply physics outside that described by the Standard Model. Also, a non-zero area of the triangle is required if CP violation, already observed in the neutral kaon system, is to be permitted within the Standard Model.

1.3 Measuring $|V_{cb}|$

$|V_{cb}|$ sets the lengths of the sides of the unitarity triangle and is therefore a quite important part of the test of unitarity. It can be measured using semileptonic B decays when the daughter meson contains a charm quark (generically referred to as $B \to X_c \ell \bar{\nu}$ decays). For mesons, semileptonic decays are weak decays in which the W emitted by the decaying quark couples to leptons while the daughter quark and the undecayed quark, called a "spectator" quark, form one or more hadrons. $B \to X_c \ell \bar{\nu}$ decays consist of $B \to D \ell \bar{\nu}$ and $B \to D^* \ell \bar{\nu}$ decays as well as modes with

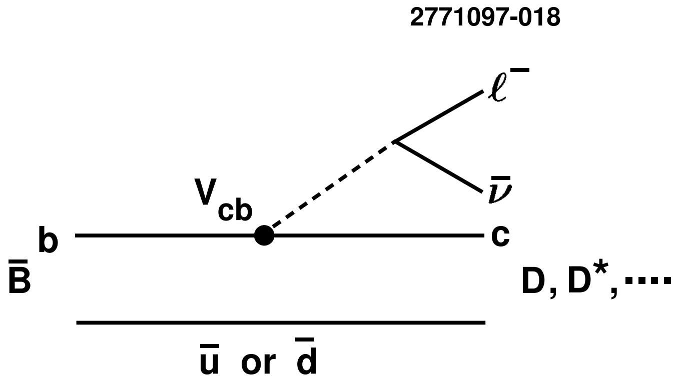

Figure 1.2: A quark diagram of semileptonic B decays to charm mesons [5].

higher excitation resonances of the D like $B \to D_2^* \ell \bar{\nu}$, and non-resonant decays such as $B \to D\pi\ell\bar{\nu}$. A quark-level diagram of a semileptonic decay of the B to a charm meson is shown in Figure 1.2. Since the b quark decays weakly to a c quark (and leptons), the decay rate will depend on $|V_{cb}|$.

Semileptonic decays are useful for measuring $|V_{cb}|$ for several reasons. The complicated hadronic component can be separated from the leptonic component, isolating the effects of the strong force. Also, when there is a single hadron in the final state will it not interact strongly with the other decay products. Experimentally, semileptonic decays tend to have relatively large branching fractions, which makes getting a sizable sample of these decays easier. Also, the single charged lepton in the final state makes for a clean signature.

Before we get into ways to extract $|V_{cb}|$ from semileptonic decays, here is a little terminology. The total rate Γ for a particle to decay is related to its lifetime by $\Gamma = \hbar/\tau$; any measurement of some subset of decays of a particle is known as a partial rate and is written with the mode next to Γ in parentheses (e.g. $\Gamma(B \to D^* \ell \bar{\nu})$). A "branching fraction" is the ratio of a partial rate for a particle to its total rate and is the probability that a particle will decay through that mode.

Several techniques exist for determining $|V_{cb}|$ from $B \to X_c \ell \bar{\nu}$ decays. "Inclusive" measurements find the partial rate $\Gamma(B \to X_c \ell \bar{\nu})$ for the sum of all $B \to X_c \ell \bar{\nu}$ decays by observing only the charged lepton. The inclusive method has the advantage that the various complicated hadronic states do not need to be separately identified, which both simplifies the detection and allows all of the semileptonic decays to be used in the measurement, decreasing the statistical uncertainty. $|V_{cb}|$ is related to the inclusive branching fraction by [4]

$$\mathcal{B}(B \to X_c \ell \bar{\nu}) = \gamma_{thy} |V_{cb}|^2 \tau_B, \tag{1.9}$$

where γ_{thy} is a constant determined from integrating the differential rate (the derivative of the rate with respect to some variable). There are substantial uncertainties on this constant from the effect of higher-order perturbative corrections, the explicit appearance of the c and b quark masses, and other sources, and it currently has an error of about 9% [6]. In addition, the rate is determined for the quark-level process $b \to c \ell \bar{\nu}$ and assumed to apply to the hadron-level process $B \to X_c \ell \bar{\nu}$. This assumption is known as quark-hadron duality, and the error from this assumption could be as high as 5%. "Exclusive" measurements reconstruct a particular mode, usually $B \to D \ell \bar{\nu}$, or $B \to D^* \ell \bar{\nu}$. $|V_{cb}|$ is extracted from measurements of either the partial rate or the differential rate. Description of the differential rate requires knowledge of the strong interaction dynamics in the decay, which is presently quite limited. Measuring $|V_{cb}|$ with an experimentally determined exclusive partial rate depends on integrating the description of the differential rate; the result is quite sensitive to the theoretical uncertainties on the differential rate. Measurements using the experimentally determined differential rate are much less sensitive to these uncertainties; however, knowledge of the normalization of the partial rate at some point is required to extract $|V_{cb}|$. The normalization suffers from an uncertainty of at least 11% for $B \to D\ell\bar{\nu}$ but only 5% [6] for $B \to D^*\ell\bar{\nu}$. The mode $B \to D^*\ell\bar{\nu}$ is also experimentally simpler than $B \to D\ell\bar{\nu}$ because its total rate is approximately three times as large due to a dependence of the differential rate on $|p_{D^*}|$ instead of $|p_D|^3$, which leads to a larger data sample in general and higher statistics at the kinematic point where $|V_{cb}|$ is measured. Also, while the $B \to D\ell\bar{\nu}$ signal will include D background from all other $B \to X_c\ell\bar{\nu}$ decays, $B \to D^*\ell\bar{\nu}$ will only have semileptonic background from $B \to X_c\ell\bar{\nu}$ decays that include a D^* or higher resonance.

It is important to measure $|V_{cb}|$ from both inclusive and exclusive decays to gain confidence in the results. In this analysis, we determine $|V_{cb}|$ from the differential decay rate of the exclusive decay $B \to D^{*0}\ell\nu$. The next chapter discusses the decay dynamics of $B \to D^*\ell\bar{\nu}$ events and how we extract $|V_{cb}|$.

CHAPTER 2

THEORY OF $B \to D^*\ell\bar{\nu}$ DECAYS

2.1 $B \to D^*\ell\bar{\nu}$ Decay Dynamics

The amplitude for $B \to D^*\ell\bar{\nu}$ decays can be written in terms of a leptonic current (L_μ) and a hadronic current (H^μ) as follows [4]:

$$\mathcal{A} = -i\frac{G_F}{\sqrt{2}}V_{cb}L_\mu H^\mu, \tag{2.1}$$

where G_F is the Fermi coupling constant. The leptonic current is calculable, but the hadronic current contains non-perturbative information about the interaction between quarks and is thus not calculable within QCD. The hadronic current is directly proportional to the matrix element of a $V - A$ charged weak current operator:

$$H^\mu = \langle D^*|V^\mu - A^\mu|B\rangle, \tag{2.2}$$

where $V^\mu = \bar{c}\gamma^\mu b$, $A^\mu = \bar{c}\gamma^\mu\gamma_5 b$, and $\langle D^*|$ and $|B\rangle$ represent the wavefunctions of the D^* and B.

2.1.1 Matrix Element

The $B \to D^* \ell \bar{\nu}$ matrix element can be parameterized in terms of the available 4-vectors in the process multiplied by form factors that include the information that is not known about the overlap of the B and $D^{(*)}$ wavefunctions. The full matrix element is written [4]

$$\begin{aligned}\langle D^*(p', \vec{\epsilon})|V^\mu - A^\mu|B(p)\rangle &= \tfrac{2i\epsilon^{\mu\nu\alpha\beta}}{m_B+m_{D^*}}\epsilon^*_\nu p'_\alpha p_\beta V(q^2) - (m_B + m_{D^*})\epsilon^{*\mu} A_1(q^2) + \\ &\quad \tfrac{\vec{\epsilon}^*\cdot\vec{q}}{m_B+m_{D^*}}(p+p')^\mu A_2(q^2) + 2m_{D^*}\tfrac{\vec{\epsilon}^*\cdot\vec{q}}{q^2} q^\mu A_3(q^2) - \\ &\quad 2m_{D^*}\tfrac{\vec{\epsilon}^*\cdot\vec{q}}{q^2} q^\mu A_0(q^2), \qquad (2.3)\end{aligned}$$

where p' and $\vec{\epsilon}$ are the 4-momentum and polarization of the D^*, respectively, p is the 4-momentum of the B, $q^2 = (p - p')^2$ is the squared momentum transfer of the process, and V, A_0, A_1, A_2, and A_3 are the form factors.[1] Three of the form factors are related by

$$A_3(q^2) = \tfrac{m_B+m_{D^*}}{2m_{D^*}} A_1(q^2) - \tfrac{m_B-m_{D^*}}{2m_{D^*}} A_2(q^2), \qquad (2.4)$$

and the condition $A_0(0) = A_3(0)$ is imposed to avoid a pole at $q^2 = 0$.

Some general assumptions can be made about the form factors from kinematic considerations. Figure 2.1 shows a schematic representation of the two extremes of q^2 at the quark level. Part (a) shows the B meson in its rest frame before decay, with the small circles representing the two quarks confined in the larger circle of the meson. Part (b) shows the result of a decay $b \to c\ell\bar{\nu}$ at $q^2 = q^2_{max}$, where the lepton and neutrino travel in opposite directions away from the meson and

[1] For $B \to D^* \ell \bar{\nu}$, q^2 ranges from 0 to 10.7 $(\mathrm{GeV}/c^2)^2$.

the c quark stays at rest relative to the rest frame of the B. The wave function of the spectator quark requires minimal change to keep the two quarks bound together in a meson, which in our case is a D^*, so the form factors have their maximum values. Part (c) shows a decay at $q^2 = q^2_{min}$, where the lepton and neutrino travel in the same direction. In this case, the c quark must recoil against the lepton-neutrino pair and has the most momentum with respect to the B rest frame. Since the c quark is traveling away from the spectator quark, the spectator quark wavefunction requires maximum change, so the form factors must have their smallest values. More specific knowledge of the form factors is important for our determination of $|V_{cb}|$; this can be derived from QCD relations and is discussed in Section 2.2.

2.1.2 Differential Decay Rate

In general, the decay rate of a process is related to its amplitude by "Fermi's Golden Rule":

$$\Gamma = \tfrac{2\pi}{\hbar}|\mathcal{A}\mathcal{A}^*|\rho_f, \tag{2.5}$$

where Γ is the decay rate and ρ_f describes the phase space of the process. In the limit of zero lepton mass, which is a good approximation for electrons and muons, the operator q_μ will give zero when multiplied by the leptonic current L^μ, as it is in $\mathcal{A}$ (Equation 2.1). The matrix element can then be treated as containing only the first three terms, and the resultant decay rate depends only on the form factors V, A_1, and A_2.

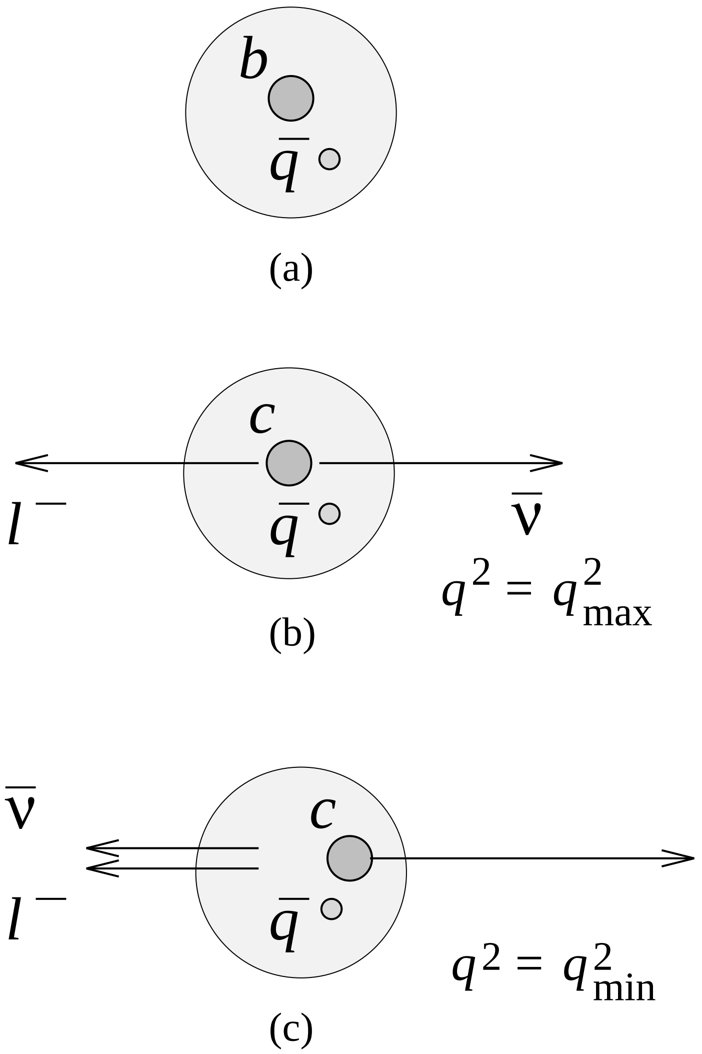

Figure 2.1: Kinematic extremes for B semileptonic decays [4]. (a) The rest frame of the B meson; (b) The system after semileptonic decay in which the c quark is a rest relative to the B rest frame; (c) The system after semileptonic decay in which the c quark has the maximum velocity relative to the B rest frame.

The differential decay rate for $B \to D^* \ell \bar{\nu}$ is given by [7]

$$\frac{d\Gamma}{dq^2} = \frac{G_F^2 |V_{cb}|^2}{96\pi^3} |\vec{p}_{D^*}| \frac{q^2}{m_B^2} (|H_+|^2 + |H_-|^2 + |H_0|^2). \tag{2.6}$$

The H's are the invariant helicity amplitudes and in the zero lepton mass limit are related to the form factors by [8]

$$H_0 = \frac{1}{2m_{D^*}\sqrt{q^2}} [(m_B^2 - m_{D^*}^2 - q^2) A_1(q^2) + 2m_B^2 p^2 A_2(q^2)], \tag{2.7}$$

$$H_\pm = A_1(q^2) \pm m_B p V(q^2), \tag{2.8}$$

where p is the momentum of the D^* in the B rest frame.

The normalization of the differential decay rate depends directly on $|V_{cb}|$, so if we can predict the value of the form factors at any point, we can measure $|V_{cb}|$ from the experimentally-determined normalization of $d\Gamma/dq^2$ at that point. Heavy Quark Effective Theory, introduced in the next section, gives us just such a prediction.

2.2 Determining the $B \to D^* \ell \bar{\nu}$ Form Factors and $|V_{cb}|$

While the exact masses of the six quark flavors are not known, the relative size of their masses can be characterized. Compared with the scale factor $\Lambda_{QCD} \sim 0.2$ GeV, the u, d, and s quarks are considered "light," while the c, b, and t quarks are considered "heavy." Heavy Quark Effective Theory (HQET) uses the assumption that the heavy quarks are infinitely massive to predict the normalization of the $B \to D^* \ell \bar{\nu}$ form factors at a specific point. In this section, first HQET and its implications for the measurement of $|V_{cb}|$ from $B \to D^* \ell \bar{\nu}$ decays are discussed.

We then discuss further results on the form factors which are required to measure $|V_{cb}|$.

2.2.1 HQET and the Isgur-Wise Function

In $B \to D^*\ell\bar{\nu}$ decays, the heavy b quark in the B meson decays to leptons and another heavy quark (c) that forms a meson with the spectator light quark. In the limit that the mass of the heavy quarks gets infinitely large ($m_Q \to \infty$), the light degrees of freedom can be thought of as a cloud surrounding the heavy quarks. This cloud is sometimes called the 'brown muck', a term invented by Isgur. The gluons that couple to the brown muck carry momenta of order Λ_{QCD}. In the limit $m_Q \to \infty$, where m_Q becomes much larger than Λ_{QCD}, the gluons are not sufficiently energetic (i.e. their wavelength is too long) to identify the quantum numbers of the heavy quark, which has a Compton wavelength inversely proportional to its mass. The brown muck can therefore only be affected by heavy quark attributes that act at large distances, which means that the light quark will only see the heavy quark's color field and not its flavor (mass) or spin.

With the mass symmetry implied by HQET, q^2 is no longer the optimal variable to use when describing $B \to D^*\ell\bar{\nu}$ decay dynamics. In the limit $m_Q \to \infty$, the velocity of the daughter heavy quark is unaffected by the rearrangement of the light degrees of freedom and therefore remains the same as the velocity of the original heavy quark, making the velocity of the heavy quark a conserved quantity in the decay. The velocity of the heavy quark is also nearly equal to the velocity of the meson(s). For these reasons, it is convenient to rewrite the matrix elements in terms of the available 4-velocities. The form factors become functions of $w = v \cdot v'$, where v is the 4-velocity of the B and v' is the 4-velocity of the D^*. There is a close relationship between q^2 and w; for $B \to D^* \ell \bar{\nu}$, they are related by

$$w = \frac{m_B^2 + m_{D^*}^2 - q^2}{2 m_B m_{D^*}}. \tag{2.9}$$

The $B \to D^* \ell \bar{\nu}$ form factors and differential decay rate are reformulated as follows. The differential decay rate is written as [7]

$$\begin{aligned} \frac{d\Gamma}{dw} &= \frac{G_F^2}{48\pi^3}(m_B - m_{D^*})^2 m_{D^*}^3 \sqrt{w^2-1}(w+1)^2 \times \\ & \left[1 + 4\left(\frac{w}{w+1}\right)\left(\frac{1-2wr+r^2}{(1-r)^2}\right)\right] \left[|V_{cb}| F(w)\right]^2 \end{aligned} \tag{2.10}$$

where $r = m_{D^*}/m_B$ and the form factor $F(w)$ is given by

$$F(w) = \sqrt{\frac{\tilde{H}_0^2 + \tilde{H}_+^2 + \tilde{H}_-^2}{1 + 4\left(\frac{w}{w+1}\right)\left(\frac{1-2wr+r^2}{(1-r)^2}\right)}} h_{A_1}(w). \tag{2.11}$$

The $\tilde{H}_i$ are the helicity form factors and are given by

$$\tilde{H}_0(w) = 1 + \frac{w-1}{1-r}\left(1 - \frac{h_{A_3}(w) + r h_{A_2}(w)}{h_{A_1}(w)}\right), \tag{2.12}$$

$$\tilde{H}_\pm(w) = \frac{\sqrt{1-2wr+r^2}}{1-r}\left(1 \mp \sqrt{\frac{w-1}{w+1}} \frac{h_V(w)}{h_{A_1}(w)}\right). \tag{2.13}$$

These new form factors are related to the traditional form factors by [4]

$$\frac{2\sqrt{m_B m_{D^*}}}{m_B + M_{D^*}} V(q^2) = h_V(w), \tag{2.14}$$

$$\frac{m_B + m_{D^*}}{2\sqrt{m_B m_{D^*}}} A_1(q^2) = \frac{w+1}{2} h_{A_1}(w), \tag{2.15}$$

$$\frac{2\sqrt{m_B m_{D^*}}}{m_B + M_{D^*}} A_2(q^2) = h_{A_3}(w) + \frac{m_{D^*}}{m_B} h_{A_2}(w). \tag{2.16}$$

The mass and spin symmetries have implications for the $B \to D^* \ell \bar{\nu}$ form factors. The spin symmetry tells us that in the limit $m_Q \to \infty$, h_{A_2} goes to zero and the other form factors all become equal to one "universal" form factor [9]:

$$h_V(w) = h_{A_1}(w) = h_{A_3}(w) = \xi(w). \tag{2.17}$$

The function $\xi(w)$ is called the Isgur-Wise function and is the universal form factor for these decays. The mass symmetry gives us some information about the Isgur-Wise function at a particular kinematic point. To the brown muck, replacing a b quark with a c quark traveling at equal velocity will have no effect, since the brown muck cannot know the difference between heavy quark flavors. If the c quark has a different velocity, the brown muck will have to rearrange itself to compensate. This tells us two things about the Isgur-Wise function: (1) It is normalized at zero recoil ($\xi(1) = 1$), and (2) at $w = 1$, the first derivative must be negative ($\xi'(1) = -\rho^2$).

Let us first assume that the heavy quarks are actually infinitely heavy and see how this allows us to measure $|V_{cb}|$. First, it is convenient to define the form factor ratios $R_1(w)$ and $R_2(w)$ [7]:

$$R_1(w) = \frac{h_{A_3}(w)+rh_{A_2}(w)}{h_{A_1}(w)}, \tag{2.18}$$

$$R_2(w) = \frac{h_V(w)}{h_{A_1}(w)}. \tag{2.19}$$

In the limit $m_Q \to \infty$, both $R_1(w)$ and $R_2(w)$ go to 1, which in turn means that $\mathcal{F}(w)$, defined in Equation 2.11, becomes equal to $\xi(w)$. Since we know $\xi(1) = 1$, it should be a simple matter to measure $d\Gamma/dw$ at $w = 1$ and extract $|V_{cb}|$. Unfortunately, phase space goes to zero at $w = 1$ and so does $d\Gamma/dw$. All is not lost, however; bounds can be set on $\xi(w)$ from non-perturbative methods (e.g. lattice

QCD, QCD sum rules, and dispersion relations) leading to a parameterization of $\xi(w)$ in terms of ρ^2 and w [7]. We can then fit the measured $d\Gamma/dw$ distribution, allowing $|V_{cb}|$ and ρ^2 to be free parameters.

2.2.2 Corrections for Non-Infinite Quark Mass

Since the quarks are not actually infinitely massive and the mass of the c quark is not particularly large compared to Λ_{QCD}, corrections must be made to the normalization at $w = 1$, and we cannot use the Isgur-Wise function for $\mathcal{F}(w)$. We go back to $R_1(w)$ and $R_2(w)$, which are defined such that they are expected to vary weakly with w, and $h_{A_1}(w)$. Instead of measuring ρ^2, the slope of $\xi(w)$ at $w = 1$, we measure the slope of $h_{A_1}(w)$ at $w = 1$, which we refer to as $\rho^2_{A_1}$. We also must know the normalization of $h_{A_1}(w)$ at $w = 1$, which can be predicted using corrections to the infinite-mass limit.

Caprini, Lellouch, and Neubert use dispersion relations and analyticity to bound $h_{A_1}(w)$ [10]. These bounds are translated into the following form factor parameterization:

$$h_{A_1}(w) \;=\; h_{A_1}(1)[1 - 8\rho^2_{A_1} z + (53\rho^2_{A_1} - 15)z^2 - (231\rho^2_{A_1} - 91)z^3], \quad (2.20)$$

where $z = (\sqrt{w+1} - \sqrt{2})/(\sqrt{w+1} + \sqrt{2})$. The authors estimate the uncertainty on these functions to be less than 2%. Boyd, Grinstein, and Lebed have made a similar calculation [11] and get results that are consistent within 3%.

$R_1(w)$ and $R_2(w)$ have been both calculated and measured. Using QCD sum rules and applying short-distance corrections, $R_1(1)$ and $R_2(1)$ are found to have the values 1.27±0.1 and 0.8±0.2, respectively, where the errors are estimated [7]. This method also gives the predictions [7]

$$R_1(w) = R_1(1) - 0.12(w-1) + 0.05(w-1)^2, \tag{2.21}$$

$$R_2(w) = R_2(1) + 0.11(w-1) - 0.06(w-1)^2. \tag{2.22}$$

CLEO [12] has measured $R_1(w)$ and $R_2(w)$ assuming that they are constant and that $h_{A_1}(w)$ is linear in w. CLEO found

$$R_1 = 1.18 \pm 0.30 \pm 0.12, \tag{2.23}$$

$$R_2 = 0.71 \pm 0.22 \pm 0.07, \text{ and} \tag{2.24}$$

$$-\tfrac{dh_{A_1}}{dw}(w=1) \equiv \rho^2_{A_1} = 0.91 \pm 0.15 \pm 0.06 \tag{2.25}$$

with the correlation coefficients $C(\rho^2_{A_1}, R_1) = 0.60$, $C(\rho^2_{A_1}, R_2) = -0.80$ and $C(R_1, R_2) = -0.82$. The calculated and measured values are in good agreement.

At $w = 1$, $h_{A_1}(1) = \mathcal{F}(1)$. Corrections to $\mathcal{F}(1)$ come from the finite QCD renormalizations of the flavor-changing axial currents at $w = 1$, QED corrections, and power corrections in terms of Λ_{QCD}/m_Q. Luke's Theorem [13] protects $\mathcal{F}(1)$ from first-order power corrections, a significant advantage of $B \to D^*\ell\bar{\nu}$ decays over $B \to D\ell\bar{\nu}$ decays, which are not protected. Uncertainties on $\mathcal{F}(1)$ come from higher-order perturbative corrections on the QCD renormalization and the uncertainties on the power corrections. We will use [6]

$$\mathcal{F}(1) = 0.913 \pm 0.042, \tag{2.26}$$

where the (theoretical) uncertainties have been added linearly to give a conservative estimate.

We measure $d\Gamma(B \to D^* \ell \bar{\nu})/dw$ using $B^- \to D^{*0} \ell^- \bar{\nu}$ and charge conjugate decays. We fit the $d\Gamma(B \to D^* \ell \bar{\nu})/dw$ distribution using the parameterizations given in Equations 2.20, 2.21, and 2.22. We use the values of R_1 and R_2 from the CLEO measurement as our values of $R_1(1)$ and $R_2(1)$ and allow as free parameters $|V_{cb}|F(1)$ and $\rho^2_{A_1}$. We then use the predicted value of $\mathcal{F}(1)$ to extract $|V_{cb}|$. By integrating the decay rate over w using the values of $|V_{cb}|F(1)$ and $\rho^2_{A_1}$, we can also extract the total rate of $B \to D^* \ell \bar{\nu}$ decays. The remainder of this thesis describes our measurement.

CHAPTER 3

PARTICLE CREATION, DETECTION, AND RECONSTRUCTION

In order to study the decays of B particles, we must have a sample of them. We must also have some way to detect and identify the decay particles. The Cornell Electron-positron Storage Ring, or CESR (pronounced like the famous Roman), gives us our supply of B's. It is located on the campus of Cornell University, in a circular tunnel 40 feet underground, and started operation in 1979. We detect the decay products of the B's in the CLEO II[1] detector, which collected data from 1989 to 1995.

This chapter gives a brief description of CESR in Section 3.1 and of the CLEO II detector in Section 3.2. The acquisition of data from CLEO II is described in Section 3.3. Section 3.4 describes the reconstruction of events from the raw data. The identification of particles in described in Section 3.5. Finally, Section 3.6 describes how we simulate the detector.

[1]There is no official explanation of this acronym, which was apparently chosen to coordinate with CESR.

3.1 CESR

B particles are a rare find in today's universe. Because they are short-lived, having a lifetime of about 1.6 ps, any B's that are created in nature (for instance by high-energy cosmic rays) do not stick around for long before decaying. If we want to study them, then, we must first create some. We do this by accelerating electrons and positrons up to more than 5 GeV of energy and colliding them with CESR. A schematic of the machines used to do this is shown in Figure 3.1.

In concept, creating massive particles from light particles is simple. The equivalence of mass and energy tells us that if we collide a particle-antiparticle pair of particles with a little mass but a lot of momentum (hence a lot of energy), we can get out of that collision a pair of particles with a lot of mass but little momentum. The difficulty lies in the details, which in this case are left in the capable hands of the CESR staff. They are responsible as much as anyone for the data that we analyze.

As the name suggests, CESR collides electrons and positrons, but CESR itself actually does not accelerate the electrons and positrons up to the energies needed to create B's. The process starts in a linear accelerator, known as the linac. At the very beginning of the linac, an electrode is heated to emit electrons. These electrons are accelerated down a 30 cm pipe through a series of strong electric fields. The electrons come out of the end of the linac with about 300 MeV of energy. Assuming a constant electric field throughout the length of the pipe, this means that the electrons reach 90% of the speed of light in just 3.9 cm! To create

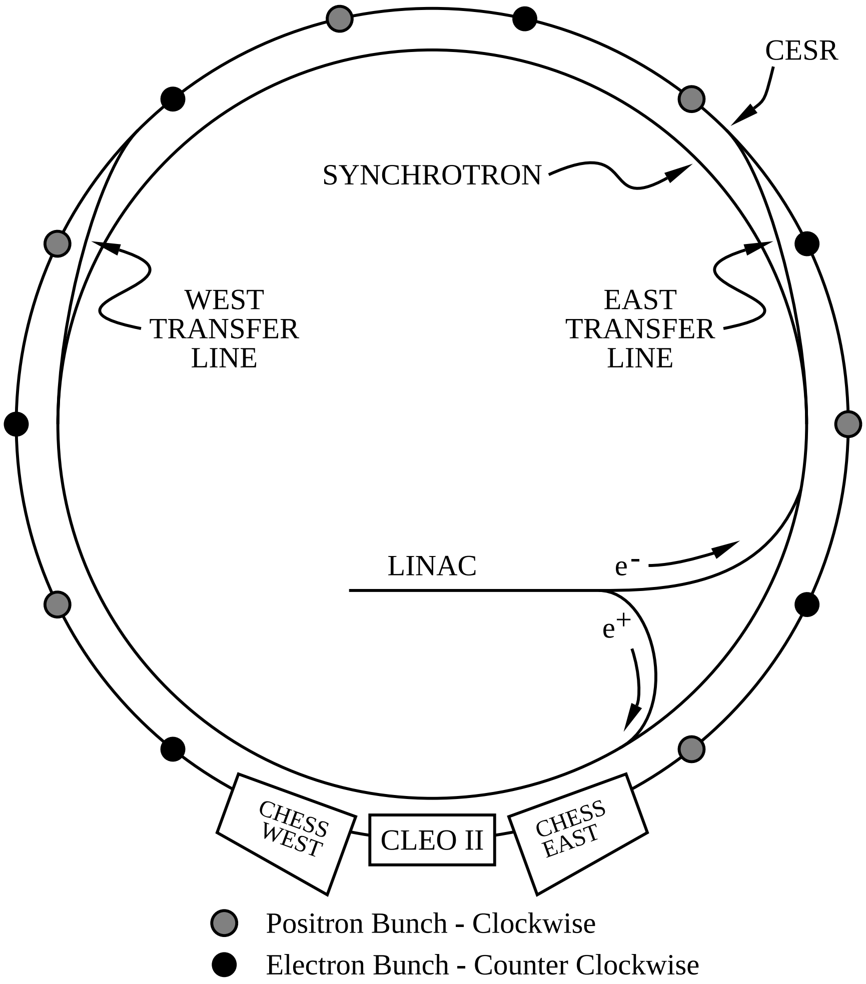

Figure 3.1: A schematic view of CESR.

positrons, electrons with about 140 MeV of energy are directed into a tungsten target. The resulting collisions produce electrons, positrons, and X-rays. The positrons are then siphoned off down the rest of the linac and are accelerated to an energy of 200 MeV.

From the linac, the electrons or positrons are injected into the synchrotron. The job of the synchrotron is to raise the energy of the particles from a few hundred MeV to more than 5 GeV. The synchrotron consists of 192 bending magnets and 4 linear accelerating sections, all of which sit along the inner wall of the underground tunnel. The bending magnets create simple dipole magnetic fields to bend the trajectory of the particles in a circle of fixed radius (i.e. the tunnel). The radius of curvature of a charged particle's path in a magnetic field can be expressed as $R = p/qB$, where R is the radius of curvature, p is the momentum of the particle, q is its charge, and B is the field strength. As the energy of the particles increases, so does their momentum; in order to keep the particles moving with a particular radius of curvature, the magnetic field must increase, and that increase must be synchronized with the momentum increase. It is from this synchronization that the synchrotron takes its name. It takes about 4000 revolutions in the synchrotron to get the particles up to the energy required to make B particles, 5.29 GeV. All of these revolutions take place in less than one hundredth of a second, and just before they are injected into CESR the particles are traveling at 99.9999995% of the speed of light.

The purpose of CESR is both to keep the positrons and electrons at a particular energy and to collide them at a particular place. Like the Synchrotron, CESR consists of many magnets and a few accelerating sections lined up along the outer wall of the tunnel. These magnets surround a pipe that runs the length of the ring, called the “beam pipe” because it contains the particle beam. The beam pipe lies in a circle with a circumference of 768 m. In addition to 86 dipole bending magnets, CESR contains 106 quadrupole “focusing” magnets. Since the particles do not enter CESR with uniform energy or direction, most of them have paths that would eventually lead them to collision with the wall of the beam pipe. The focusing magnets focus the beam of particles in much the same way a concave lens focuses a beam of light. Unlike a lens, however, the quadrupole magnetic field actually focuses in one direction (for instance side to side) and defocuses in the other direction (up and down). In addition, particles that are originally turned away from one side of the beam pipe will eventually make their way to the other side if not redirected. Many quadrupole magnets are therefore required, arranged so that each magnet is rotated 90 degrees around the beam pipe compared to the magnets on either side of it. This arrangement causes the beam to be alternately focused and defocused in each direction, with the cumulative effect that the particles stay away from the beam pipe walls. CESR also has sextupole and octupole magnets, which focus the momentum distribution of the beam.

Unlike the synchrotron, the accelerator sections in CESR do not increase the energy of the particles. Instead, these sections allow CESR to maintain the energy of the particles. Each particle on average loses 1.2 MeV of energy per revolution in the form of X-rays, which are known as “synchrotron radiation” because they are a by-product of bending charged particles in a magnetic field. These X-rays are emitted tangential to the beam and the majority run into the outer wall of the beam pipe, which must be cooled, but since they are well-collimated and can be produced over a substantial amount of time, they are a valuable tool themselves. At certain points in the ring, the X-rays are allowed to go off into experimental stations. This setup is known as the Cornell High Energy Synchrotron Source, or CHESS, and scientists from all over the world use the synchrotron radiation to do research in the areas of physics, chemistry, biology, environmental science, and material science.

When starting from scratch, first positrons are created in the linac, accelerated in the synchrotron, and then injected into CESR. Unlike the synchrotron, CESR must contain both types of particles at once. Once the appropriate number of positrons is in the ring, the acceleration and injection process is repeated with electrons, with the electrons injected so they travel the opposite way around the ring. Since electrons and positrons have the same mass, they would normally travel the same path, or "orbit", around the ring. This would lead to electron-positron collisions all along the length of the beam pipe, which means that the collisions we are so interested in and have gone to so much trouble to cause would not happen where we have a detector set up to record them. To prevent these collisions, electrostatic separators are included to make the electrons and protons travel slightly different paths; these paths are called "pretzel orbits" because the electron and positron paths weave around each other. The beam pipe is also kept under a vacuum of 10^{-8} torr to prevent interactions with air or other particles.

The electrons and positrons are allowed to collide only at the “interaction point”, which is at the center of the CLEO II detector.

The particles in the CESR beams are not evenly distributed. Instead, there are nine groups of particles, called trains, evenly spaced around the ring. Each train is made up of some number of bunches of particles. When CLEO II started taking data, there was only one bunch in each train. Towards the end of data-taking with CLEO II, in November of 1994, a bunch was added to each train, making a total of 18 bunches. Currently, CESR runs in what is known as “9×4” running, which means 9 trains of 4 bunches each. Grouping the bunches this way helps with the timing of the data readout, which is discussed below. It also allows for more particles to be put into CESR, thus increasing the frequency of collision. Each collision is generally referred to as an “event.”

The number of collisions is measured using instantaneous luminosity, which is defined as

$$\mathcal{L} = fn\frac{N_{e^+}N_{e^-}}{A}, \tag{3.1}$$

where f is the frequency of revolution of the particles, n is the number of bunches, N_{e^+} and N_{e^-} are the number of positrons and electrons in each bunch, respectively, and A is the cross-sectional area of the beams. At the interaction point, each bunch is 2 cm long, 0.3 mm wide, and 8μm high. The current record for instantaneous luminosity for CESR is $1.2\times10^{33}/\mathrm{cm}^2\mathrm{s}$. The total number of collisions that occur is measured by integrating the instantaneous luminosity over time.

3.1.1 The Υ Resonances

Although CESR was designed to run over a range of energies, during CLEO II data taking it ran primarily at a center-of-mass energy (E_{cm}) of 10.58 GeV. At this energy the e^+e^- collisions sometimes produce a bound state of a b and $\bar{b}$ quark known as the $\Upsilon(4S)$ resonance, which decays 100% of the time to a $B\overline{B}$ pair. As the name implies, the $\Upsilon(4S)$ is the third excited state of this bound pair. CLEO was the first experiment to resolve the $\Upsilon(1S)$, $\Upsilon(2S)$, and $\Upsilon(3S)$ resonances [14] and the first to observe the $\Upsilon(4S)$ [15].

The $\Upsilon(4S)$ is the lowest-energy state of the Υ that produces $B\overline{B}$ pairs. The $\Upsilon(3S)$, with a mass of 10.36 GeV/c^2 [1], does not have enough mass (energy) to decay to two B particles, which together have a mass of 10.56 GeV/c^2 [1]. The $\Upsilon(4S)$, however, has just enough mass at 10.58 GeV/c^2 [1] to decay to a $B\overline{B}$ pair. It is frequently assumed in B branching fraction measurements that the branching fraction for the $\Upsilon(4S)$ to decay to B^+B^- (referred to as f_{+-}) and $B^0\bar{B}^0$ (f_{00}) are equal. A recent CLEO measurement confirmed this assumption at the 8% level (cite Sylvia), but the ratio f_{+-}/f_{00} has been predicted to be as high as 1.18 [17].

Figure 3.2 shows the cross-section (which is related to probability) of $e^+e^- \to$ *hadrons* for the energy range of the first four resonances. Notice that the Υ resonance peaks sit on a hadronic background. This background is referred to as "continuum background" and mostly consists of $e^+e^- \to q\bar{q}$ events, where q stands for a u, d, s, or c quark (which are all quarks lighter than the b quark). Also included are $e^+e^- \to \tau^+\tau^-$ events where one or both of the τ's decays hadronically. The amount of continuum background scales as $1/E_{cm}^2$. Some continuum events are difficult to distinguish from $B\overline{B}$ events and must be subtracted using a process described below. Other background processes that exist are $e^+e^- \to e^+e^-$ (Bhabha [2] events) and $e^+e^- \to \mu^+\mu^-$ (μ-pairs); cross-sections for these backgrounds are much higher than the cross-section for hadronic events, but are easy to distinguish from $B\overline{B}$ events.

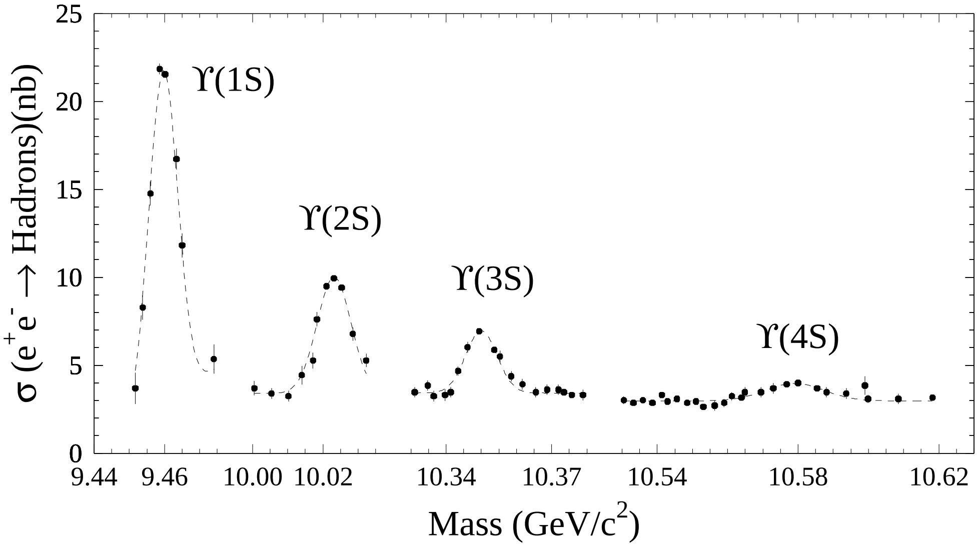

Figure 3.2: The first four Υ resonances.

The ratio of Fox-Wolfram moments H_2/H_0 [18] gives us some handle on vetoing continuum events. This ratio contains information about the shape of an event. $\Upsilon(4S) \to B\bar{B}$ events tend to be isotropic, or "spherical," with particles carrying energy in all directions; the $\Upsilon(4S)$ is produced and decays at rest and each daughter

[2]Named after Indian physicist Homi Jehangir Bhabha (1909-1966), who made significant contributions to the understanding of the production of electron-positron pairs from cosmic rays.

B meson is produced with a momentum of about 0.3 GeV$/c$. In a continuum event, the mass of the quark pair is much lower than E_{cm}, so the daughter particles of these quarks' hadronization have higher momenta than the B's. These events tend to have a more "jetty" appearance; that is, the energy in the event tends to be distributed back-to-back. The ratio of Fox-Wolfram moments H_2/H_0 measures how jetty an event is, assigning spherical events numbers closer to zero, and jetty events numbers closer to one, with 98% of$B\bar{B}$ events containing $D^{*0}\ell\nu$ decays having H_2/H_0 values less than 0.4.

Requiring small H_2/H_0 removes some but not all continuum events from on-resonance data samples. The rest of the events are subtracted using a pure sample of continuum events. At energies just below the $\Upsilon(4S)$ resonance, only continuum processes generate hadronic events, and these events are very much like the continuum events produced at the $\Upsilon(4S)$ energy. Because the cross-section for continuum events is about four times the cross section for $\Upsilon(4S)$ at $E_{cm} = 10.58$ GeV, CESR must spend a substantial amount of time running below the $\Upsilon(4S)$ resonance energy to collect a large enough sample of continuum events. CESR usually spends two-thirds of the time running "on-resonance" at $E_{cm} = 10.58$ GeV and one-third of the time running "off-resonance" at $E_{cm} = 10.52$ GeV.

3.2 The CLEO II detector

Making B particles is not enough; in order to learn anything about them, we also must observe them, which is the purpose of the CLEO II detector. CLEO II was installed from 1988 to 1989 and began taking data in late 1989. While CLEO II is referred to as "a detector," it is actually a collection of many different types of detectors. A cross-section of CLEO II is shown in Figure 3.3. As particles travel out radially from the beam pipe, they encounter the following detectors, in order: the Precision Tracker, the Vertex Detector, the Outer Drift Chamber, the Time of Flight Detector, the Electromagnetic Calorimeter, also called the Crystal Calorimeter, and the Muon Detector. The Precision Tracker, Vertex Detector, and Outer Drift Chamber are often referred to together as the "tracking chambers" because they are used to reconstruct the path a particle follows through the detector. A superconducting magnet coil provides a 1.5 T magnetic field inside all detectors except the Muon Detector. Since CLEO II has been described in great detail elsewhere [19], each component is only briefly described below.

We adopt the following coordinate system when describing CLEO II. The polar angle θ is defined with respect to the direction of the electrons at the interaction point, also known as the z axis. Using a cylindrical coordinate system, r represents the distance from the beam line, and $\phi = 0$ points horizontally in the northward direction at the interaction point. CLEO II is symmetric with respect to θ; on a large scale, it is also symmetric in ϕ. "Layer" refers to components arranged cylindrically around the z axis; these are stacked radially.

The first object a particle encounters as it moves away from the interaction point is not actually a detector; it is the CESR beam pipe, which must extend inside CLEO II so that the vacuum within the beam pipe can be maintained. The

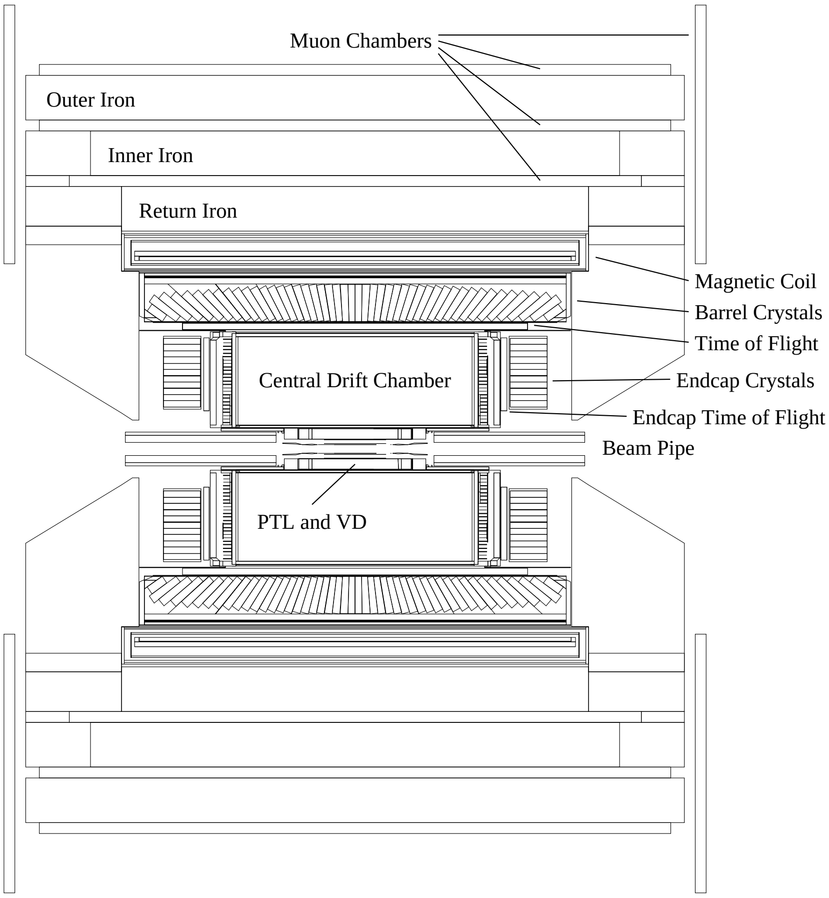

Figure 3.3: A side view of the CLEO II detector.

beam pipe section inside the detector is made of beryllium and has a thickness of 0.5 mm and a radius of 3.5 cm.

3.2.1 Precision Tracker

The Precision Tracker (PT) sits just outside of the beam pipe, in the region 3.5 cm to 7.5 cm (radial). It is made up of 6 layers of "straw tubes", which are aluminized mylar tubes with a gold-plated tungsten wire running through the center. There are a total of 384 straw tubes in the PT. The tubes, which vary in diameter, are arranged in the pattern shown in Figure 3.4 by the label "PTL." The tubes are held in this pattern by two endplates made of G-10 plastic. Gas flows through the tubes; originally this gas was a mixture of 50% argon and 50% ethane, but in April 1992 it was switched to dimethyl ether, which produces better position resolution.

The PT uses ionized electrons and an electric field to detect particles. The wires in the tubes are held at high voltage, and the tubes are held at ground, which produces an electric field within the tube in a direction that pushes electrons toward the wire. A charged particle traveling through the tube ionizes some of the gas particles in the tube. The liberated electrons follow the electric field and drift toward the wire, picking up speed as they go. Close to the wire, the electrons pick up enough speed to ionize more gas particles, which then ionize more gas particles in a chain reaction known as an "avalanche". When the electrons reach the wire, they produce a measurable current in the wire, which is read out. The wires are known as "sense wires" since they indirectly detect particles passing through. Note that only charged particles can be detected with this technique, since only they can ionize the gas particles. The signal from the sense wires, including time and accumulated charge (pulse height) are read out at one end. The PT can only give information about the $r - \phi$ position of a particle and none on its position in z.

3.2.2 Vertex Detector

The Vertex Detector (VD) sits directly outside the PT in the region 7.5 cm to 17.5 cm. It operates on the same basic principle as the PT. The VD's major components are wires and cathodes. The wires are strung between two G-10 endplates. There are 800 nickel-chromium sense wires making up 10 layers. 2,272 aluminum field wires are arranged to make hexagonal cells around the sense wires; the field wires shape the electric field, taking the place of the tubes in the PT. The two cathodes are made of sheets of mylar to which aluminum foil has been applied. The foil is segmented in ϕ and z into separate "pads." The inner cathode sits just inside the innermost layer of wires, and the outer cathodes sits just outside the outermost layer of wires. Figure 3.4 shows the arrangement of the wires and cathodes. The entire VD volume is filled with a 50-50 mixture of argon and ethane.

Like the PT, the sense wires in the VD are held at high voltage. The field wires are held at ground to make the electric field around the sense wire. The cathodes are also held at ground and shape the electric field for the first and last sense wire layers. Unlike the PT, the VD measures information about a particle's position in z as well as the $r - \phi$ plane. The sense wires are read out at both ends, and a particle's z position can be determined from the different amount of charge that accumulates at each end of the wire (known as the "charge division" method).

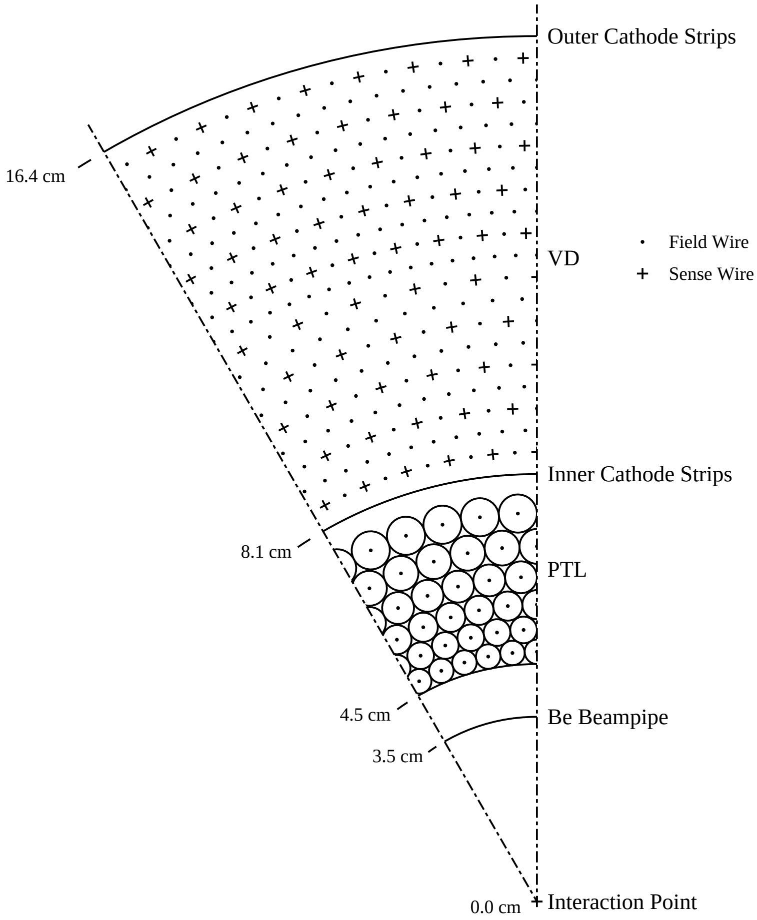

Figure 3.4: The arrangement of wires and cathodes in the Precision Tracker and the Vertex Detector.

The cathodes are also used to determine z position. When a particle induces a negatively-charged avalanche on a sense wire near a cathode, a negative "image charge" of the ion cloud develops on the cathode pads nearest the avalanche. The z position of the avalanche and hence the particle is determined by analyzing the distribution of charge on the pads.

3.2.3 Outer Drift Chamber

The Outer Drift Chamber (DR) is set up very much like the VD, with a few differences. It occupies the region 17.5 cm to 95.0 cm and consists of sense wires, field wires, and cathodes. The arrangement of the wires and cathodes is shown in Figure 3.5. There are 12,240 gold-plated tungsten sense wires arranged in 51 layers with 36,240 field wires arranged around them. The field wires around the inner 40 layers are made of gold-plated aluminum, with the remainder made of gold-plated copper-beryllium. The wires are strung between two aluminum endplates, each 3.175 cm thick. The endplates are manufactured flat but bow inwards at smaller radii due to the enormous tension provided by the 48,480 wires. The endplates are held apart at their outer edge by a cylinder of composite panels. The wires are insulated from the endplates with plastic bushings. The cathodes have the same construction and position relative to the wires as in the VD. The sense wires are held at high voltage, and the field wires and cathodes are held at ground. The DR volume is filled with a 50-50 mixture of argon and ethane.

Because of the large number of sense wires in the DR, it is impractical to read the wires out at both ends to obtain z information. Instead, eleven sense layers

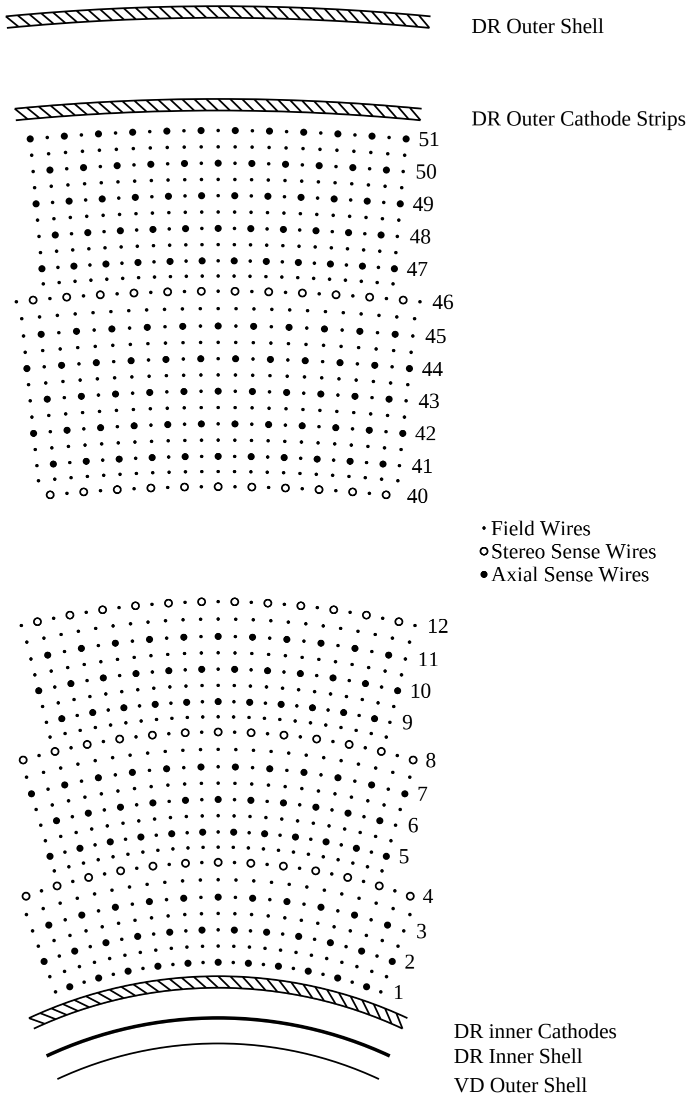

Figure 3.5: The wire pattern of the Outer Drift Chamber.

of the DR are strung slightly crooked, not quite parallel with the z axis, with their ends offset in ϕ. The $r-\phi$ position of the wire is therefore a function of z. The offset layers are known as "stereo" layers because they give three-dimensional information about the particle's position. The 40 layers strung parallel to the z axis are known as "axial" layers. To determine the z position of the particle at the stereo layers, first the particle's $r-\phi$ position at the stereo layers is predicted using the axial layers. Then the z position of the particle is determined by where along the wire the $r-\phi$ information from the stereo wire matches the $r-\phi$ information of the axial layers.

Information from the PT, the VD, and the DR is used together to determine the paths that charged particles traveled through the detector. A pattern-recognition algorithm goes through all the $r-\phi$ and z information and essentially "connects the dots" to find tracks. Figure 3.6 shows a schematic $r-\phi$ view of the PT, VD, and DR, with open and closed dots representing data points from a typical event. The lines drawn connecting the dots show the reconstruction of particles' paths through the detector, known as "tracks." The closed dots have been used to reconstruct tracks. The momentum resolution for reconstructed tracks is approximately

$$\left(\frac{\sigma_{p_t}}{p_t}\right)^2 = (0.0015p_t)^2 + (0.0055)^2, \tag{3.2}$$

where p_t is the track's momentum (in GeV/c) in the $r-\phi$ plane. For particles with momentum of 2 GeV/c, this gives a resolution of 0.6%. The angular resolution of tracks is 1 mrad in ϕ and 4 mrad in θ. These tracks tell us a particle's charge, from which way they curl due to the magnetic field, and momentum, but by themselves they tell nothing more. Particle identification, which is determining what type of particle created a track, is discussed in Section 3.5.

3.2.4 Time of Flight Detector

The Time of Flight detector (TF) sits just outside the tracking chambers. It is divided into two parts to provide better solid angle coverage. The “barrel” section sits just outside the DR and is so named because of the cylindrical arrangement of the components. It consists of 64 blocks, also called counters,[3] of a special plastic (Bicron BC-408, which has polyvinyltoluene as a base) that has been doped to make it scintillate, or emit light, when particles pass through it. The counters are 2.8 m long, 10 cm wide, and 5 cm thick and cover the region $36° < \theta < 144°$. The light signal is read out on each end by phototubes, which are connected to the counters with lucite light pipes. The “endcap” section sits outside of the endplates of the DR, at 1.175 m from the interaction point. There are 28 counters on each end of the DR. The endcap counters are shaped like truncated pie pieces; they are 58 cm long, 5 cm thick, and vary in width from 6.4 cm to 19.6 cm. They cover the regions $15° < \theta < 36°$ and $144° < \theta < 165°$. The endcap counters are read out with phototubes attached directly to the narrow ends of the counters. All counters

[3] One of the earliest uses of detectors in particle physics was as “coincidence” detectors, where one would put two detectors next to or on top of each other and look for simultaneous signals that implied the passage of a particle through the detectors. One would count the events and so the detectors were referred to as “counters”; the name has stuck.

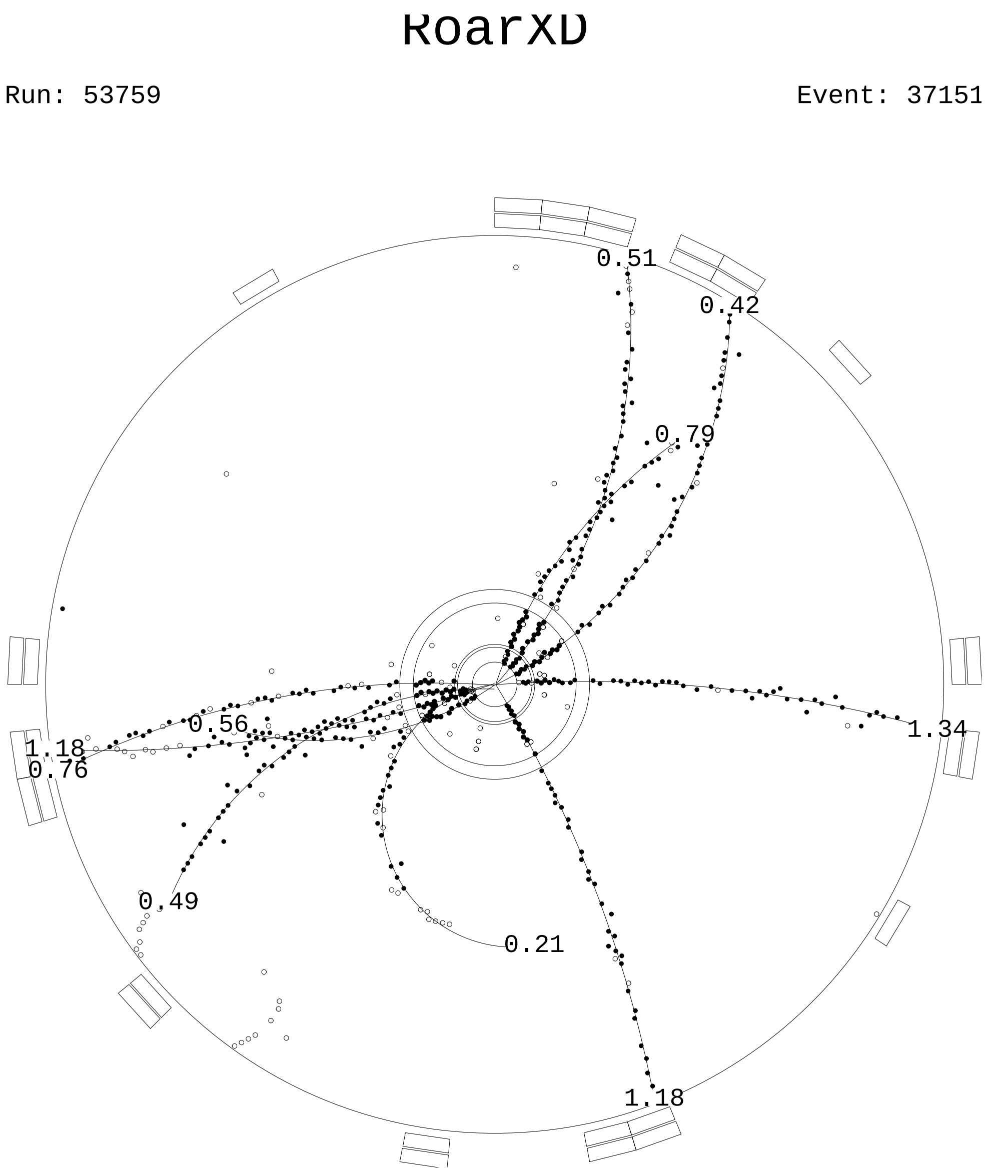

Figure 3.6: An $r-\phi$ view of data in the CLEO tracking chambers.

are wrapped in aluminum foil and then electrical tape. The TF provides 97% solid angle coverage.

When a charged particle travels through a TF counter, the counter emits light, with the maximum emission at 425 nm. The light travels down the counter to the phototube(s), where the time of arrival is read out along with the pulse height. If a track reconstructed in the tracking chambers is found to travel through a counter with a signal above threshold, the track is used to determine where in z the particle passed through the counter. The amount of time it took the signal to travel from where the track entered the counter to the end of the counter is calculated using the distance the light traveled along the counter and the speed of light in the scintillator. This quantity is subtracted from the signal's time of arrival at the phototube. The end product is the amount of time it took for the track to arrive at the counter from the interaction point, or the "time of flight," which then becomes associated with the matched track. In the barrel counters, the time-of-flight measurements from the two phototubes are averaged to get one measurement. The resolution of the barrel TF is about 170 ps; the endcap resolution is slightly worse because the counters are only read out at one end and because there is more material for particles to interact with between the interaction point and the counters.

3.2.5 Electromagnetic Calorimeter

The Electromagnetic, or Crystal, Calorimeter (CC) sits outside the TF. It consists of 7,800 thallium-doped cesium iodide crystals, all of which are approximately

30 cm long and 5 cm by 5 cm square. Like the TF, it is divided into barrel and endcap sections. The barrel section is made up of 6,144 crystals in the region $32^\circ < \theta < 148^\circ$. The crystals are placed such that their long axis points slightly away from the interaction point in order to reduce gaps between the crystals through which particles can travel. As z increases, the crystals must tip over more to point towards the interaction point, so the shape of the crystals changes slightly. The crystals are set in 48 z rows, with 128 crystals arranged azimuthally in each row. The endcap sections consist of 828 identical rectangular crystals on each end of the detector, all of which sit horizontally along the z direction. The endcap crystals overlap slightly in z with the barrel crystals, covering the regions $15^\circ < \theta < 36^\circ$ and $144^\circ < \theta < 165^\circ$. The endcap and barrel sections together provide 95% solid angle coverage.

Like the TF, the CC crystals scintillate, but in the CC the phenomenon is used differently. The density of CsI is much higher than polyvinyltoluene: 4.53 g/cm^2 versus 1.032 g/cm^2. This higher density makes it more probable that particles will lose energy in the calorimeter through processes such as ionization, scattering, bremsstrahlung (radiation emitted when a charged particle decelerates), pair production (the production of an electron-positron pair from a photon), and nuclear interaction. The particles initiate a chain reaction of interactions and decays known as a “shower.” Electron and photon showers are contained within the crystals, so all of their energy is measured, giving the detector its name. Hadron showers travel much further radially, depositing energy in the magnet coil and beyond. Muons, which are minimum-ionizing particles, usually travel through the calorimeter undisturbed. The showers produce scintillation light in the crystals, which is detected by four silicon photodiodes mounted on the end of each crystal.

Showers are reconstructed using the amount of light detected in each crystal. First the amount of light is converted to the amount of energy deposited in that crystal. Next, clusters of adjacent and near-adjacent crystals with energies above threshold are located. The highest-energy crystal in each cluster must have a signal above 10 MeV. Then the energy and position of the shower are determined from the cluster signals. The shower energy is the sum of the energies in the contributing crystals. This energy is corrected based on studies of $e^+e^- \to e^+e^-\gamma$ (radiative Bhabha) and $e^+e^- \to \gamma\gamma\gamma$ events, where it is known that the energy of the three particles must add up to twice the beam energy. The photon energy resolution is 3.8% at 100 MeV and 1.5% are 5 GeV in the barrel. The position of the shower is calculated as the energy-weighted mean of the position of the center of each crystal in the cluster;[4] energy-dependent corrections are applied to this position. The angular resolution for barrel photon showers is 11 mrad at 100 MeV and 3 mrad at 5 GeV.

3.2.6 Superconducting Magnet and Muon Detector

The 1.5 T magnetic field in most of CLEO II allows for the determination of particle charge. This magnetic field is produced with a large superconducting coil, which sits outside the barrel calorimeter. The coil has a diameter of 3 meters and is 3.5 m in length. It carries a current of 3,300 amps, storing 25 MJ of energy, and is cooled

[4]This is somewhat like finding the center of mass of a solid.

down to superconducting temperatures with liquid helium. The coil produces a field uniform to $\pm 0.2\%$ over 95% of the DR volume. The field is monitored with an NMR probe that sits a few centimeters beyond the end of the DR. Three layers of iron 36 cm thick sit outside the coil and channel the looping magnetic field lines.

The barrel muon detectors (MU) extend from $43^\circ < \theta < 137^\circ$. The detectors sit between and outside of the magnet return iron layers. The detector components operate much like the tracking chambers. Each section is 5 m long, 8.3 cm wide, and 1.0 cm tall and is oriented with its long axis parallel to the z axis. The sections are divided into eight separate volumes with a piece of plastic that runs the length of the section and has a comb-like profile. The plastic is coated with graphite to provide a field cage on three sides for silver-plated copper-beryllium wires which run down the center of each of the eight channels. Orthogonal copper pickup strips, similar in idea to the VD and DR cathodes, provide the fourth side of the field cage and give z information. The wires are held at high voltage, and the volume is filled with a 50-50 mixture of argon and ethane. The wires are read out at both ends and use charge division to give more z information. This type of drift chamber is known as a "plastic streamer counter." The counters are placed in layers of three at 36, 72, and 108 cm in the magnet return iron. Endcap muon counters sit outside the return yoke and increase the total solid angle coverage of the muon detector to 85%. The spatial resolution of the muon detector is 4.6 cm (5.7 cm) for particles which reach the middle (outer) layer of barrel counters.

3.3 Data Acquisition

With electrons and positrons traveling near the speed of light, not much time elapses between bunch crossings as the bunches travel around the CESR ring. Electron and positron trains pass each other with a frequency of 390 kHz such that with 9 trains the crossing frequency is about 3.5 MHz. Although not every crossing produces a collision, the rate is still far too high for the data acquisition system to read out every event; in addition, not every event is of interest. The events which we would like to record (where an $\Upsilon(4S)$ is created) happen at the rate of a few Hz. CLEO II has a system, called the trigger system, that examines each event as it happens and determines if it should be written out. This system is driven by the timing system, which coordinates the readout of events with the crossing time of electron and positron bunches. This timing system enables, disables, and resets readout from detector components, based on results of the trigger system. The trigger system is designed to detect primarily $B\overline{B}$ events, but some Bhabha and μ-pair events are saved for calibrating the detector.

The trigger operates on several levels, where each level uses more complicated information from the detector. One level must be passed before the trigger system examines the next level; in the event of a failure, the system goes back to ground zero. The first level, called L0, looks at data from the VD, TF, and CC. L0 takes about 30 ns to make a decision, slowing the data-taking rate to about 20 kHz. If L0 is passed, the gates to the detector electronics are disabled so that no new data are put in the short-term memory. The next level, L1, looks at DR data as well as data used by L0. It takes about 1 μs and slows the rate to 25 Hz. The last level, L2, slows the rate to a few Hz. L2 takes 30-50 μs and makes use of tracking information from the VD and DR. If L2 is satisfied, the data from that event are written out to disk. The efficiency of the trigger for choosing $B\overline{B}$ events is 99.8% and for choosing events where at least one B decays to $D^*\ell\nu$ is essentially 100%.

There are over 28,000 sensitive elements (e.g. sense wires) in CLEO II, for each of which several quantities must be recorded. Since generally the particles produced in the event reach only a small fraction of the channels, writing out the information recorded by each channel would be a waste of storage space. Channels are only written out if they have recorded a signal that falls over a certain threshold and within a certain time window determined by the timing system; in the CC the channel must also be near another activated channel that passes an energy cut. This weeding out is known as "sparsification." In addition, events read out to disk are analyzed with a program (called `level3` in reference to the trigger) that rejects more events before they are permanently recorded. In the end, CLEO II recorded about 27 million hadronic events.

3.4 Event Reconstruction

The raw data recorded from CLEO II must be processed to reconstruct tracks and showers as well as various higher-level information, such as the particle identity of tracks and showers. The program that processes the data is called `pass2` and is a collection of separate processors. The output of `pass2` is usually stored in what is known as `ROAR` format, which takes up significantly less storage space than the raw data. This section describes the output variables of `pass2` that we use to identify and reconstruct $B \to D^* \ell \bar{\nu}$ decays.

Figure 3.7 shows a data event that has been processed by `pass2`. All detectors are shown in cross-section except the CC, where each barrel crystal is represented by a rectangle in a view that approximates looking at the inside of a tin can. The raw signals are represented as dots (tracking chambers and MU), open rectangles (TF), filled-in rectangles (CC), or bars (MU). The reconstructed tracks are represented by lines; the number at the end of each tracks is its momentum in GeV/c. The number by each shower is its measured energy in GeV. The squares seen in the DR represent endcap crystal hits; endcap TF hits are not shown.

We can not directly detect B's with CLEO II, because B's are short-lived and decay to other particles within the beam pipe. Some of these decay particles are also short-lived and decay further. The six types of particles that are most frequently directly detected by CLEO II are photons, electrons, muons, pions (charged), kaons (charged), and protons. Many processors repeatedly analyze the same hits assuming that a different kind of particle (e, μ, π, K, or p) created the signal and let the user choose which assumption she prefers. Most other particles, including π^0's, and D^{*0}'s, are reconstructed from the signals of their daughter particles.

The basics of tracking were discussed at the end Section 3.2.3. The first processors used to find tracks are `TRIO` [21] and `DUET`. These processors are designed to find all possible tracks, and they often find two tracks where only one particle

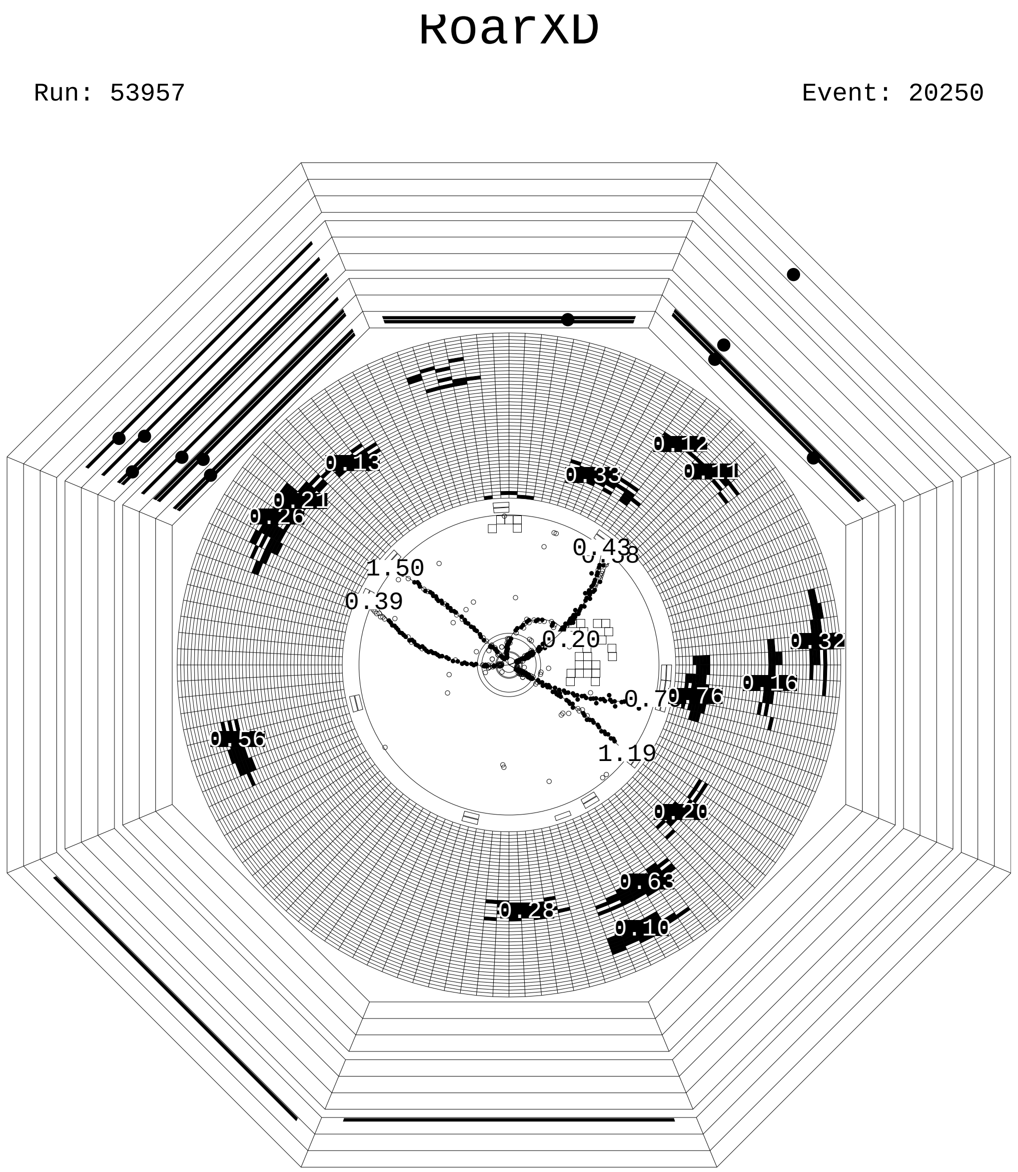

Figure 3.7: A data event showing track momentum and shower energy.

passed[5] or a track where no particles passed. The TMNG[6] processor [22] examines the output of TRIO and DUET and rejects many duplicate and fake tracks. Although we have other ways of removing the contribution to our $B \to D^* \ell \bar{\nu}$ signal from fake tracks, TMNG is useful in reducing the number of background events that we must deal with.

One other processor runs on the tracks to improve momentum reconstruction. TRIO and DUET reconstruct tracks assuming that they follow perfectly helical paths. As particles travel through the tracking chambers they lose energy through ionization and other interactions with the material in the tracking chambers. The radius of curvature of their path decreases as they slow down. By assuming a helical path, TRIO and DUET end up using a radius of curvature that is too large at the outer edge of the DR and too small at the inner edge of the PT, leading to an incorrect projection of the particle's momentum at the interaction point. The KLMN processor [23] takes into account this change in curvature; it outputs five sets of track parameters, one for each possible particle type, because the different particle types lose energy differently.

[5] An example of this can be seen in Figure 3.7 if one looks carefully; the track pointing a little below the 1 o'clock position has two labels at the end (the 0.43 covers up much of the 0.58), which indicates that two tracks were found.

[6] TMNG stands for TrackMan the Next Generation, and yes, it really is after the TV show.

3.5 Particle Identification

3.5.1 Particle Identification with Specific Ionization

The difference in energy loss which requires `KLMN` to output five sets of parameters can be exploited for particle identification. The amount of energy a particle loses through ionization per unit length, called dE/dx, depends on $\beta = v/c$, where v is the particle's speed and c is the speed of light. Particles which have the same momentum will have different values of β if they have different masses and therefore will lose different amounts of energy. The amount of charge deposited on the wires in the drift chamber is proportional to the dE/dx of the particle; by examining the mean value of the charge deposited on wires by a particular track, we can determine dE/dx for that particle. Figure 3.8 shows dE/dx versus momentum for tracks in the drift chamber. The lines represent the mean values of dE/dx for the different particle types, and the points are values from data tracks; the data for electrons are not shown because they would obscure the other distributions. While the distributions of K and π particles are clearly separated in the momentum range $0.25\,\mathrm{GeV}/c < p < 0.5\,\mathrm{GeV}/c$, they merge fairly quickly as momentum increases. Since most of the π's and K's that we reconstruct in this analysis have momentum greater than 0.5 GeV/c, we do not make use of the dE/dx information for π and K candidates; however, as seen in Figure 3.8, dE/dx continues to offer us some discrimination for electrons and is used in electron identification, described below.

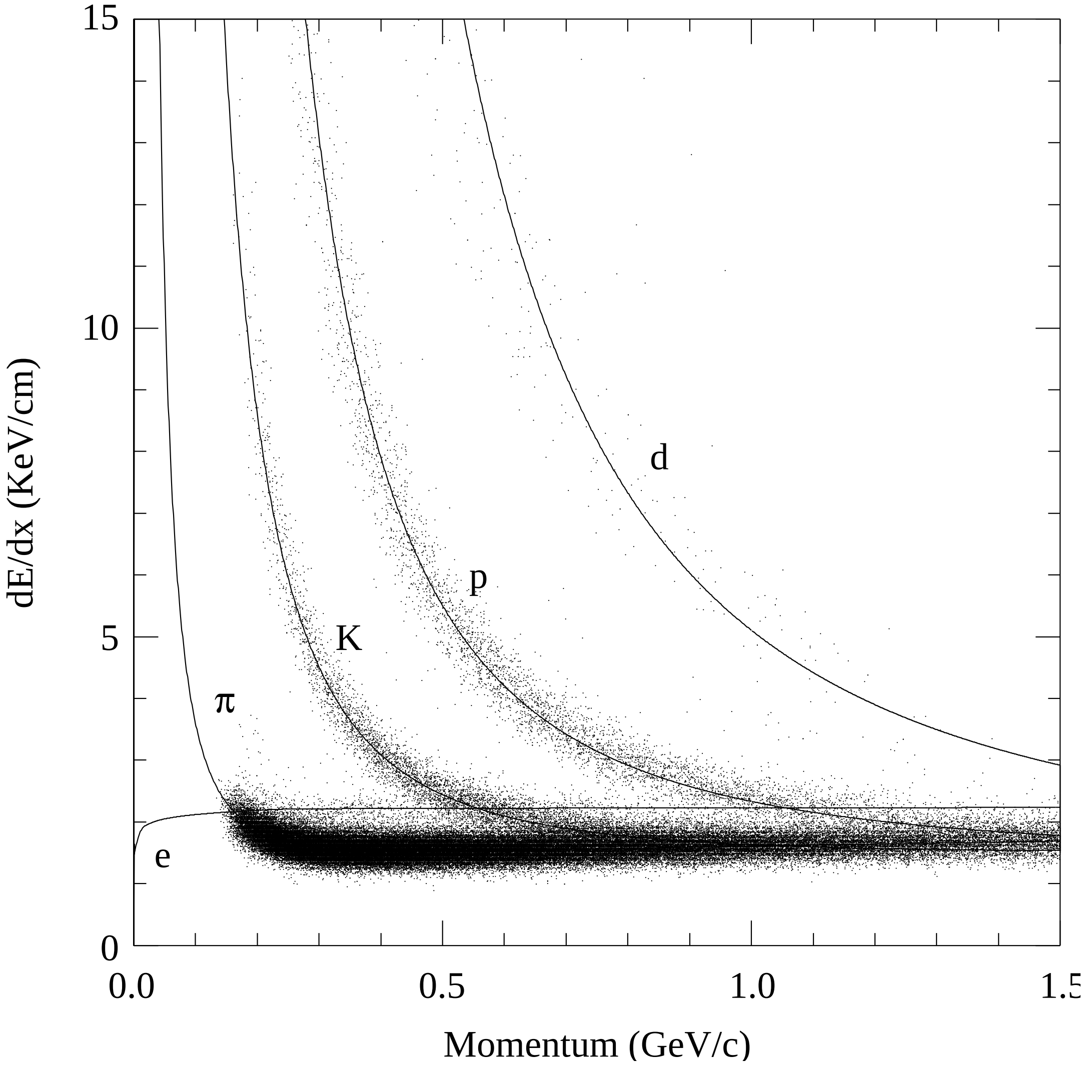

Figure 3.8: The dE/dx distribution versus momentum for particles in the DR.

3.5.2 Particle Identification through Time of Flight

The TF detector exists primarily for particle identification and works on a principle similar to that used for dE/dx measurements. The TF measures each particle's time of arrival at the detector. From this time and the distance the particle traveled to get there, derived from the track information, the particle's β (speed) is determined. As mentioned above, particles with the same momentum but different mass will have different β's; this can be seen in Figure 3.9, which shows $1/\beta$ versus momentum, where β has been determined in the TF. The lines represent the ideal value of $1/\beta$ for the different particle types; again electron data points are not shown. The TF measurements can separate K's and π's up to a slightly higher momentum than dE/dx, about 0.6 GeV/c, but again we choose not to use these measurements for K and π candidates. The TF data offer further discrimination of electrons from other particle types and are also used in electron identification.

3.5.3 Photon Identification

The CC is the only detector that detects photons. We use the processor `CCFC` to reconstruct showers in the manner discussed in Section 3.2.5. Electromagnetic showers, which are showers produced by photons or electrons, generally have a different energy distribution than hadronic showers. The ratio of the energy measured in the nine crystals surrounding and including the highest-energy crystal (a 3×3 crystal square) to the energy measured in the 25 surrounding crystals (a 5×5 crystal square) is known as `E9/E25`. Electromagnetic showers tend to have most

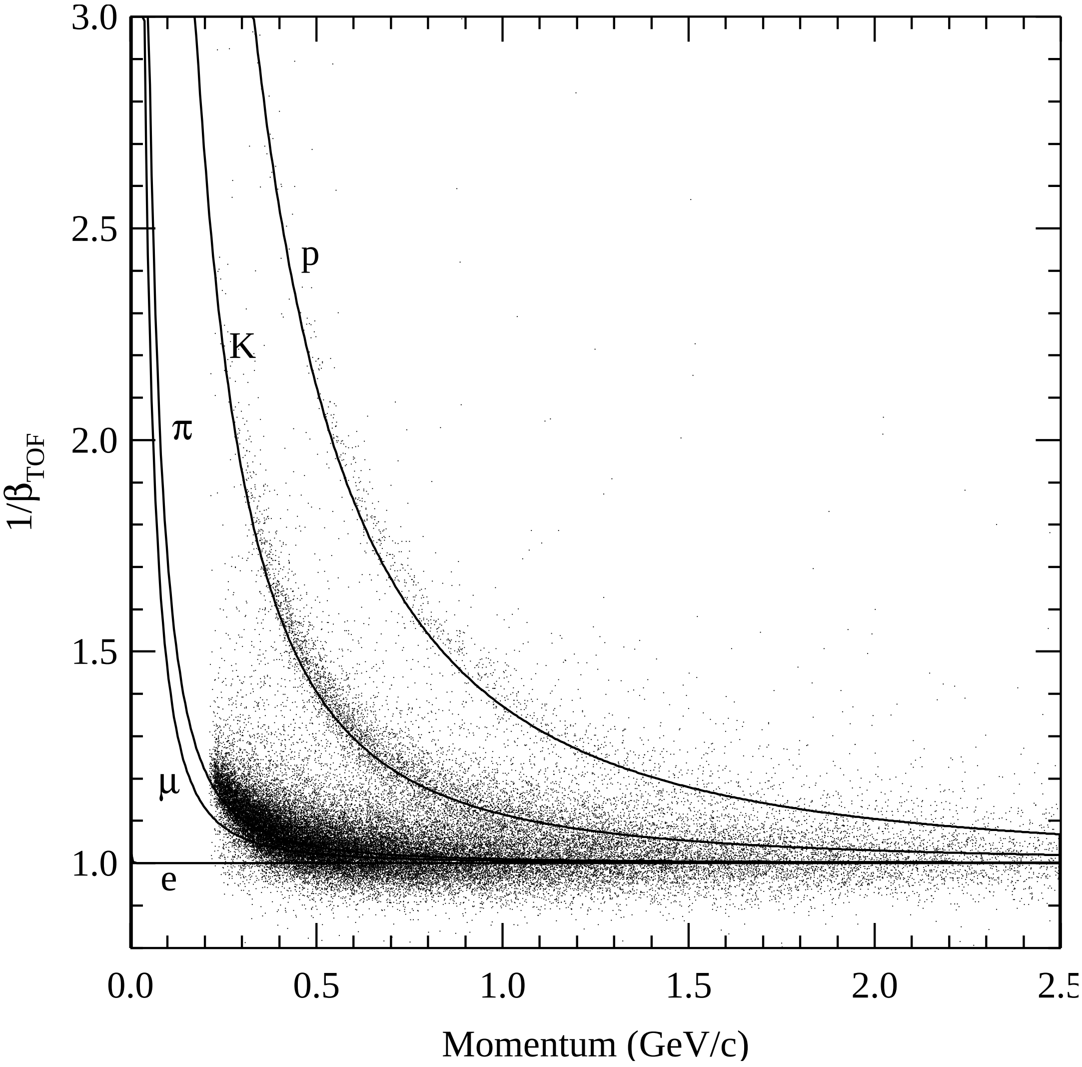

Figure 3.9: $1/\beta$ measured in the TF versus momentum measured in the tracking chambers.

of their energy concentrated in the middle nine crystals, giving them values of `E9/E25` close to 1. Because hadronic showers spread out their energy, giving them `E9/E25` values significantly less than 1, `E9/E25` can be used to distinguish photon and electron showers from all other types.

To distinguish photon showers from electron showers, we look for reconstructed tracks that point to the shower. This process is called track-shower matching and is carried out by the `CDCC` processor [24]. Electromagnetic showers that have tracks pointing to them can be ruled out as photon showers, since photons do not leave tracks in the tracking chambers. `CDCC` designates track-shower matches of several different types. For type 1 matches, the track must point within 8 cm of the center of the shower. For type 2 matches, the track must point within 8 cm of the center of any crystal in the shower. Matches of type greater than 3 use only $r - \phi$ information or indicate that a track which does not satisfy a type 1 or 2 match passes near another matched shower. The data event that was shown in Figure 3.7 is shown again in Figure 3.10, this time with the track-shower match information. The first number shown at the end of the tracks is the track number, and the second number is the number of the matched shower; vice-versa for shower labels. The absence of a second number means that no track (shower) was matched to that shower (track).

3.5.4 Lepton Identification

Correctly identifying leptons from $D^{*0}\ell\nu$ decays requires a more direct system than identifying the hadrons. As mentioned above, we do not use any direct particle

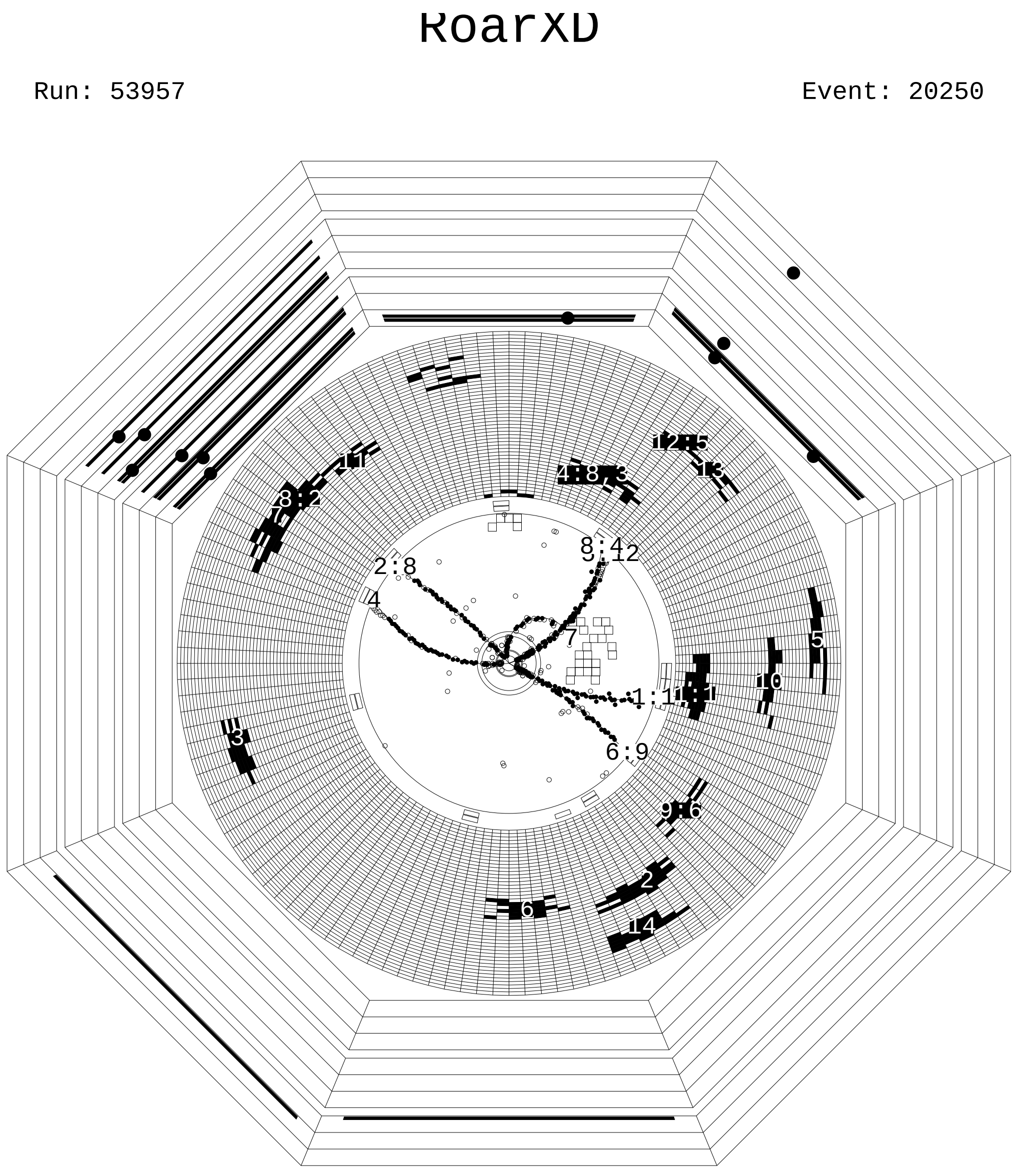

Figure 3.10: A data event showing track-shower matching. The first number at the end of a track is the track number; the second number is the number of the matched shower. The labeling is reversed for the showers.

identification information (dE/dx, time of flight) for our K and π candidates; instead, the K, π, and π^0 from the D^{*0} are identified indirectly. In the case of the D^0, the 4-momenta of two candidate tracks are combined, and the mass of the resulting "particle" is examined. If the two particles really came directly from the D^0, the resulting mass will be close to m_{D^0};[7] if two non-related tracks are combined, the mass will most likely fall far from m_{D^0}. A similar procedure is followed to find π^0's from two showers and D^{*0}'s from D^0 and π^0 candidates. Requiring the reconstructed mass of the candidate parent particle to fall in some range around the measured mass of the parent particle effectively identifies the daughter particles. Since we do not detect neutrinos in CLEO II, the same procedure cannot be followed to identify the lepton from the B [25]. We instead identify leptons directly by their track and/or shower properties; this of course causes us to include leptons which do not come from $D^{*0}\ell\nu$ decays, a subject which is addressed in the next chapter.

We use the `CEID` package [26] to identify electron candidates. `CEID` examines each track and produces a log-likelihood that each track is an electron, called `r2elec`. `r2elec` is defined as

$$\texttt{r2elec} = \sum_i ln(\frac{P_{ei}}{P_{\not e i}}), \tag{3.3}$$

where the sum is over several variables, described below, P_{ei} is the probability that, given the variable's value, the track/shower was produced by an electron, and $P_{\not e i}$ is the probability that value was not produced by an electron. P_{ei} and

[7] There is measurement error in the momenta of the tracks, so the mass of correctly-identified D^0's is smeared around the true mass.

$P_{\not e i}$ are calibrated using Bhabha events, which are purely electrons, and $\Upsilon(1S)$ decays, which produce very few electrons. `r2elec` includes the variables dE/dx, the track-shower match distance, `E9/E25`, and the time of flight, all of which were described above, as well as E/p, the track-shower match distance, `LP2SH`, and `LP3SH`. A higher value of `r2elec` means that it is more likely that track was produced by an electron.

E/p and the track-shower match distance relate track information to shower information. E/p refers to the energy of the matched shower, E, divided by the track's momentum, p. For electrons, which have a very small mass (0.5 MeV/c^2), the relationship $E^2 = m^2c^4 + p^2c^2$ becomes to good approximation $E = pc$ at the energies in which we are interested ($E > 800$ MeV). Since electrons (and photons) usually deposit all of their energy in the calorimeter, E/p is very close to 1 for electrons, while for other charged particles it is usually significantly less. The track-shower distance is defined as the absolute distance between the center of the shower and the point on the surface of the CC to which the track extrapolates. The track-shower distance tends to be smaller for electrons. Figure 3.11 shows the E/p and track-shower distance distributions of electrons and hadrons.

The variables `LP2SH` and `LP3SH` give information about the size of the shower. `LP2SH` is the RMS width of the shower, and `LP3SH` is the ratio of the RMS width of the shower in θ to the RMS width of the shower in ϕ. Electrons have narrower distributions than hadrons in both of these variables. Figure 3.12 shows these distributions for electrons and for hadrons.

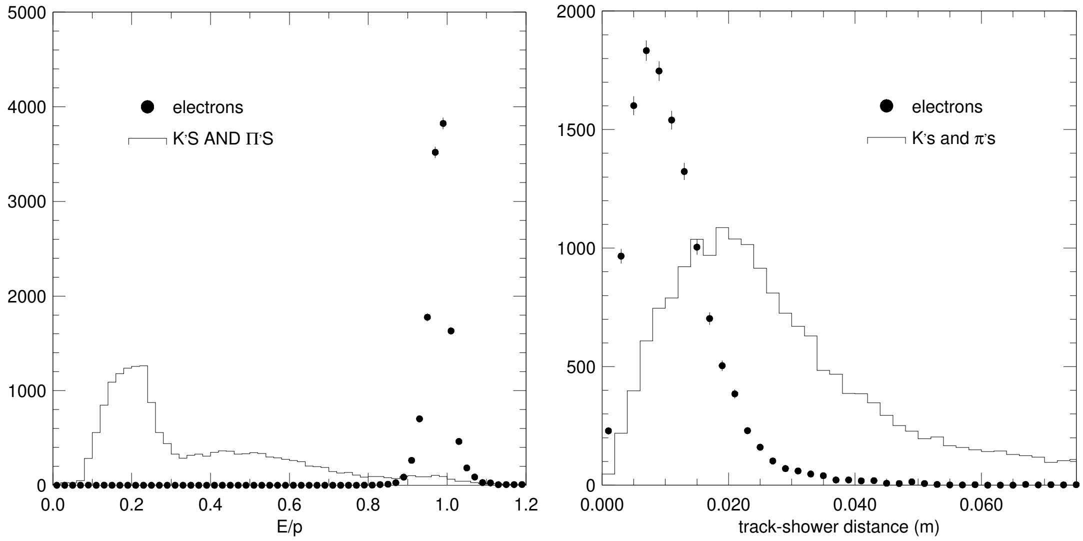

Figure 3.11: The left plot shows E/p for electrons and hadrons, and the right plots shows the track-shower distance for electrons and hadrons.

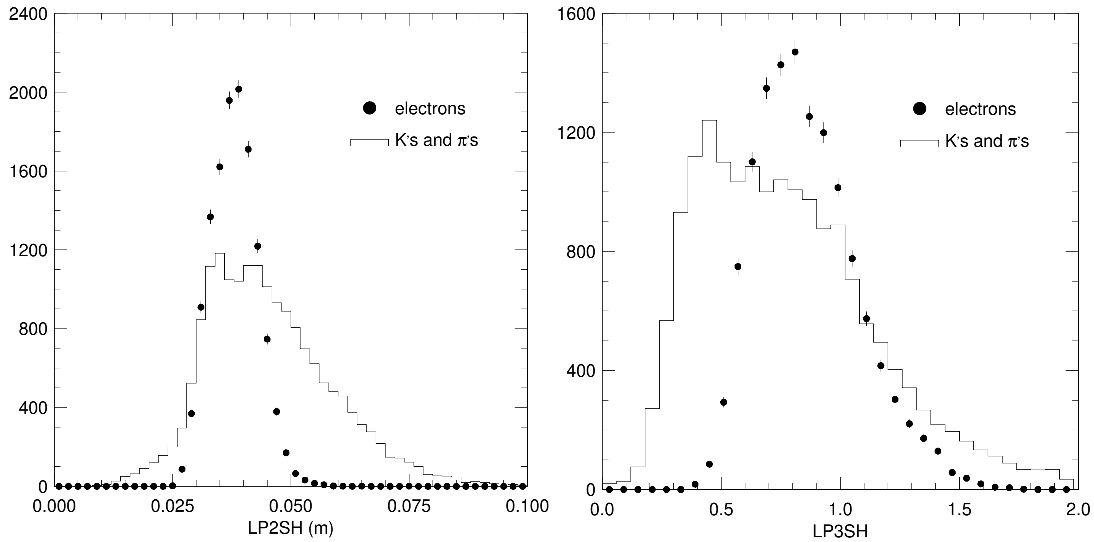

Figure 3.12: `LP2SH` (left) and `LP3SH` (right) for electrons and hadrons.

Muon identification is more simple than electron identification because of the muon detector. Tracks are extrapolated to the muon counter layers and matched to hits. To be a match, there must be hits in at least two out of the three counters in that layer. There must be a match in any layer that the muon is expected to reach (based on its momentum) or the track is disqualified. If there is a match in an outer layer but one is not found where expected in an inner layer, the variable `MUQUAL` is set to be non-zero. The variable `DPTHMU` records how many interaction lengths[8] of iron the particle penetrated to reach the outermost matched layer. The three counter layers sit at roughly 3, 5, and 7 interactions lengths (depending on the trajectory of the track). Particles must have at least 1, 1.4, and 1.8 GeV/c of momentum to reach a `DPTHMU` of 3, 5, and 7, respectively. Track number 2 in Figure 3.10 is most likely a muon; it has 1.5 GeV/c of momentum and penetrates to the second muon counter layer, as expected given its momentum. Requiring higher values of `DPTHMU` gives a lower efficiency but also decreases the likelihood that the track is not a muon, known as the "fake rate."

3.6 Detector Simulation

The CLEO II detector response to $D^{*0}\ell\nu$ and other decays is simulated by a program called `CLEOG`. We use this simulation to measure the efficiency for CLEO II to reconstruct $D^{*0}\ell\nu$ decays, to simulate some background events, and to test our method for measuring $|V_{cb}|$.

[8] A nuclear interaction length is the average distance a particle travels in a material between interactions with the nuclei in that material. In iron it is 16.8 cm.

CLEOG is based on GEANT [28], a program which simulates the passage of particles through matter. The simulation is based on random-number generation and is therefore often referred to as "Monte Carlo." The CLEOG code contains a complete description of the material in CLEO II, from sense wires and calorimeter crystals to support structures and readout cables. Figure 3.13 shows an $r-\phi$ cross-section of one quadrant of the detector at $z = 0$. The inner and outer cathodes and support structures of the tracking chambers are visible, as well as the barrel TF counters, the barrel CC crystals, the superconducting coil and return yoke, and the first two layers of the muon detector. The tracks in the figure show how GEANT propagates particles, including secondary particles from interactions with the detector material; this is especially apparent in the calorimeter showers. The tracks shown are, in clockwise order, an electron, a μ^-, a photon, and a π^+. This "event" was generated for display purposes; in general, GEANT takes input from QQ, a program which simulates the creation and decay of B-pairs in the beam pipe. GEANT starts with the daughters of the B's and propagates them outward from the interaction point, allowing the particles to decay further. GEANT records how much energy was deposited in each detector component, and CLEOG translates the energy into a raw signal exactly like the raw signals read out of CLEO II, writing the signals to an output file. This output file is then input to pass2, which outputs a ROAR file that can be analyzed like a data file.

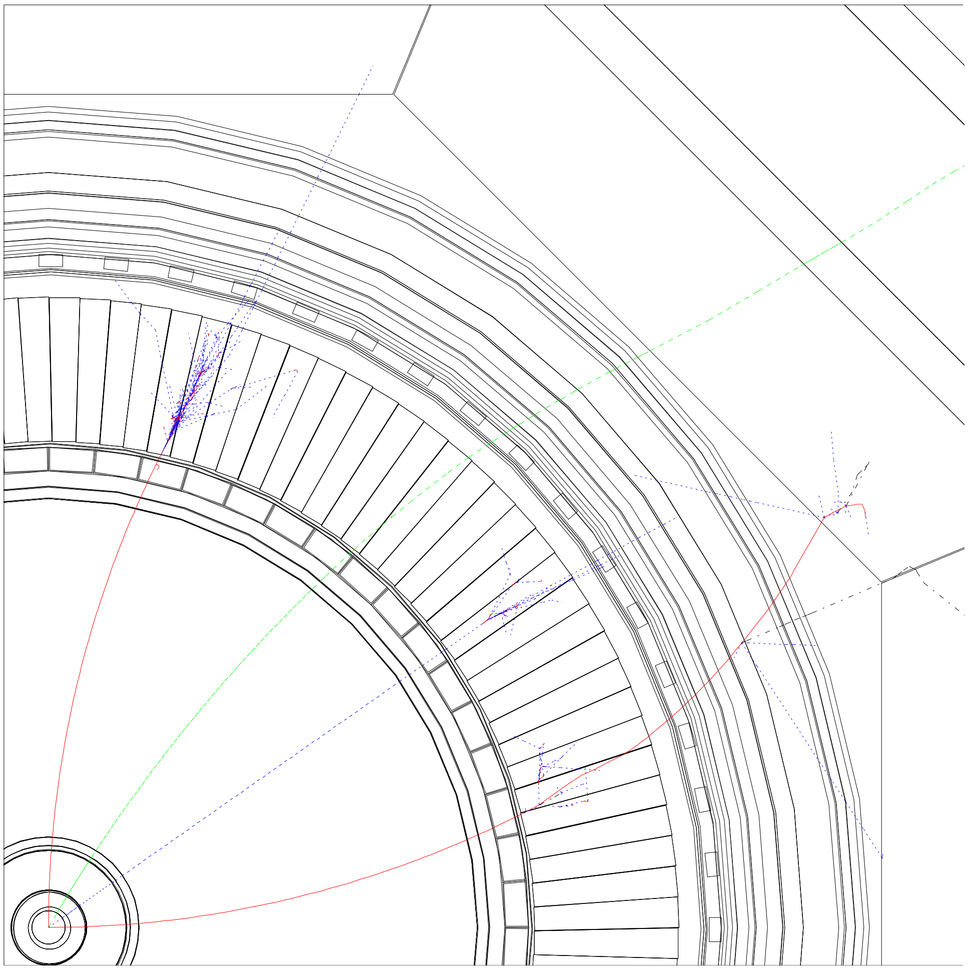

Figure 3.13: Simulated particle tracks.

CHAPTER 4

MEASUREMENT

In this chapter we describe how we measure $|V_{cb}|$ from our data sample. Section 4.1 describes our data sample. Section 4.2 describes several Monte Carlo samples that we use in our analysis. Section 4.3 gives the details of how we reconstruct $D^{*0}\ell\nu$ candidates. Section 4.4 describes the likelihood fit that we use to determine the $D^{*0}\ell\nu$ yields in bins of w. Finally, Section 4.5 describes how we extract $|V_{cb}|$ from the $D^{*0}\ell\nu$ yields.

4.1 Data Sample

We do our analysis with 3.04 million $B\overline{B}$ events ($2.9\,\mathrm{fb}^{-1}$) produced on the $\Upsilon(4S)$ resonance and with $1.5\,\mathrm{fb}^{-1}$ of off-resonance data. We use the 4s2 through 4sG "recompress" data sets, excluding the runs between 59630 and 61778 (part of 4s9 and all of 4sA) because of poor calibration of the CC at low shower energies. The data sets are summarized in Table 4.1.

Table 4.1: The CLEO II data sets.

Data Set	Start Date	End Date	$\mathcal{L}_{Total}$ (pb^{-1})	$\mathcal{L}_{on}/\mathcal{L}_{off}$	$N_{B\bar{B}}$
4s2	11/11/90	6/4/91	672.0	2.36	503790
4s3	9/18/91	2/17/92	680.2	2.21	487290
4s4	4/10/92	5/26/92	317.5	2.12	231262
4s5	7/9/92	10/5/92	342.7	2.06	230005
4s6	11/3/92	1/19/93	316.5	2.73	247102
4s7	3/16/93	7/6/93	461.3	1.62	314084
4s8	8/1/93	9/27/93	274.4	2.01	202458
4s9	11/22/93	1/10/94	340.1	1.97	249463
4sA	1/20/94	2/28/94	190.8	2.54	143563
4sB	3/19/94	5/16/94	140.9	1.32	86569
4sC	6/16/94	8/15/94	141.5	3.21	114491
4sD	9/15/94	10/9/94	98.0	1.05	53218
4sE	10/9/94	11/1/94	128.8	1.16	66334
4sF	11/3/94	11/28/94	145.9	1.34	90632
4sG	1/19/95	4/9/95	456.6	1.52	302289

4.2 Simulated Events

The analysis uses events from a GEANT-based [28] Monte Carlo simulation (described in Section 3.6) to provide information on $D^*\ell\nu$ events and some backgrounds. We use three samples, which are described below and are known as generic Monte Carlo, $D^*\ell\nu$ Monte Carlo, and $D^*X\ell\nu$ Monte Carlo.

We use a sample of 15.5 million "generic" $B\overline{B}$ Monte Carlo events to simulate some backgrounds and for systematic error studies. This sample is meant to simulate the CLEO II $B\overline{B}$ data. The name "generic" refers to the fact that the B's are allowed to decay through any known decay mode. These decays are cataloged in the file `/cleo/clib/runfil/decay.dec`. The branching fractions of the various modes are set using measurements from the data. Of particular importance to this analysis, the semileptonic branching fractions have been adjusted so that the momentum spectrum of leptons from $B \to X_c\ell\bar{\nu}$ decays matches the same distribution measured from the data. This is accomplished by moving the separate branching fractions up and down; since different modes have different lepton spectra due to mass and spin differences in the X_c, adjusting the branching fractions relative to one another also adjusts the lepton momentum distribution.

Our $D^*\ell\nu$ Monte Carlo sample consists of 4.75×10^5 $B\overline{B}$ events in which we have required one of the B's to decay through the series of decays that we reconstruct ($B \to D^*\ell\bar{\nu}$, $D^{*0} \to D^0\pi^0$, etc.). The other B is allowed to decay generically. In the simulation, $D^*\ell\nu$ decays are modeled using a linear form factor (for $h_{A_1}(w)$) with the parameters measured in a previous CLEO analysis [12]. We simulate other form factors by re-weighting this sample. The `EvtGen` package accounts for the angular correlations between the decay products (which is necessary because some decay products have non-zero spin). Simulation of final-state radiation, which occurs when the lepton in the $B \to D^* \ell \bar{\nu}$ decay radiates a photon, is provided by PHOTOS [29].

We generate a sample of 40,000 $D^* X \ell \nu$ decays for our $D^* X \ell \nu$ Monte Carlo, where $D^* X \ell \nu$ refers to B semileptonic decays containing D resonances higher than D^* and the decay $B \to D^* \pi \ell \bar{\nu}$. Non-resonant $B \to D^* \pi \ell \nu$ decays are modeled using the results of Goity and Roberts [30], and $B \to D^{**} \ell \nu$ decays are modeled using the ISGW2 [31] form factors. The specific modes and branching fractions used are listed in Table 4.2.

4.3 Event Reconstruction

To suppress non-$B\overline{B}$ events, we require the ratio of Fox-Wolfram moments H_2/H_0 [18] to be less than 0.4. We calculate this ratio using only Trackman-approved (`TMNG`) tracks with energy less than the beam energy and showers that do not have a type 1 or 2 track match. We also require `KLASGL` $= 10$, which is an event category defined by the following conditions:

- The event must have at least three charged tracks, one of which has to extrapolate back to within 5 mm of the interaction point;
- The sum of the energy measured in the tracking chambers and the calorimeter must be at least 20% of the center-of-mass energy of the event;

Table 4.2: Modes and branching fractions used for $B \to D^* X \ell \nu$ simulation.

Primary Decay	Secondary Decay
$\mathcal{B}(B^- \to D^{*0}\pi^0\ell^-\bar{\nu}_\ell) = 0.23\%$	
$\mathcal{B}(B^- \to D_1^{*0}\,\ell^-\bar{\nu}_\ell) = 0.11\%$	$\mathcal{B}(D_1^{*0} \to D^{*0}\pi^0) = 33.0\%$
$\mathcal{B}(B^- \to D_1^0\,\ell^-\bar{\nu}_\ell) = 0.66\%$	$\mathcal{B}(D_1^0 \to D^{*0}\pi^0) = 33.0\%$
$\mathcal{B}(B^- \to D_2^{*0}\,\ell^-\bar{\nu}_\ell) = 0.33\%$	$\mathcal{B}(D_2^{*0} \to D^{*0}\pi^0) = 10.4\%$
$\mathcal{B}(B^- \to D'^0\,\ell^-\bar{\nu}_\ell) = 0.02\%$	$\mathcal{B}(D'^0 \to D^{*0}\pi^0) = 33.7\%$ $\mathcal{B}(D'^0 \to D^{*0}\gamma) = 0.4\%$
$\mathcal{B}(B^- \to D^{*\prime 0}\,\ell^-\bar{\nu}_\ell) = 0.22\%$	$\mathcal{B}(D^{*\prime 0} \to D^{*0}\pi^0) = 12.2\%$ $\mathcal{B}(D^{*\prime 0} \to D^{*0}\gamma) = 0.1\%$ $\mathcal{B}(D^{*\prime 0} \to D_1^{*+}\,\pi^-) = 0.6\%$ $\mathcal{B}(D^{*\prime 0} \to D_1^{*0}\,\pi^0) = 0.3\%$
$\mathcal{B}(\bar{B}^0 \to D^{*0}\pi^+\ell^-\bar{\nu}_\ell) = 0.47\%$	
$\mathcal{B}(\bar{B}^0 \to D_1^{*+}\,\ell^-\bar{\nu}_\ell) = 0.11\%$	$\mathcal{B}(D_1^{*+} \to D^{*0}\pi^+) = 67.0\%$
$\mathcal{B}(\bar{B}^0 \to D_1^+\,\ell^-\bar{\nu}_\ell) = 0.66\%$	$\mathcal{B}(D_1^+ \to D^{*0}\pi^+) = 67.0\%$
$\mathcal{B}(\bar{B}^0 \to D_2^{*+}\,\ell^-\bar{\nu}_\ell) = 0.33\%$	$\mathcal{B}(D_2^{*+} \to D^{*0}\pi^+) = 20.8\%$
$\mathcal{B}(\bar{B}^0 \to D'^+\,\ell^-\bar{\nu}_\ell) = 0.02\%$	$\mathcal{B}(D'^+ \to D^{*0}\pi^+) = 33.1\%$
$\mathcal{B}(\bar{B}^0 \to D^{*\prime +}\,\ell^-\bar{\nu}_\ell) = 0.22\%$	$\mathcal{B}(D^{*\prime +} \to D^{*0}\,\pi^+) = 24.9\%$ $\mathcal{B}(D^{*\prime +} \to D_1^{*0}\,\pi^+) = 0.3\%$ $\mathcal{B}(D^{*\prime +} \to D_1^{*+}\,\pi^0) = 0.7\%$

- If there are three tracks, the sum of the energy measured in the calorimeter must be at least 15% of the center-of-mass energy;
- If there are three or four tracks, the sum of the energy measured in the calorimeter must be less than 65% of the center-of-mass energy (this excludes radiative Bhabha events);
- The vertex of the event must fall within 2 cm of the interaction point in the $r-\phi$ plane and 5 cm in the z direction.

We reconstruct D^{*0}'s by looking for the daughter particles from the decays $D^{*0} \to D^0\pi^0$, $D^0 \to K^-\pi^+$, and $\pi^0 \to \gamma\gamma$ (charge-conjugate decays are implied throughout this work). We first combine oppositely-charged kaon and pion candidates in hadronic events to form D^0 candidates. We use the Kalman kaon and pion hypothesis tracks for the kaon and pion candidate, respectively. We require the tracks to be Trackman (`TMNG`) approved and to have a `KINCD` value of 0 or -2, which requires good z information. We also require `DBKL`, the distance of closest approach to the interaction point in the $r-\phi$ plane, to be less than 0.005 m, and `ZOKL`, the distance of closest approach in z, to be less than 0.05 m. We require $|\cos\theta| \leq 0.9$ for kaon and pion candidates. Tracks with $\cos\theta$ larger than this pass through the endplate of the VD, which contains a significant amount of material. This material is not modeled well by our simulation, so we exclude those tracks from consideration. We veto on `Z_ESCAPE` tracks, in which the z information comes from an assumption that the particle left the detector via the endplate at the layer of the outermost hit, and `DREDGE` tracks, which are tracks

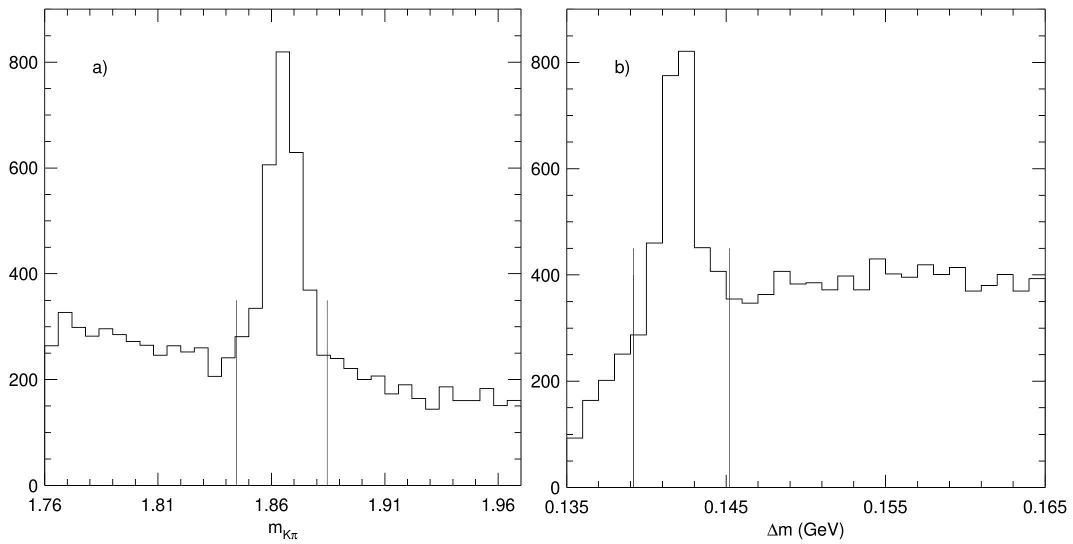

Figure 4.1: (a) The $m_{K\pi}$ distribution. All requirements are met except $|m_{K\pi} - 1.865\ \mathrm{GeV}/c^2| \leq 0.020\ \mathrm{GeV}/c^2$. We accept candidates that fall between the vertical lines. (b) The Δm distribution. All requirements are met except $|\Delta m - 0.1422\ \mathrm{GeV}/c^2| \leq 0.003\ \mathrm{GeV}/c^2$. We accept candidates that fall between the vertical lines.

constructed from "leftover" hits not matched to any other track. The resolution of the $m_{K\pi}$ peak is about 7 MeV; we accept candidates that lie in the window $|m_{K\pi} - 1.865\ \mathrm{GeV}/c^2| \leq 0.020\ \mathrm{GeV}/c^2$, roughly three times this resolution. The $m_{K\pi}$ distribution for $D^*\ell\nu$ candidates is shown in Figure 4.1(a).

The pions produced in the decay $D^{*0} \to D^0\pi^0$ have low momentum (< 250 MeV) because the combined mass of the D^0 and π^0 is within 8 MeV of the mass of the D^{*0}. We give these pions the label "slow." We add a slow π^0 to the D^0 candidate to get a D^{*0} candidate. We take π^0 candidates from the `anlcp0.inc` common block. The momentum information for these π^0's has been derived from a kinematic fit to pairs of calorimeter showers that modifies the shower parameters to force the reconstructed π^0 to have the measured π^0 mass, 0.13498 GeV/c^2. We require both showers to pass a cut for `E9/E25` which has been calibrated to be 99% efficient for photons and which varies with the shower's energy. We veto showers with a track match of type 1 or 2, and we veto "bad" showers, which contain a crystal which is known to be noisy. The di-photon mass $m_{\gamma\gamma}$ is the mass calculated from the raw shower information; the data distribution has an unexplained bump in the region 0.142 GeV/$c^2 \leq m_{\gamma\gamma} \leq$ 0.150 GeV/c^2 which is not modeled by the Monte Carlo (see Figure B.3). We require $m_{\gamma\gamma}$ to pass 0.120 GeV/$c^2 \leq m_{\gamma\gamma} \leq$ 0.150 GeV/c^2 to avoid this bump. The $\Delta m = m_{K\pi\pi} - m_{K\pi}$ resolution for D^{*0}'s is about 0.9 MeV, so we require $|\Delta m - 0.1422 \text{ GeV}/c^2| \leq 0.003$ GeV/c^2. The Δm distribution for D^{*0} candidates is shown in Figure 4.1(b), and the $m_{\gamma\gamma}$ distribution is shown in Figure 4.2. Particles with $|\cos\theta| > 0.71$ travel through the endplate of the outermost tracking chamber before reaching the calorimeter, again traversing a significant amount of material. We therefore require that both photons satisfy $|\cos\theta| \leq 0.71$ so as to remain in the part of the calorimeter with the best energy and position resolution. Both photons must have energy greater than 30 MeV to limit background from very soft showers. Finally, we require the momentum of the D^{*0} candidate to be less than $\frac{1}{2}\sqrt{E_B^2 - m_{K\pi\pi}^2}$, or about 2.5 GeV/$c$, where E_B is the energy of the beam.

We next combine the D^{*0} candidate with a lepton candidate, accepting both electrons and muons. We use the Kalman electron and muon track parameters for electrons and muon candidates, respectively. We choose electron and muon

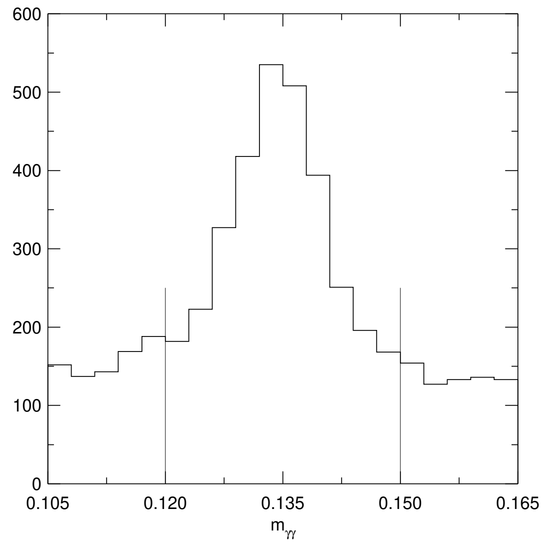

Figure 4.2: The $m_{\gamma\gamma}$ distribution. All requirements are met except 0.120 GeV/c^2 $\leq m_{\gamma\gamma} \leq$ 0.150 GeV/c^2. We accept candidates that fall between the vertical lines.

identification parameters that are compromises between higher efficiency and a lower chance that the particle is not a lepton. Electrons are identified using the `CEID` package and requiring `R2ELEC` ≥ 3. We require our candidates to lie in the momentum range 0.8 GeV/$c \leq p_e \leq$ 2.4 GeV/c; the lower bound is chosen to limit the contribution from $D^* X \ell\nu$ decays, and the upper bound is the endpoint of $D^*\ell\nu$ decays. We require muon candidates to have `MUQUAL` $= 0$ and `DPTHMU` ≥ 5, which means they must penetrate two layers of steel in the solenoid return yoke, or about 5 interaction lengths. Only muons with momenta above about 1.4 GeV/c satisfy this requirement; we therefore demand that they lie in the momentum range 1.4 GeV/$c \leq p_\mu \leq$ 2.4 GeV/c. The lepton must satisfy $|\cos\theta| \leq 0.71$ and the same requirements on Trackman, `KINCD`, `DBKL`, `Z0KL`, `Z_ESCAPE`, and `DREDGE` as the tracks that make up the D^0 candidates. The charge of the lepton must match the charge of the kaon.

We use the D^{*0} and lepton to calculate the variables $\cos\theta_{B-D^*\ell}$ and w, which are related to the kinematics of the $B \to D^*\ell\bar{\nu}$ decay. Through energy and momentum conservation, we can relate the invariant mass of the neutrino to the 4-momenta of the B, the D^{*0}, and the lepton:

$$p_\nu^2 = (p_B - p_{D^*} - p_\ell)^2. \tag{4.1}$$

Setting the neutrino mass to zero gives

$$0 = m_B^2 + m_{D^*\ell}^2 - 2(E_B E_{D^*\ell} - \vec{p}_B \cdot \vec{p}_{D^*\ell}). \tag{4.2}$$

The energy and momentum of the D^*-lepton pair come from our reconstruction. The B mass has been measured by CLEO [32], and the magnitude of the B momentum has been measured for each data set (see below for details); from these we compute E_B. We solve for the only unknown quantity, the angle between the B meson and the D^*-lepton pair:

$$\cos\theta_{B-D^*\ell} = \frac{2E_B E_{D^*\ell} - m_B^2 - m_{D^*\ell}^2}{2|\mathbf{p}_B||\mathbf{p}_{D^*\ell}|}. \tag{4.3}$$

When calculating E_{D^*}, we use the true D^{*0} mass rather than the reconstructed $m_{K\pi\pi}$ to avoid a bias in the $\cos\theta_{B-D^*\ell}$ distribution of the high Δm sideband, which we use to determine a background as described in Section 4.4.1. For off-resonance events, we compute $\cos\theta_{B-D^*\ell}$ using the average B momentum and scaling the D^* and lepton 4-momenta by the ratio E_{on}/E_{off}.

We derive the momentum of the B from measurements of the average B^0 and B^+ momenta for each data set [33]. The momentum of B's reconstructed in generic Monte Carlo differs from the true B momentum by 0.0012±0.0006 GeV/c on average, so we first correct the data momenta by this amount. The average over all data sets of the B^0 and B^+ momenta differ by 0.0083±0.0022 GeV/c, which is expected since the B^0 and B^+ have slightly different masses. We combine the B^0 and B^+ measurements in each data set to improve the statistical error, adding the the measured difference to the B^0 momenta. There are errors on the average B^+ momentum from half of the error on the mean $B^+ - B^0$ momentum difference (1.1 MeV/c), the statistical error on the correction to the B^+ momentum (0.6 MeV/c) and the statistical error on the average momentum from the statistical error on each dataset measurement (0.9 MeV/c); added in quadrature, these errors give a total error of 1.6 MeV/c. The average B^+ momentum for each dataset derived from this method is listed in Table 4.3. We also use the measured B^0-B^+ momentum difference to correct the value of the B mass measured in [32] to $m_{B^+} = 5278.9 \pm 0.6$ MeV/c^2.

While we use $\cos\theta_{B-D^*\ell}$ to distinguish true $B \to D^*\ell\bar{\nu}$ decays from background, it is also necessary for calculating w. Without knowing the flight direction of the B, we cannot calculate the true value of w, but $\cos\theta_{B-D^*\ell}$ gives us some information on the B direction relative to the D^*-lepton pair. We find the B momentum for each of the extreme cases as follows, with Y standing for the D^*-lepton pair:

Table 4.3: The average B^+ momentum for each data set. The errors are uncorrelated between data sets.

Data Set	B^+ Momentum (GeV/c)
4s2	0.3003±0.0028
4s3	0.3348±0.0023
4s4	0.3397±0.0035
4s5	0.3069±0.0038
4s6	0.3348±0.0031
4s7	0.3214±0.0029
4s8	0.3084±0.0045
4s9	0.3119±0.0041
4sA	0.3043±0.0056
4sB	0.3540±0.0058
4sC	0.2962±0.0061
4sD	0.2854±0.0122
4sE	0.3027±0.0089
4sF	0.2985±0.0069
4sG	0.2928±0.0036

- We calculate $\vec{p}_\perp$, which gives the direction perpendicular to the D^*-lepton combination and in the plane defined by the D^* and lepton momenta:

$$\vec{p}_\perp = \vec{p}_\ell(\vec{p}_Y \cdot \vec{p}_{D^*}) - \vec{p}_{D^*}(\vec{p}_Y \cdot \vec{p}_\ell). \tag{4.4}$$

- We find two momentum vectors for the B, one in which $\vec{p}_B$ points maximally in the direction of $p_\perp$, and one in which $\vec{p}_B$ points maximally in the direction opposite of $p_\perp$:

$$\vec{p}_B = |\vec{p}_B| \cos\theta_{BY} \hat{p}_Y \pm |\vec{p}_B| \sin\theta_{BY} \hat{p}_\perp, \tag{4.5}$$

  where $|\vec{p}_B|$ is the measured B momentum.

- We calculate q^2, which is the invariant mass of the virtual W, for each $\vec{p}_B$ from the B and D^* 4-momenta:

$$q^2 = p^2_{W^*} = (p_\nu + p_\ell)^2 = (p_B - p_{D^*})^2. \tag{4.6}$$

  From that we calculate w using Equation 2.9.

- We average the two values of w.

We divide the data into ten equal bins of w from 1.0 to 1.5, but not all of our data sits within these limits. The w endpoint for $B \to D^*\ell\bar{\nu}$ decays is 1.504, and some events are also reconstructed outside the physics limits due to detector resolution. We assign events with $w < 1$ to the first bin and events with $w > 1.5$ to the last bin. In the high w bins, we suppress background with minor loss of signal efficiency by restricting the cosine of the angle between the D^* and the lepton ($\cos\theta_{D^*-\ell}$). The distribution of $\cos\theta_{D^*-\ell}$ versus w is shown in Figure 4.3 for $B \to D^*\ell\nu$ decays. The accepted angles are listed in Table 4.4.

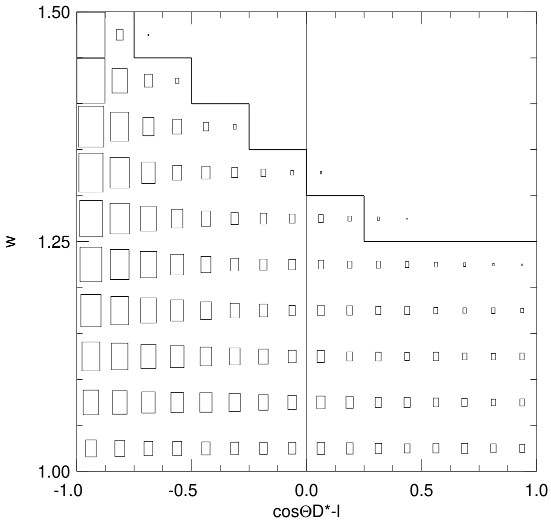

Figure 4.3: The distribution of w versus $\cos\theta_{D^*-\ell}$ for simulated $D^{*0}\ell\nu$ decays. We accept candidates that fall below and to the left of the stairstep line.

Table 4.4: The accepted regions of the cosine of the angle between the D^* and the lepton in each w bin.

w Bin Number	w Limits	Accepted $\cos\theta_{D^*-\ell}$
1-5	<1.25	-1.0 to 1.00
6	1.25-1.30	-1.0 to 0.25
7	1.30-1.35	-1.0 to 0.00
8	1.35-1.40	-1.0 to -0.25
9	1.40-1.45	-1.0 to -0.50
10	>1.45	-1.0 to -0.75

4.4 Extracting the $D^*\ell\nu$ Yields

Our $B \to D^*\ell\bar{\nu}$ candidates contain $D^*\ell\nu$, $D^*X\ell\nu$, and various backgrounds. We separate out the $D^*\ell\nu$ component using a binned maximum likelihood fit to the $\cos\theta_{B-D^*\ell}$ distribution. In this fit, the normalizations of the various background distributions are fixed and we allow the normalizations of the $D^*\ell\nu$ and the $D^*X\ell\nu$ events to float. While we allow the overall normalization of $D^*X\ell\nu$ decays to vary, the relative branching fraction of each $D^*X\ell\nu$ mode remains fixed. Unlike many likelihood fits, our likelihood fit includes the statistical uncertainties on the background, $D^{*0}\ell\nu$, and $D^*X\ell\nu$ $\cos\theta_{B-D^*\ell}$ distributions along with the data uncertainties [34].

By fitting we allow the data to set the normalization of the $D^*X\ell\nu$ events. As shown in Figure 4.4, $B \to D^*\ell\nu$ decays are concentrated in the physical region, $-1 \leq \cos\theta_{B-D^*\ell} < 1$, while the larger missing mass of the $D^{**}\ell\nu$ decays allows them to populate $\cos\theta_{B-D^*\ell} < -1$. The normalization of the $D^*X\ell\nu$ contribution is therefore primarily determined by the data in the $\cos\theta_{B-D^*\ell}$ region less than -1. For each bin, we fit in a $\cos\theta_{B-D^*\ell}$ region chosen to include approximately 95% of the $D^*X\ell\nu$ events in that bin. These regions are listed in Table 4.5.

Our $D^{*0}\ell\nu$ Monte Carlo includes $B \to D^{*0}\ell\nu$ decays with final-state radiation. Since we do not reconstruct the emitted photon in these events, we miss some of the energy, which makes the reconstructed $\cos\theta_{B-D^*\ell}$ lower than the actual $\cos\theta_{B-D^*\ell}$.

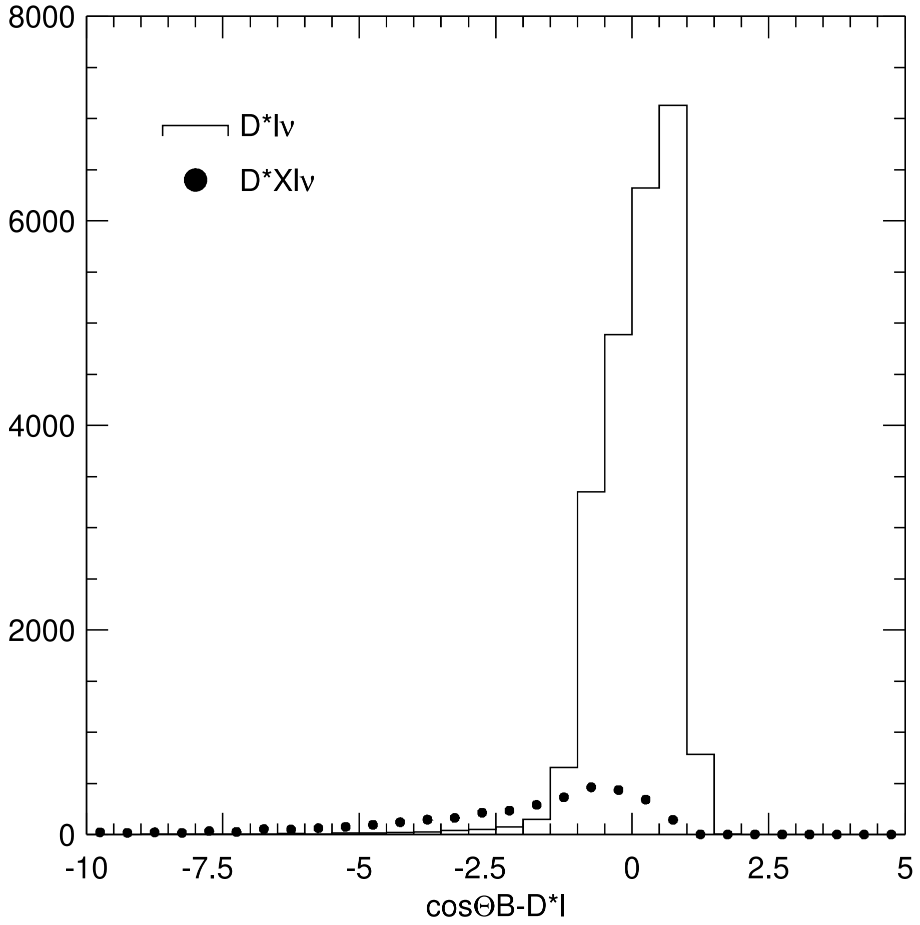

Figure 4.4: The $\cos\theta_{B-D^*\ell}$ distributions for $D^*\ell\nu$ and $D^*X\ell\nu$ simulated events. The $D^*X\ell\nu$ decays are shown at about twice their relative branching fraction in the generic Monte Carlo, since at the correct normalization the $\cos\theta_{B-D^*\ell}$ distribution is difficult to see.

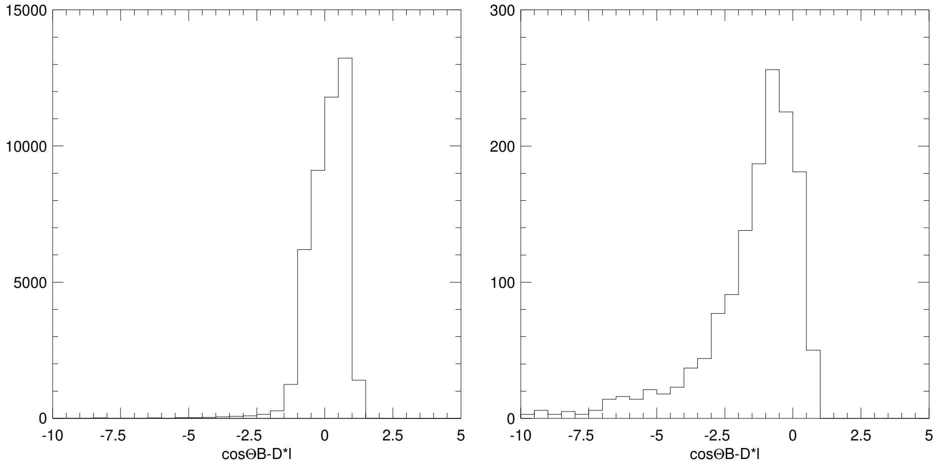

Figure 4.5: The left plot shows the $\cos\theta_{B-D^*\ell}$ distribution for $D^{*0}\ell\nu$ Monte Carlo where either there is no final state radiation or the emitted photon has an energy of less than 100 MeV. The right plot shows the $\cos\theta_{B-D^*\ell}$ distribution for $D^{*0}\ell\nu$ Monte Carlo where final state radiation has occurred and the emitted photon has an energy greater than 100 MeV.

This effect increases the low-side tail of the $D^{*0}\ell\nu$ $\cos\theta_{B-D^*\ell}$ distribution.[1] Since the simulation of final-state radiation is only known to be correct to about 30% [29], we want to limit our reliance on the simulation of this tail. As shown in Figure 4.5, the $\cos\theta_{B-D^*\ell}$ tail comes primarily from events with final-state radiation where the emitted photon has an energy greater than 100 MeV. We choose to treat such events as background by including them in the $\cos\theta_{B-D^*\ell}$ fit but not including them in our $D^{*0}\ell\nu$ yield.

[1]There is a low-side tail on the $D^{*0}\ell\nu$ $\cos\theta_{B-D^*\ell}$ distribution even without final-state radiation; this tail is primarily due to the electron losing energy in interactions with the detector material.

Table 4.5: The regions of $\cos\theta_{B-D^*\ell}$ over which we perform a binned maximum likelihood fit.

w Bin Number	w Limits	$\cos\theta_{B-D^*\ell}$ Fit Region
1-6	< 1.30	-8.0 to 1.5
7	1.30-1.35	-6.0 to 1.5
8	1.35-1.40	-4.0 to 1.5
9	1.40-1.45	-3.0 to 1.5
10	> 1.45	-2.0 to 1.5

Section 4.4.1 describes how we determine the $\cos\theta_{B-D^*\ell}$ distributions and normalizations for the backgrounds, and Section 4.4.2 describes how we determine the $\cos\theta_{B-D^*\ell}$ distributions for $D^*\ell\nu$ and $D^*X\ell\nu$. The results of the $\cos\theta_{B-D^*\ell}$ fits are given in Section 4.4.3.

4.4.1 Backgrounds

There are several sources of decays other than $B \to D^*\ell\nu$ and $B \to D^*X\ell\nu$ that fulfill our requirements. We divide these backgrounds into five classes: continuum, combinatoric, uncorrelated, correlated and fake lepton. The contribution of each background in the range $-1 \leq \cos\theta_{B-D^*\ell} < 1$ (the "signal region") is listed in Table 4.6. We discuss each background and how we determine it below.

Table 4.6: The contribution of each background in percent in the range $-1 \leq \cos\theta_{B-D^*\ell} < 1$ (the "signal region") for $D^{*0}\ell\nu$ candidates.

Background	Contribution (%)
Continuum	2.8
Combinatoric	37.8
Uncorrelated	4.7
Correlated	0.1
Fake Lepton	0.2

Continuum Background

Continuum events are subtracted using off-resonance data, with $\cos\theta_{B-D^*\ell}$ reconstructed as discussed in Section 4.3. We normalize the continuum background using the ratio of on-resonance to off-resonance luminosities, corrected for the small difference in the cross-sections at the two center-of-mass energies. For our data sample, this normalization is 1.92.

Combinatoric Background

Combinatoric background events are those in which one or more of the particles in the D^{*0} candidate does not come from a true D^{*0} decay. This is a large background for $D^{*0}\ell\nu$ decays primarily because there are many low-energy background showers in the calorimeter that can combine to give a π^0 that meets all of our requirements. In addition, we do not have the benefit of a charge correlation between the π^0 and other particles in the decay. Random combinations of K^- and π^+ candidates also contribute to this background. Correctly reconstructed D^{*0}'s peak at $m_{D^{*0}} - m_{D^0} = 0.1422$ GeV/c^2, while combinatoric background has a smooth distribution that falls over a broad range of Δm. The lower and upper limits of w for each bin restrict the range of the D^{*0} energy in each bin, so in each bin the average value of the D^{*0} momentum decreases slightly as Δm increases, which in turn changes the $\cos\theta_{B-D^*\ell}$ distribution. We take the $\cos\theta_{B-D^*\ell}$ distribution of D^{*0} candidates from the high Δm sideband region 0.147 GeV/c^2 $< \Delta m \leq$ 0.165 GeV/c^2 to be representative of the combinatoric background in the Δm signal region. We choose this region because it is large enough to give us a good sample of these events but keeps the mean value of the momentum as close as possible to that of the Δm signal region.

The normalization of the Δm sideband events comes from fits to the Δm distributions in each bin of w. We fit each Δm distribution with a functional form for the background and a histogram of the Δm lineshape for correctly reconstructed D^{*0}'s. We assume a background distribution of the form $n(\Delta m - m_{\pi^0})^a e^{b(\Delta m - m_{\pi^0})}$ and vary n, a, b, and the normalization of the signal peak. After the fit, we integrate the background function in both the Δm signal and sideband regions. We take the ratio of the area in the Δm signal region to the Δm sideband region as the normalization for the Δm sideband $\cos\theta_{B-D^*\ell}$ distribution.

The lineshape for the Δm peak is taken from tagged $D^{*0}\ell\nu$ Monte Carlo and includes some D^{*0} candidates that are not quite correctly reconstructed. D^{*0}'s reconstructed with all the correct particles except one wrong photon preferentially populate the Δm signal region, which means that the Δm sideband does not fully account for this type of misreconstruction. We choose to treat the excess as part of our $D^{*0}\ell\nu$ signal, and we include these events in the $D^{*0}\ell\nu$ lineshape so they do not bias the Δm fit. Also, the width of the peak of the Δm distribution from signal Monte Carlo is smaller than the width of the peak in the data. We have determined that the smaller width is due to a low estimate of the noise on the calorimeter crystals in the Monte Carlo and non-linearity in the response of the crystals at low shower energies that is not modeled by the Monte Carlo (see Appendix B for details). Correcting these faults causes the width of the Monte Carlo Δm peak to increase by 0.61 ± 0.10 MeV/c^2 in quadrature; it was impractical to regenerate our Monte Carlo with these improvements, so we instead add this smearing to our Δm lineshapes. A fit is shown for a representative w bin in Figure 4.6. The normalizations are listed in Table 4.7.

A small component of the combinatoric background is not addressed using our method for background subtraction. This contribution comes from correctly reconstructed D^0 meson decays in which the D^0 is truly a daughter of a D^{*0} and the slow pion is properly found, but the D^0 did not decay in the mode $D^0 \to K^-\pi^+$. An example of such a mode is $D^0 \to K^-K^+$. By misassigning the K^+ the mass of a π, the energy of the D^0 candidate is underestimated; $m_{K\pi}= \sqrt{E^2 - p^2}$ is then lower than m_{D^0}. Assigning the wrong mass smears $m_{K\pi}$ around the mean (because $m_{K\pi}$ depends on the momenta of the two particles), and sometimes these events end up in our $m_{K\pi}$ signal region. In the case of three-body decays like $D^0 \to K^-\mu^+\nu_\mu$, the μ is assigned too much mass, making the mean $m_{K\pi}$ higher,

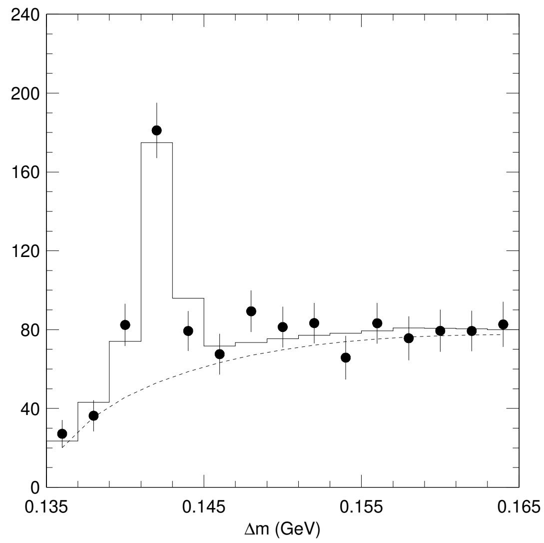

Figure 4.6: A fit to the Δm distribution of events in the third w bin. The data (solid squares) are superimposed with the combinatoric background distribution (dashed curve) and the sum of the background and the D^* signal (solid histogram).

Table 4.7: The Δm sideband normalizations for each w bin.

w Bin Number	Normalization
1	0.2731±0.0161
2	0.2941±0.0196
3	0.2394±0.0199
4	0.2567±0.0261
5	0.2360±0.0257
6	0.2277±0.0295
7	0.2591±0.0413
8	0.1941±0.0455
9	0.2481±0.0555
10	0.2656±0.0628

but we also miss the energy of the ν_μ, bringing the mean $m_{K\pi}$ back in range of our signal region.

We determine the contribution of this component using the generic Monte Carlo. The D^0 modes that contribute are listed in Table 4.8. The first column gives the modes. The second column in the table shows the yield for each mode in the $\cos\theta_{B-D^*\ell}$ signal region from the generic Monte Carlo; the uncertainties are statistical only. The third column gives the branching fraction that was used in generating the generic Monte Carlo, and the fourth column gives the measured branching fraction and uncertainties for each mode. We normalize the contribution from each mode using the ratio of the measured branching fraction to the branching fraction used in the Monte Carlo times the ratio of the number of $B\overline{B}$ events in the data and generic Monte Carlo (0.196). The last column shows the scaled yield from each mode, and the uncertainties include both the statistical uncertainty and the uncertainty on the measured branching fraction. The total predicted yield in the data from this background is 5.2±2.5; this is 0.5±0.3% of the $B \to D^*\ell\bar{\nu}$ yield we find with our $\cos\theta_{B-D^*\ell}$ fits. Since the branching fraction of the main contributing mode ($D \to \rho\pi$) is unmeasured, we include this contribution only as a systematic uncertainty.

Uncorrelated Background

Uncorrelated background arises when the D^{*0} and lepton come from the decays of different B mesons. It is a relatively small background but has many components. B decays produce D^{*0}'s through semileptonic modes as well as through hadronic

Table 4.8: Studied decay modes of the D other than $D^0 \to K^-\pi^+$ that are not fully subtracted by the Δm sideband. The $D^0 \to \pi\pi\pi^0$ category includes both non-resonant $D^0 \to \pi^+\pi^-\pi^0$ decays and resonant $D^0 \to \rho^+\pi^-$, $D^0 \to \rho^-\pi^+$, and $D^0 \to \rho^0\pi^0$ decays; one of the background events comes from the nonresonant mode, and the rest come from either $D^0 \to \rho^+\pi^-$ or $D^0 \to \rho^-\pi^+$. For the mode $D^0 \to \pi\mu\nu$, we use the measured branching fraction of $D^0 \to \pi e\nu$.

Mode	Monte Carlo Yield	Monte Carlo B.F.	Measured B.F. [1]	Scaled Yield
$D^0 \to K^+K^-$	2±1	4.34×10^{-3}	$(4.25 \pm 0.16) \times 10^{-3}$	0.5 ± 0.3
$D^0 \to \pi^+\pi^-$	1±1	1.50×10^{-3}	$(1.52 \pm 0.09) \times 10^{-3}$	0.2 ± 0.2
$D^0 \to K^-\mu^+\nu_\mu$	1±1	3.74%	$3.22 \pm 0.17\%$	0.2 ± 0.2
$D^0 \to \pi^+\pi^-\pi^0$	17±4	1.60%	$1.6 \pm 1.1\%$	3.3 ± 2.4
$D^0 \to K^-\rho^+$	1±1	9.94%	$10.8 \pm 1.0\%$	0.2 ± 0.2
$D^0 \to K^{*-}\pi^+$	1±1	3.50%	$1.7 \pm 0.2\%$	0.1 ± 0.1
$D^0 \to \pi^-\mu^+\nu_\mu$	2±1	2.0×10^{-3}	$(3.7 \pm 0.6) \times 10^{-3}$	0.7 ± 0.5
Total	25±5			5.2±2.5

modes. Semileptonic B decays produce leptons, and daughters of the B can also produce leptons. Combinations of various subsets of these D^{*0}'s and leptons satisfy our requirement on the charge correlation of the K and lepton. Mixing of a neutral B pair introduces further D^{*0}-lepton pairs with the correct charge correlation. To determine this background, we use the $\cos\theta_{B-D^*\ell}$ distribution from generic Monte Carlo for each combination and normalize the contributions according to the measured production rates for each D^{*0} and lepton component.

We classify D^*'s into two categories: upper-vertex, in which the D^* contains the $\bar{c}$ in the decay chain $b \to c\bar{c}s$, and lower-vertex, in which the D^*'s c quark is of the opposite sign of its parent b quark. We also classify the leptons as primary leptons, which come from semileptonic B decays, or secondary leptons, in which the lepton is from the chain $b \to c \to s\ell\nu$.

We divide the uncorrelated background events into five categories as follows (where the first number gives the category designation and the second number gives the percentage of uncorrelated background consisting of that category):

- (1) a lower-vertex D^* combined with a secondary lepton in an event with an unmixed $B\overline{B}$ pair (because primary leptons from the other B have the wrong charge correlation) (26.6%);

- (2) an upper-vertex D^{*0} combined with a primary lepton in an event with an unmixed $B\overline{B}$ pair (17.3%);

- (3) a lower-vertex D^{*0} in which the K and π have been exchanged (swapped) and paired with a primary lepton in an event with an unmixed $B\overline{B}$ pair (42.0%);
- (4) a lower-vertex D^{*0} from a B^0 or $\bar{B}^0$ combined with a primary lepton from the other B, which has mixed (9.3%);
- (5) miscellaneous combinations, of which no one sub-category makes up more than 2% (4.7%).

We further divide categories (1-3) into D^{*0}-lepton pairs from B^+B^- events and $B^0\bar{B}^0$ events. We obtain the $\cos\theta_{B-D^*\ell}$ distributions for each category for the Δm signal and sideband regions from generic Monte Carlo. With tagging, we require the K and π candidates to be primary or secondary descendents of a D, but we make no requirements on the π^0 showers. This allows some combinatoric background into the $\cos\theta_{B-D^*\ell}$ distributions, which we subtract from the $\cos\theta_{B-D^*\ell}$ distribution using the Δm sideband $\cos\theta_{B-D^*\ell}$ distribution normalized with the same normalizations as the data combinatoric background. We also require that the D and lepton come from different B's.

With the combinatoric background subtracted, we normalize each category according to its components. To obtain the normalizations of the B decays containing D^{*0}'s, we compare the yield of inclusive D^{*0} decays in data and generic Monte Carlo events. Since the $\cos\theta_{B-D^*\ell}$ distribution depends somewhat on the momentum distribution of the D^{*0}, we normalize the D^{*0} sources separately in low ($p_{D^*} \leq 1.3$ GeV/c) and high ($p_{D^*} > 1.3$ GeV/c) momentum bins. We scale

Table 4.9: B^- decays of the form $D^{(*)}\bar{D}^{(*)}\bar{K}^{(*)}$ that contribute to the uncorrelated background. Some analogous B^0 decays also contribute.

Decay	Branching fraction (%)
$B^- \to D^{*0}\bar{D}^{*0}K^-$	1.5
$B^- \to D^{*0}D^{*-}\bar{K}^0$	1.5
$B^- \to D^{*0}\bar{D}^0K^-$	0.5
$B^- \to D^{*0}D^-\bar{K}^0$	0.5
$B^- \to D^0\bar{D}^{*0}K^-$	0.5
$B^- \to D^{*0}\bar{D}^{*0}K^{*-}$	0.3
$B^- \to D^{*0}D^{*-}\bar{K}^{*0}$	0.3
$B^- \to D^{*0}\bar{D}^0K^{*-}$	0.5
$B^- \to D^{*0}D^-\bar{K}^{*0}$	0.5
$B^- \to D^0\bar{D}^{*0}K^{*-}$	0.25

the simulated events to match the data, assuming that the upper-vertex D^{*0}'s are correctly modeled and attributing the difference to the lower-vertex D^{*0}'s. We will vary this assumption later to assess the systematic uncertainty. The upper-vertex decays that contribute to this background are listed in Table 4.9. The normalizations for lower-vertex D^{*0}'s are listed in Table 4.10.

We find the normalization of D^{*0}'s reconstructed with exchanged K's and π's by studying inclusive D^{*+} decays with the charge correlation of the slow pion reversed. We determine the ratio of exchanged to unexchanged yields for both data and simulated D^{*+}'s in the same momentum bins as above. We use the ratio of these

Table 4.10: The normalizations for D^{*0} elements of the uncorrelated background.

Rate	$p_{D^*} < 1.3$ GeV/c	$p_{D^*} > 1.3$ GeV/c
lower-vertex	0.812±0.055	0.963±0.048
$K - \pi$ exchange	0.94±0.10	1.19±0.12

rates to normalize the contribution from D^{*0}'s reconstructed with exchanged K and π particles. The normalizations are listed in Table 4.10. While the normalizations are consistent with 1, which we expect since this effect is primarily kinematic and therefore easy to simulate, we use the measured rates to be conservative.

The primary lepton decay rate in the generic Monte Carlo for leptons with momenta between 0.8 and 2.4 GeV/c is 9.18±0.07% and is consistent with its measured value of $8.99 \pm 0.42\%$ [35], where the error includes statistical and systematic errors; since this measurement was made at CLEO, we include only the systematic errors that are uncorrelated with our analysis. The secondary lepton rate for leptons with momenta between 0.8 and 2.4 GeV/c in the generic Monte Carlo is 1.83%; we scale the secondary lepton contributions by 0.836 to make the Monte Carlo consistent with the measured value of $1.53 \pm 0.12\%$ [35]. We adjust χ_d, the $B^0 - \bar{B}^0$ mixing rate, to its measured value of 0.174±0.009 [1] by scaling the unmixed $B^0\bar{B}^0$ components by 0.993 (in categories 1-3) and the mixed components (category 4) by 1.035.

Finally, we scale each category by the ratio of the number of $B\overline{B}$ events in the data to the generic Monte Carlo, $(3.0 \times 10^6)/(15.5 \times 10^6) = 0.196$. Table 4.11

shows each category and the rates that we use to normalize them; it also gives the normalization for each category.

Correlated Background

Correlated background events are those in which the D^{*0} and lepton are daughters of the same B, but the decay was not $B \to D^* \ell \nu$ or $B \to D^* X \ell \nu$. In order to have the correct charge correlation with the D^{*0}, the lepton must come from a secondary decay. The most common sources are $B \to D^* \tau \nu$ followed by leptonic τ decay, and $B \to D^* D_s^{(*)}$ followed by semileptonic decay of the $D_s^{(*)}$. We get the $\cos\theta_{B-D^*\ell}$ distribution for this background from generic Monte Carlo. The modes and branching fractions are listed in Table 4.12.

Fake Lepton Background

Fake lepton background arises when a hadron is misidentified as a lepton and is then used in our reconstruction. This background was measured by carrying out our analysis on the same data sample and choosing hadrons to be the lepton candidate instead of identified leptons. We normalize the resulting $\cos\theta_{B-D^*\ell}$ distributions using measured rates of hadrons faking electrons or muons. Tim Riehle has measured the momentum-dependent fake probability [37] for kinematically-identified samples of hadrons in the data: pions are identified using $K_S^0 \to \pi^+\pi^-$ decays, kaons using $D^{*+} \to D^0\pi^+ \to K^-\pi^+\pi^+$, and protons from $\Lambda \to p\pi^-$. We convolute the fake probabilities with the momentum spectrum of hadronic tracks

Table 4.11: The normalizations for uncorrelated background. The (a) and (b) sub-categories represent the low (a) and high (b) D^{*0} momentum bins.

Category	D^{*0} Rate	Lepton Rate	$N_{B\bar{B}}$	$B^0\bar{B}^0$ Mixing	Normalization
1a (B^+B^-)	lower-vertex (low p_{D^*})	secondary	0.196	-	0.133
1a ($B^0\bar{B}^0$)	lower-vertex (low p_{D^*})	secondary	0.196	unmixed	0.132
1b (B^+B^-)	lower-vertex (high p_{D^*})	secondary	0.196	-	0.158
1b ($B^0\bar{B}^0$)	lower-vertex (high p_{D^*})	secondary	0.196	unmixed	0.157
2 (B^+B^-)	upper-vertex	primary	0.196	-	0.196
2 ($B^0\bar{B}^0$)	upper-vertex	primary	0.196	unmixed	0.195
3a (B^+B^-)	lower-vertex×swapped (low p_{D^*})	primary	0.196	-	0.150
3a ($B^0\bar{B}^0$)	lower-vertex×swapped (low p_{D^*})	primary	0.196	unmixed	0.149
3b (B^+B^-)	lower-vertex×swapped (high p_{D^*})	primary	0.196	-	0.225
3b ($B^0\bar{B}^0$)	lower-vertex×swapped (high p_{D^*})	primary	0.196	unmixed	0.223
4a (B^0B^0)	lower-vertex (low p_{D^*})	primary	0.196	mixed	0.165
4b (B^0B^0)	lower-vertex (high p_{D^*})	primary	0.196	mixed	0.195
5b	-	-	0.196	-	0.196

Table 4.12: Modes that contribute to the correlated background, and their branching fractions.

Mode	`decay.dec` Branching Fraction (%)
$B \to D^{*0} X \tau\nu$	1.65
$B \to D_s D^{*0}$	1.39
$B \to D_s^* D^{*0}$	3.08
$B \to D^{*0} D^{(*)} K^{(*)}$	5.6
$B \to D^{*0} D^*$	3.4
$B \to D^{*0}\pi;\ \pi \to \mu\nu$	0.47
$B \to D^{*0}$ plus γ conversion	—

in events with an identified D^{*+} to obtain an average fake rate of 0.035% for a hadronic track to fake an electron and 0.68% to fake a muon.

4.4.2 $D^*\ell\nu$ and $D^*X\ell\nu$ $\cos\theta_{B-D^*\ell}$ distributions

The $\cos\theta_{B-D^*\ell}$ distributions of $D^*\ell\nu$ and $D^*X\ell\nu$ events are obtained from the $D^*\ell\nu$ and $D^*X\ell\nu$ Monte Carlo samples. Since the other B in the event also decays, the $\cos\theta_{B-D^*\ell}$ distributions can contain the same backgrounds listed above.

The largest background contribution to the signal $\cos\theta_{B-D^*\ell}$ distributions comes from the combinatoric background. We have found that the normalizations of the Δm sideband required to remove this background from the simulated events are consistent with those we use to remove it from data events. The normalizations obtained from Δm fits of the data can fluctuate statistically around their true values, and these fluctuations affect the amount of this background that we assign. In order to keep the amount of this background consistent between data and simulated events, we use the normalizations obtained with the data and the $\cos\theta_{B-D^*\ell}$ distributions from the Δm sideband of the simulated events to remove the combinatoric background from the $\cos\theta_{B-D^*\ell}$ distributions of all simulated events.

We veto the small contribution of all other backgrounds to the $D^*\ell\nu$ and $D^*X\ell\nu$ $\cos\theta_{B-D^*\ell}$ distributions using generator-level information.

4.4.3 $\cos\theta_{B-D^*\ell}$ fit results

With the $\cos\theta_{B-D^*\ell}$ distributions of $D^{*0}\ell\nu$, $D^*X\ell\nu$, and the backgrounds, we fit the data in bins of w. The results of the $\cos\theta_{B-D^*\ell}$ fits are shown for each w bin in Figures 4.7 through 4.11. We use the normalization of the $D^{*0}\ell\nu$ and $D^*X\ell\nu$ components and the area of the respective $\cos\theta_{B-D^*\ell}$ distributions to extract the $D^*\ell\nu$ and $D^*X\ell\nu$ yields. The $D^*\ell\nu$ and $D^*X\ell\nu$ yields are given in Table 4.13. The fits are good in terms of both the χ^2 (calculated after the likelihood fit) and the agreement of the data and fit distributions outside the fit regions.

Cross-checks of the $\cos\theta_{B-D^*\ell}$ Fits

In order to check that the $D^*X\ell\nu$ model in our Monte Carlo is consistent with the data, we plot the $D^*X\ell\nu$ yield from the $\cos\theta_{B-D^*\ell}$ fits over the $D^*X\ell\nu$ yield

Table 4.13: The results of the fit to the $\cos\theta_{B-D^*\ell}$ distribution in each w bin. The fits are likelihood fits; the quoted χ^2's are calculated from the results of the fit.

w Range	$D^{*0}\ell\nu$ Yield	$D^*X\ell\nu$ Yield	χ^2/dof
1.00 - 1.05	69.7 ± 19.6	-20.6±19.2	17.3/17
1.05 - 1.10	122.8 ± 20.7	-1.0±22.0	13.4/17
1.10 - 1.15	110.6 ± 18.8	23.3±18.2	23.7/17
1.15 - 1.20	127.5 ± 18.7	4.5±13.3	17.6/17
1.20 - 1.25	123.4 ± 17.1	10.6±14.6	12.8/17
1.25 - 1.30	102.6 ± 16.2	14.6±17.9	13.5/17
1.30 - 1.35	99.8 ± 15.1	-14.0±13.3	14.8/13
1.35 - 1.40	113.8 ± 15.6	-4.0±13.2	11.3/9
1.40 - 1.45	62.0 ± 15.2	-0.8±14.7	6.0/7
1.45 - 1.51	21.4 ± 16.4	17.6±14.6	1.6/5

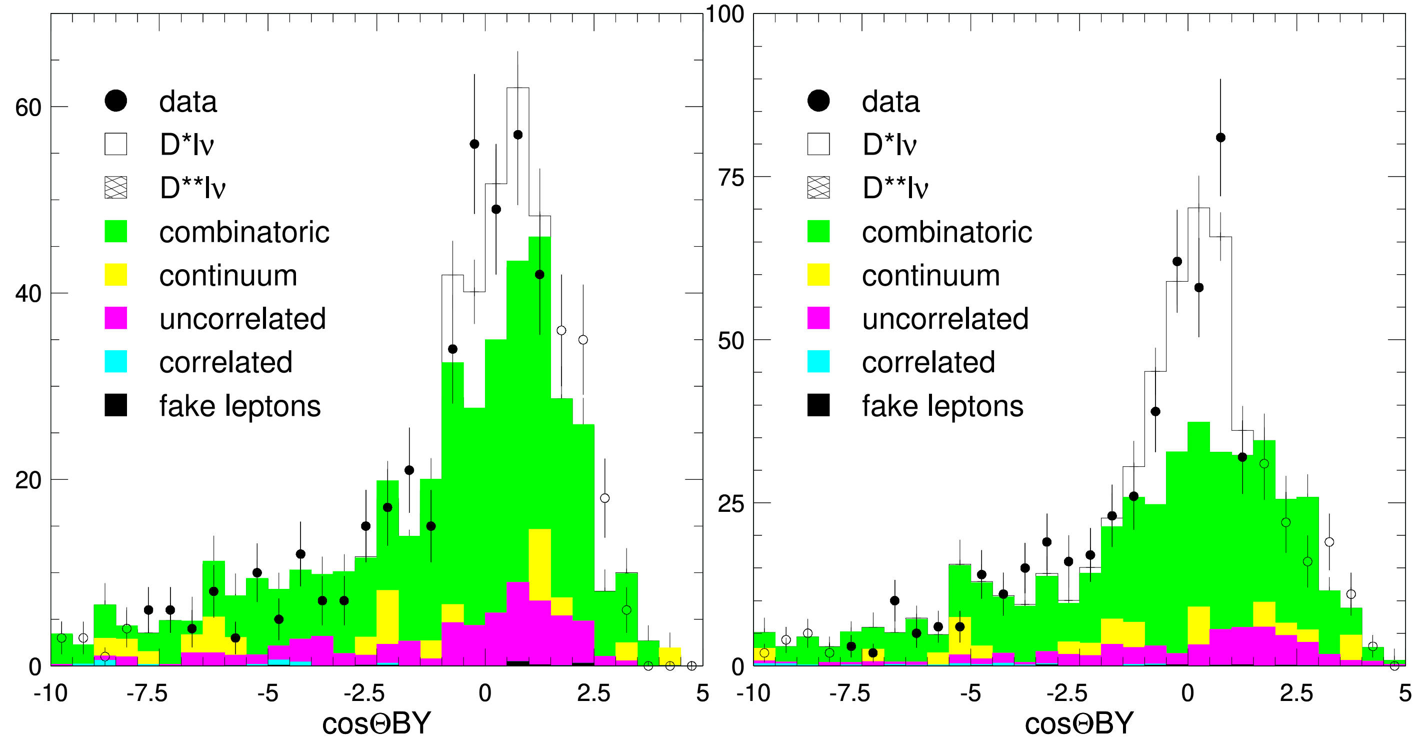

Figure 4.7: $\cos\theta_{B-D^*\ell}$ fit results for the first and second w bins. The solid circles represent the $\cos\theta_{B-D^*\ell}$ fit region.

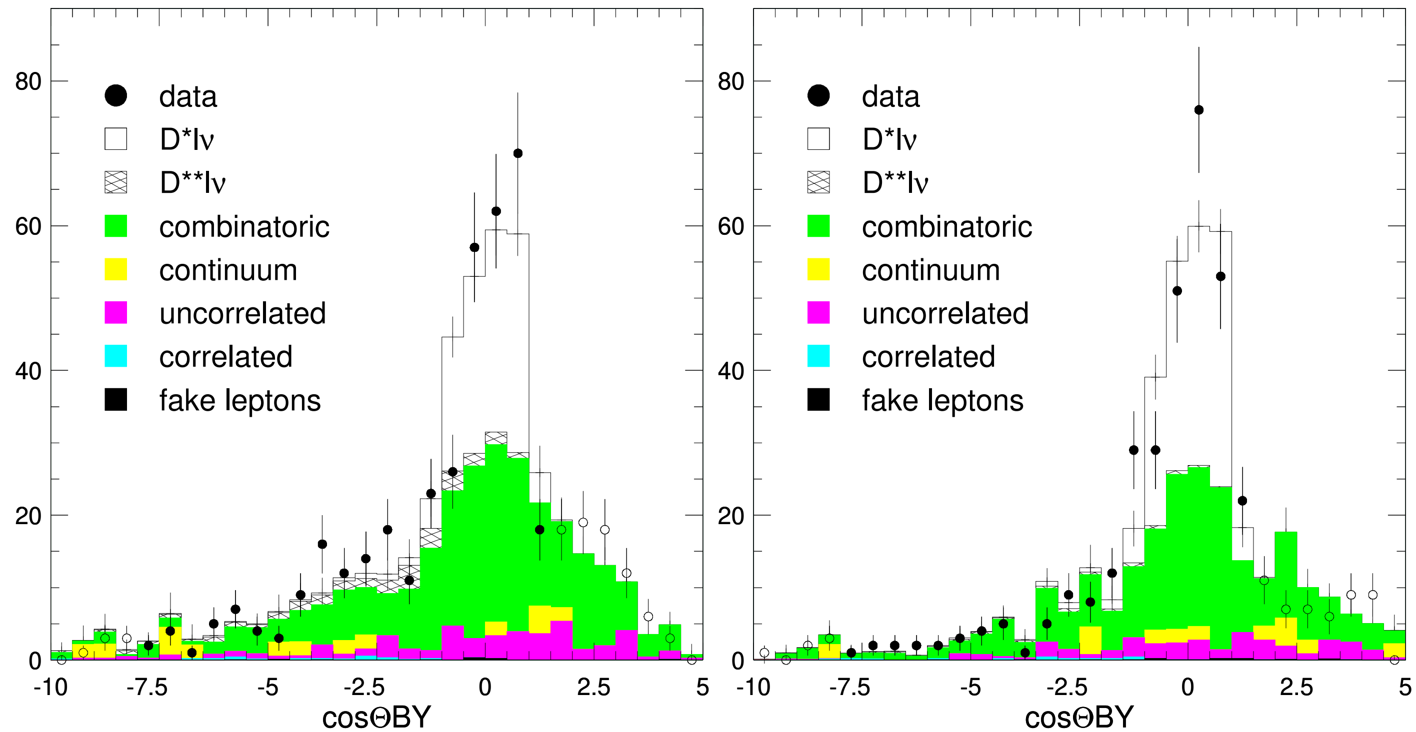

Figure 4.8: $\cos\theta_{B-D^*\ell}$ fit results for the Third and Fourth w bins. The solid circles represent the $\cos\theta_{B-D^*\ell}$ fit region.

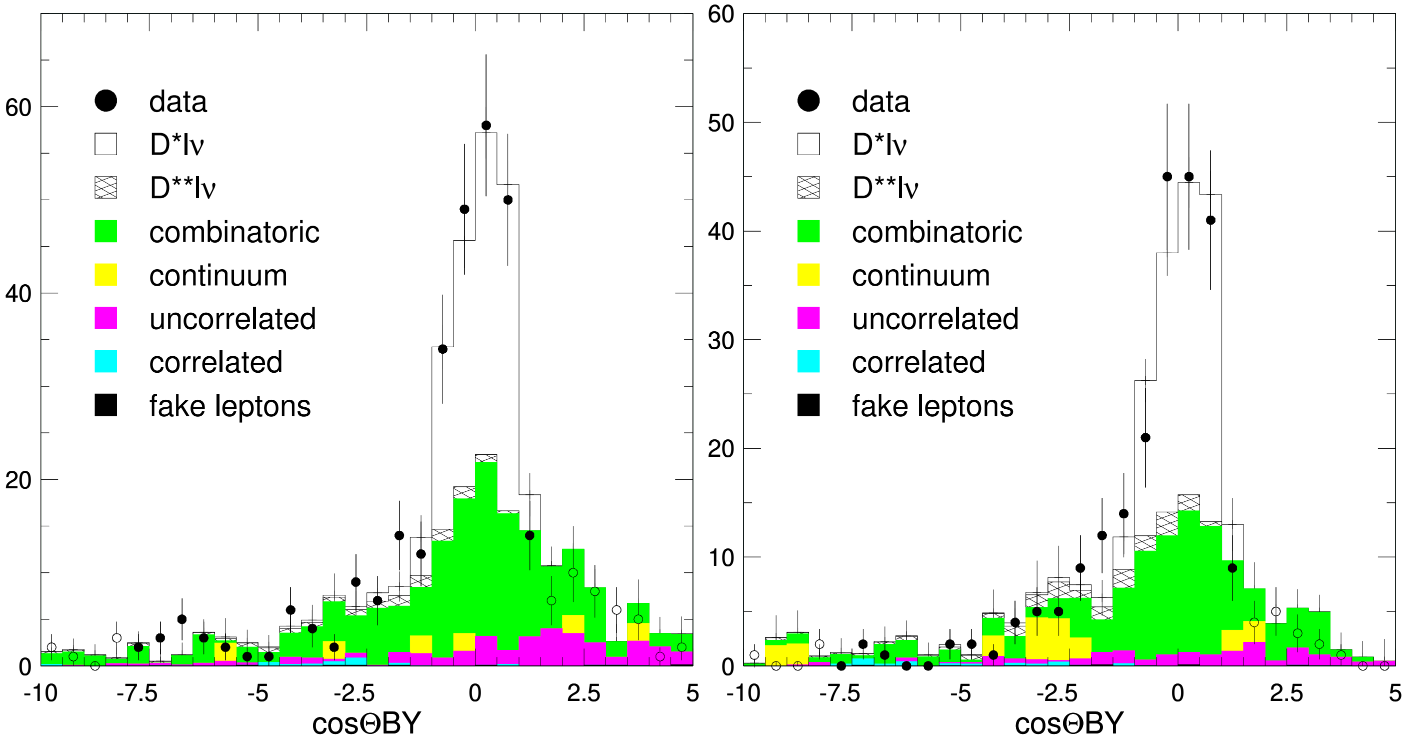

Figure 4.9: $\cos\theta_{B-D^*\ell}$ fit results for the fifth and sixth w bins. The solid circles represent the $\cos\theta_{B-D^*\ell}$ fit region.

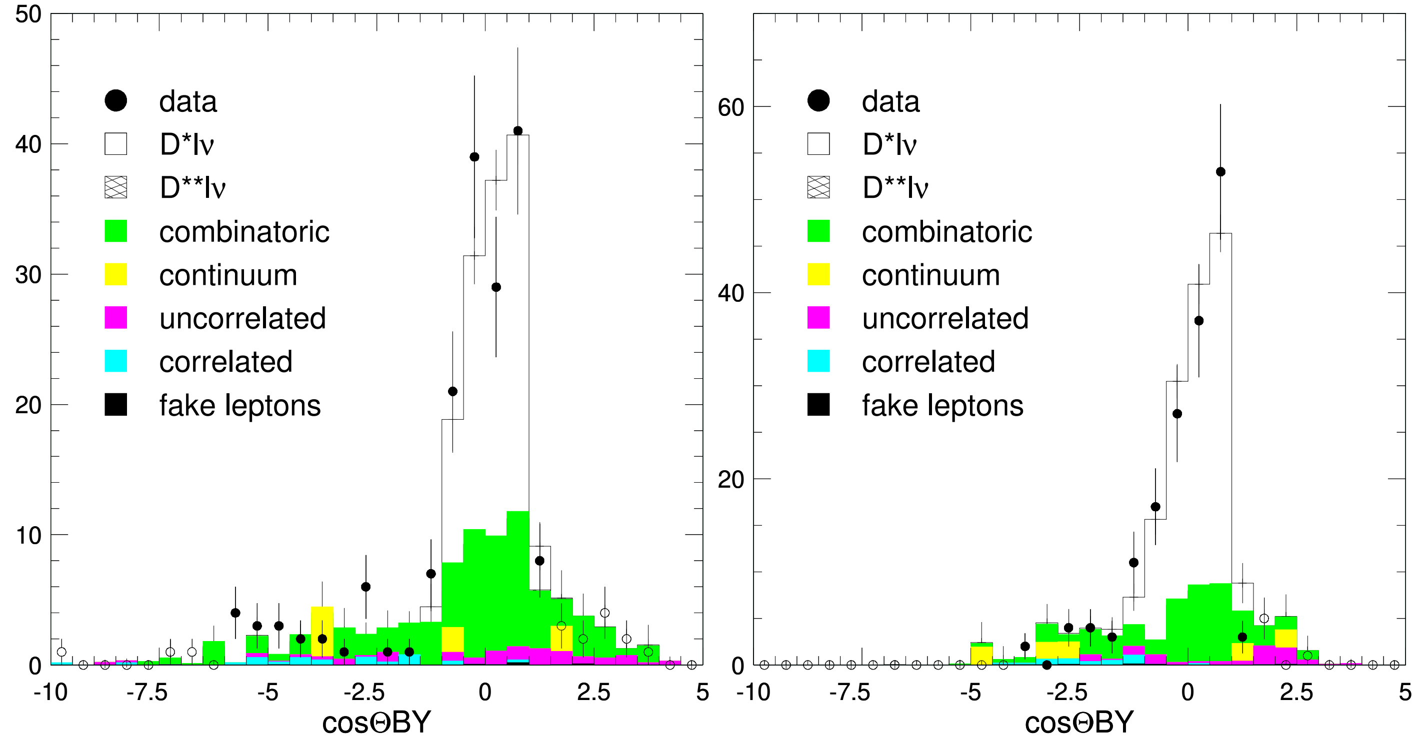

Figure 4.10: $\cos\theta_{B-D^*\ell}$ fit results for the seventh and eighth w bins. The solid circles represent the $\cos\theta_{B-D^*\ell}$ fit region.

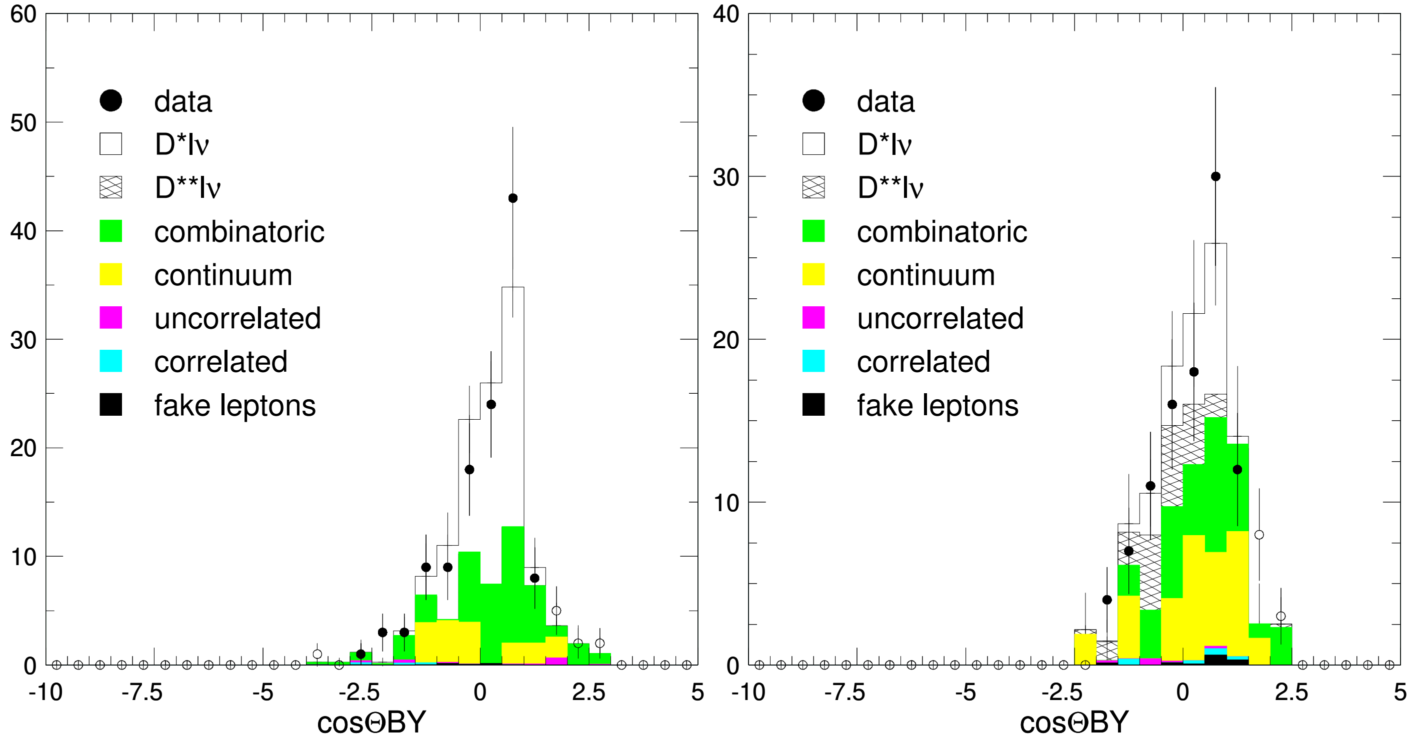

Figure 4.11: $\cos\theta_{B-D^*\ell}$ fit results for the ninth and tenth w bins. The solid circles represent the $\cos\theta_{B-D^*\ell}$ fit region.

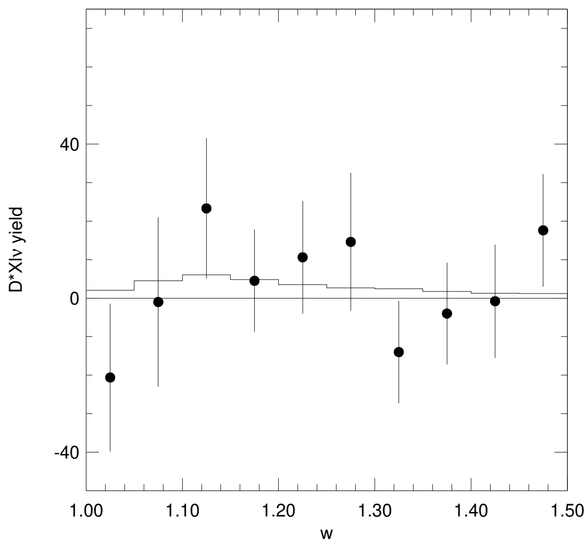

Figure 4.12: The points show the $D^*X\ell\nu$ yield in the data from the $\cos\theta_{B-D^*\ell}$ fits, and the line shows the $D^*X\ell\nu$ distribution in w from the Monte Carlo. The plots have been normalized to equal area.

predicted by the Monte Carlo in bins of w. This plot is shown in Figure 4.12. The agreement between the data and Monte Carlo distributions is good.

We also plot the results of the $\cos\theta_{B-D^*\ell}$ fits in terms of the D^{*0} energy, the lepton momentum, and the angle between the lepton momentum in the virtual W's rest frame and the flight direction of the virtual W in the B's rest frame ($\cos\theta_\ell$). These distributions are related to the $B \to D^*\ell\bar{\nu}$ model used in the fits. Since we do not do our fit with these variables, agreement between the fit results and the data is a good indication that our fit correctly determines the $D^*\ell\nu$ yield. For each variable, we plot the sum of the results of the w bin fits in the signal region and the $\cos\theta_{B-D^*\ell}$ range outside of the signal region but included in the fit. The D^{*0} energy plots are shown in Figure 4.13, the lepton momentum plots are shown

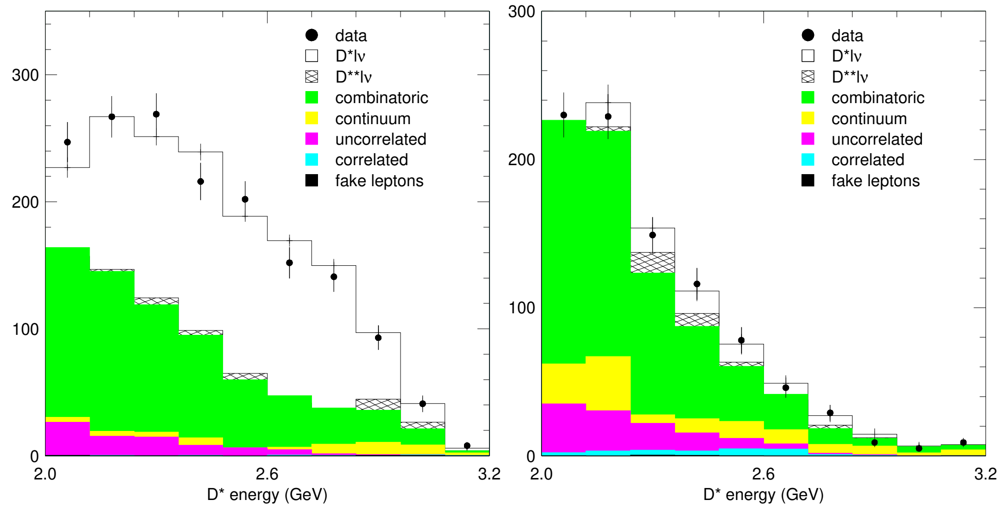

Figure 4.13: The sum of the results of the $\cos\theta_{B-D^*\ell}$ fits in D^{*0} energy in (a) the signal region and (b) the $\cos\theta_{B-D^*\ell}$ region outside the signal region but within the fit range.

in Figure 4.14, and the $\cos\theta_\ell$ plots are shown in Figure 4.15. The agreement of the fit distribution with the data distribution is good in all plots.

4.5 Extracting $|V_{cb}|$

The basics of our measurement of $|V_{cb}|$ were discussed in Section 2.2. To review, we measure $d\Gamma/dw$ (Equation 2.10) in the data and then fit the distribution using the parameterizations of $h_{A_1}(w)$, $R_1(w)$, and $R_2(w)$ given in equations 2.20, 2.21, and 2.22, keeping $|V_{cb}|F(1)$ and $\rho^2_{A_1}$ as free parameters.

CLEO II is not 100% efficient at reconstructing $B \to D^*\ell\bar{\nu}$ decays, and there is some measurement error in the decays that we do reconstruct, leading to smearing in the reconstructed value of w. This effect is illustrated in Figure 4.16. Some

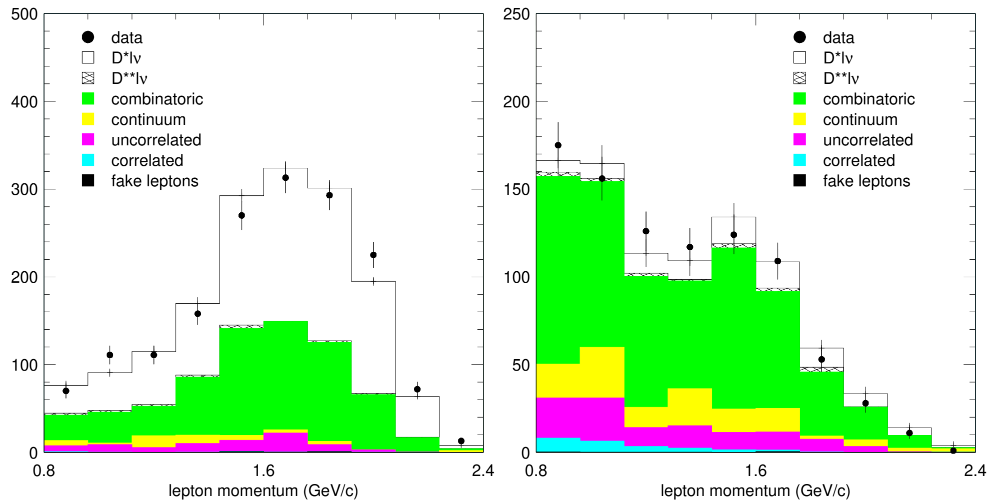

Figure 4.14: The sum of the results of the $\cos\theta_{B-D^*\ell}$ fits in lepton momentum in (a) the signal region and (b) the $\cos\theta_{B-D^*\ell}$ region outside the signal region but within the fit range.

of this smearing comes from the inherent resolution of the detector, and some comes from our assumptions about the direction of the B when we calculate w. We include an efficiency matrix in our fit, ϵ_{ij}, that includes our estimate of the efficiency for reconstructing $B \to D^* \ell \bar{\nu}$ events and the smearing on w.

The efficiency matrix ϵ is calculated using $D^*\ell\nu$ signal Monte Carlo. A matrix element ϵ_{ij} represents the efficiency for reconstructing a $D^*\ell\nu$ event in the jth w bin when its true w falls in the ith w bin. To be consistent with our method for finding the $\cos\theta_{B-D^*\ell}$ distribution of $D^*\ell\nu$ events, described in Section 4.4.2, we subtract the combinatoric background in the simulated events using the Δm sideband and the data normalizations. We veto all other backgrounds using generator-level knowledge of the simulated events. A single element of the efficiency matrix

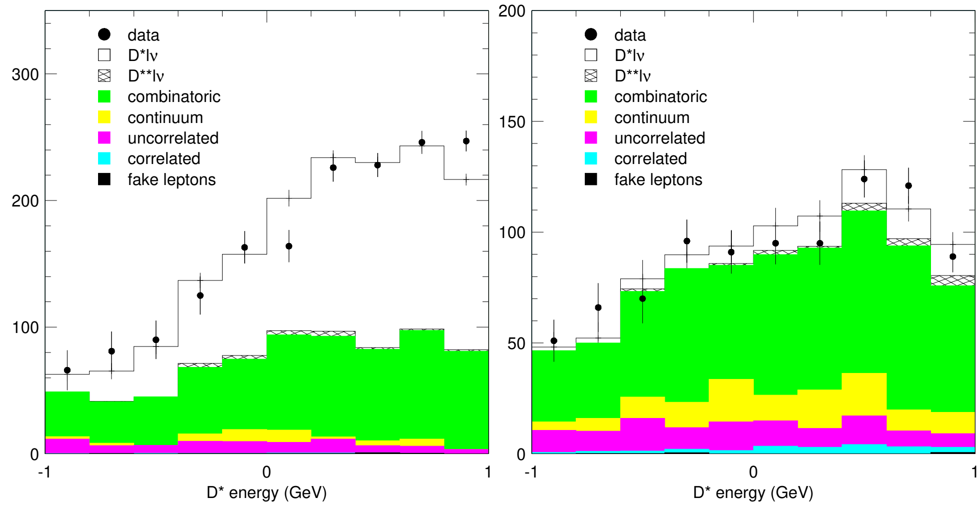

Figure 4.15: The sum of the results of the $\cos\theta_{B-D^*\ell}$ fits in $\cos\theta_\ell$ in (a) the signal region and (b) the $\cos\theta_{B-D^*\ell}$ region outside the signal region but within the fit range. In the limit that the masses of the lepton and anti-neutrino are zero, the weak decay requires them to have left-handed and right-handed helicity, respectively. $\cos\theta_\ell = 1$ is favored in $B \to D^*\ell\bar{\nu}$ decays because the spin of the D^{*0} allows the W to have left-handed helicity required by its decay to a lepton-anti-neutrino pair.

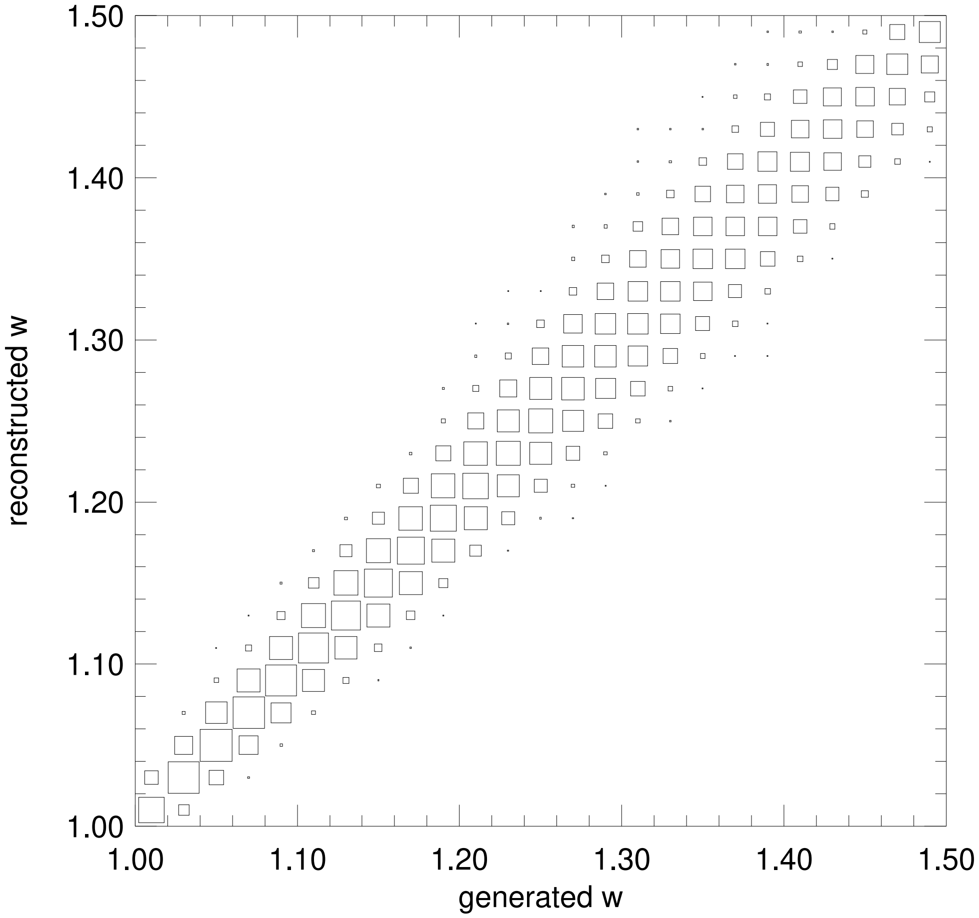

Figure 4.16: Reconstructed w versus generated w for $B \to D^* \ell \bar{\nu}$ Monte Carlo events.

is thus calculated using

$$\epsilon_{ij} = (S_i^{sig} - n_i S_i^{side})/S_j, \tag{4.7}$$

where S_i^{sig} and S_i^{side} are the number of non-vetoed candidates reconstructed in the ith w bin in the Δm signal and sideband regions, respectively, n_i is the normalization of the Δm sideband region (from the data Δm fits), and S_j is the number of $D^*\ell\nu$ events generated in the jth w bin. When finding S_i^{sig} and S_i^{side} we include only $D^{*0}\ell\nu$ decays where either there is no final state radiation or where the emitted photon has an energy less than 100 MeV. We correct the efficiency by -1.26% to account for final-state radiation in the $D^0 \to K^-\pi^+$ decay; this efficiency correction in determined with PHOTOS and is consistent with the treatment of final-state radiation in the two measurements that we average to get $\mathcal{B}(D^0 \to K^-\pi^+)$. The efficiency is corrected by generated w bin for slow-π^0 efficiency differences between data and Monte Carlo $B\overline{B}$ events. The event environment, defined as the number and distribution of nearby showers and calorimeter hits, is known to differ between data and Monte Carlo $B\overline{B}$ events. This environment affects the efficiency by providing showers that can overlap with the showers of the daughter photons and change their energy and shape. We measure this efficiency difference by "embedding" (inserting) Monte Carlo-generated slow-π^0 showers with kinematic distributions appropriate to $D^*\ell\nu$ decay into samples of hadronic events selected from our data and simulated $B\overline{B}$ events. For the π^0's embedded in the data events, we adjust the calorimeter noise and add a smearing to the crystal gains so that our simulation reproduces the distributions of `E9/E25` and $m_{\gamma\gamma}$ for slow π^0's. The efficiency is measured in bins of w using our analysis requirements for the recon-

Table 4.14: The corrections applied to the efficiency matrix, in percent.

w (generated)	Efficiency Correction (%)
1.00-1.05	-5.3
1.05-1.10	-5.1
1.10-1.15	-3.7
1.15-1.20	2.2
1.20-1.25	1.3
1.25-1.30	6.2
1.30-1.35	1.4
1.35-1.40	2.3
1.40-1.45	-4.1
1.45-1.51	-5.4
all	-0.6

structed slow pion combined with generated quantities for the remainder of the $D^{*0}\ell\nu$ decay. In this way we correctly weight the efficiency for kinematic effects of our cuts. We measure the efficiency difference for these embedded showers and apply these differences as efficiency corrections. This study is described in greater detail in Appendix B. The efficiency corrections are given in Table 4.14, and the efficiency matrix is given in Table 4.15.

Our fit minimizes

$$\chi^2 = \sum_{i=1}^{10} \frac{[N_i^{obs} - \sum_{j=1}^{10} \epsilon_{ij} N_j]^2}{\sigma^2_{N_i^{obs}}}, \tag{4.8}$$

Table 4.15: The efficiency matrix used in the $|V_{cb}|$ fit. The i index gives the generated w bin, and the j index gives the reconstructed w bin. The efficiencies are given in percent. A Δm sideband subtraction is performed using the normalizations from the data Δm fits; this is the source of the scatter in the diagonal elements.

	1	2	3	4	5	6	7	8	9	10
1	11.15	1.55	0.00	0.01	0.00	0.00	0.00	0.00	0.00	0.00
2	0.71	9.36	1.58	0.00	0.00	0.00	0.00	0.00	0.00	0.00
3	0.02	1.12	8.01	1.67	0.00	0.01	0.00	0.00	0.00	0.00
4	0.00	0.00	1.42	7.04	2.05	0.01	0.00	0.00	0.00	0.00
5	0.01	0.00	0.00	1.60	6.44	2.16	0.03	0.00	0.00	0.00
6	0.01	0.00	0.00	0.00	1.88	5.93	2.41	0.07	0.00	0.00
7	0.01	0.00	0.01	0.01	0.01	1.93	4.84	2.23	0.06	0.00
8	0.00	0.00	0.00	0.00	0.00	0.01	1.86	5.11	2.12	0.04
9	0.00	0.00	0.00	0.01	0.00	0.00	0.00	1.89	4.80	1.34
10	0.00	0.00	0.00	0.00	0.01	0.00	0.01	0.06	1.51	5.72

where N_i^{obs} is the $D^{*0}\ell\nu$ yield in the i^{th} w bin, N_j is the predicted number of decays in the j^{th} w bin (calculated from $d\Gamma/dw$), and the matrix ϵ accounts for the reconstruction efficiency and the smearing in w. In addition, we take advantage of the recent CLEO measurement of $(f_{+-}/f_{00})(\tau_{B^-}/\tau_{B^0})$ [16] (where $f_{+-} = \mathcal{B}(\Upsilon(4s) \to B^+B^-)$ and $f_{00} = \mathcal{B}(\Upsilon(4s) \to B^0\bar{B}^0)$) and add a term to χ^2 constraining this ratio. We assume that $f_{00} = 1 - f_{+-}$.

Explicitly, N_j is

$$N_j = 4f_{+-}N_{\Upsilon(4S)}\,\mathcal{B}_{D^{*0}}\,\mathcal{B}_{D^0}\,\mathcal{B}_{\pi^0}\,\tau_{B^+}\int_{w_j} dw\frac{d\Gamma}{dw}, \tag{4.9}$$

where τ_{B^+} is the B^+ lifetime, $\mathcal{B}_{D^{*0}}$ is the $D^{*0} \to D^0\pi^0$ branching fraction, $\mathcal{B}_{D^0}$ is the $D^0 \to K^-\pi^+$ branching fraction, $\mathcal{B}_{\pi^0}$ is the $\pi^0 \to \gamma\gamma$ branching fraction, and $N_{\Upsilon(4S)}$ is the number of $\Upsilon(4S)$ events in the sample. The values that we use for the B lifetimes and the various branching fractions are listed in Table 4.16. Because the branching fraction given for $D^0 \to K^-\pi^+$ in [1] does not take into account the different treatment of final-state radiation by the different measurements, we take a weighted average of two $D^0 \to K^-\pi^+$ branching fraction from measurements made at CLEO [38] and ALEPH [39] in which we know how final-state radiation was treated.

4.5.1 Results

The results of the fit can be seen in Figure 4.17. We find the following:

$$|V_{cb}|\mathcal{F}(1) = 0.0427 \pm 0.0025 \tag{4.10}$$

$$\rho^2_{A_1} = 1.54 \pm 0.18 \tag{4.11}$$

Table 4.16: The B^+ lifetime and the branching fractions used in the $|V_{cb}|$ fit. All values are from [1] except $\mathcal{B}(D^0 \to K^-\pi^+)$, which is explained in the text.

τ_{B^+}	1.653±0.028 ps
τ_{B^0}	1.548±0.032 ps
$\mathcal{B}(D^{*0} \to D^0\pi^0)$	(61.9±2.9)%
$\mathcal{B}(D^0 \to K^-\pi^+)$	(3.86±0.11)%
$\mathcal{B}(\pi^0 \to \gamma\gamma)$	(98.798±0.032)%

$$f_{+-} = 0.510 \pm 0.018 \tag{4.12}$$

$$\chi^2 = 8.8/8\,\mathrm{dof}, \tag{4.13}$$

where the errors are statistical. The correlation coefficients between the results are $C(|V_{cb}|F(1), \rho^2_{A_1}) = 0.832$, $C(|V_{cb}|F(1), f_{+-}) = -0.299$, and $C(\rho^2_{A_1}, f_{+-}) = 0.000$. Using $|V_{cb}|F(1)$ and $\rho^2_{A_1}$ and integrating $d\Gamma/dw$ over all w gives $\Gamma = 0.0400 \pm 0.0027\,\mathrm{ps}^{-1}$, which implies a $B^- \to D^{*0}\ell\nu$ branching fraction of 6.62%. Using $\mathcal{F}(1) = 0.913 \pm 0.042$ [6], we find

$$|V_{cb}| = 0.0468 \pm 0.0035 \tag{4.14}$$

The systematic uncertainties on these measurements are the subject of the next chapter.

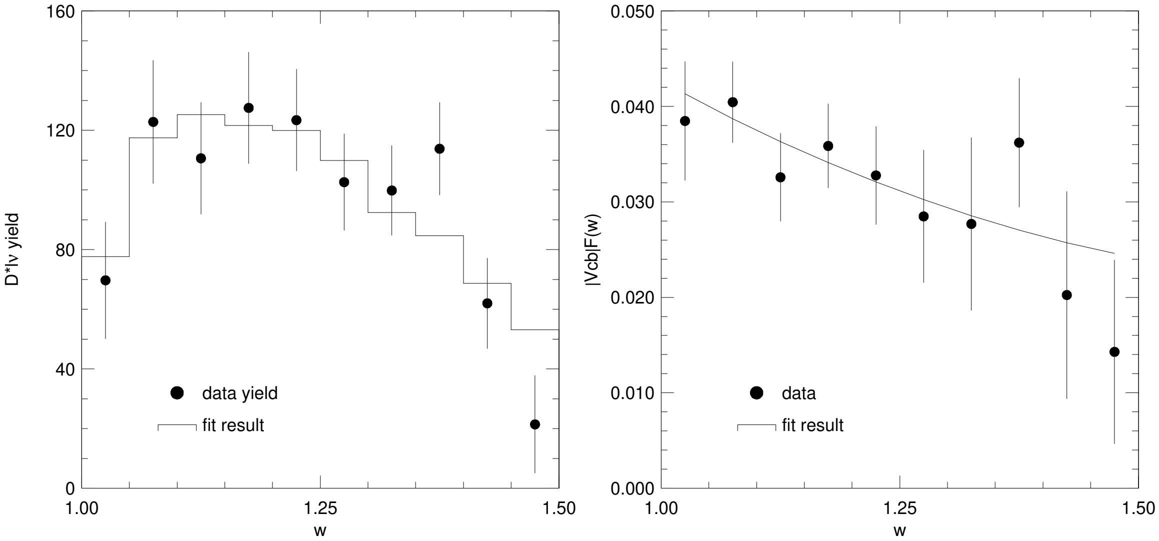

Figure 4.17: The results of the $|V_{cb}|$ fit. The left plot shows the $D^{*0}\ell\nu$ yield versus w (points) and the results of the fit (line). The right plot shows $|V_{cb}|\mathcal{F}(w)$ for our efficiency-corrected data points and from the fit (line).

CHAPTER 5

SYSTEMATIC UNCERTAINTIES

The biggest challenge in this analysis is to have a systematic uncertainty that is comparable in size to our statistical uncertainty. We divide these uncertainties into three main groups: uncertainty from our various background subtractions, uncertainty on our efficiency for reconstructing $D^{*0}\ell\nu$ decays, and uncertainties that come about on our results from uncertainties on constants in our $|V_{cb}|$ fit (like the $D^{*0} \to D^0\pi^0$ branching fraction). There are also uncertainties from the parameterization of the $B \to D^*\ell\bar{\nu}$ form factors, the model we use to simulate the final-state radiation, and the $D^*X\ell\nu$ decay model. Section 5.1 describes the uncertainties from the backgrounds, Section 5.2 describes the uncertainties from our estimate of the reconstruction efficiency, and Section 5.3 describes the uncertainties from the branching fractions, lifetimes, and form factor ratios. Section 5.4 describes the remaining uncertainties. Finally, Section 5.5 summarizes all of the sources of uncertainty and gives the totals.

Our basic method for determining most of these uncertainties is to vary the $\cos\theta_{B-D^*\ell}$ normalization or distribution of some component and/or the $D^{*0}\ell\nu$ efficiency and to repeat our analysis. We then use the change in our results to determine the uncertainty. In the following, we will frequently give the change in our results when we vary a parameter with a Gaussian uncertainty in only one direction. Experience has shown us that most parameters with Gaussian uncertainties automatically lead to symmetric uncertainties on our measurements; the exceptions are $R_1(1)$ and $R_2(2)$, where we must include the correlation between the measurement uncertainties. Unless mentioned, we take all changes from parameter variations to be symmetric.

5.1 Background Uncertainties

5.1.1 Continuum Background

When calculating w for off-resonance events, we scale the energy of the D^* and lepton to reflect the difference in the on- and off-resonance center-of-mass energies. While the momentum distribution of scaled off-resonance particles does not match the distribution of on-resonance particles [40], the difference between the two is smaller than the difference between un-scaled and scaled off-resonance distributions. To assess the systematic uncertainty from this scaling, we compare our results with the scaling to the results we get if we repeat the analysis without scaling the D^* and lepton energies. We take the systematic uncertainty to be half of the difference. The change in the results and the uncertainties assigned are listed in Table 5.1. We assign an uncertainty of 0.15% on $|V_{cb}|F(1)$ from this source.

Table 5.1: The change in our results due to not scaling the D^* and lepton energies for off-resonance events and the uncertainties we assign for the continuum background, which is equal to half the change.

	$\lvert V_{cb}\rvert F(1)(\%)$	$\rho^2(\%)$	$\Gamma(B \to D^*\ell\nu)(\%)$
Change	-0.30	-0.67	-0.01
Uncertainty	0.15	0.33	0.00

5.1.2 Combinatoric Background

In assessing the uncertainty on our result from the combinatoric background, we want to consider how well the Δm sideband $\cos\theta_{B-D^*\ell}$ distribution reproduces the distribution of the background in the Δm signal region and how well our Δm fit does at finding the normalization of the Δm sideband. As mentioned before, the D^{*0} momentum distribution of the combinatoric background in the Δm sideband has a slightly lower mean momentum than the background in the Δm signal region, leading to a slightly different $\cos\theta_{B-D^*\ell}$ distribution. Because this effect is kinematic, the generic Monte Carlo does a good job of predicting the distribution difference and is a good place to test the effect of this difference. For the same reason, the Monte Carlo also reproduces the Δm distribution of the combinatoric background in the data, allowing us to test the functional form that we have chosen for the background. We perform our analysis on the generic Monte Carlo twice, once where we determine the combinatoric background using the procedure outlined in Section 4.4.1 and once where we use the absolutely

Table 5.2: The results of the study of combinatoric background using the generic Monte Carlo.

Source	$\lvert V_{cb}\rvert F(1)(\%)$	$\rho^2(\%)$	$\Gamma(B \to D^*\ell\nu)(\%)$
Difference	-1.54	-4.24	+0.20
Statistical Uncertainty	1.56	2.27	1.51
Uncertainty	2.19	4.81	1.52

normalized true tagged combinatoric background in place of the Δm sideband distribution. When performing the $|V_{cb}|$ fit, we use the same linear form factor that was used to generate the $B \to D^*\ell\bar{\nu}$ decays in the generic Monte Carlo. We compare the results from the two analyses and take any differences as part our systematic uncertainty. The statistics of the study are limited, and we find statistical uncertainties on the shifts of the same order as the shifts. To include these errors, we add in quadrature the statistical uncertainties of this study. The results of this study are shown in Table 5.2.

There are additional uncertainties in the normalizations due to the Δm fits to the data distributions. The Δm lineshape from $D^{*0}\ell\nu$ Monte Carlo can affect the outcome of the Δm fit. To assess this effect, we first vary the width we add to the peak of the signal Monte Carlo Δm distribution by its statistical uncertainty and repeat the Δm fits. We then repeat the data analysis using the new normalizations and assign any change in the result as a systematic uncertainty. Also, Δm appears to peak slightly higher in the Monte Carlo than the data; we shift it down by 0.15 MeV/c^2 and take the change in our result as an uncertainty. Since there may be small differences in the Δm distributions of combinatoric background between data and Monte Carlo, we try other functional forms for the background distribution. The two forms we use are $a(\Delta m - m_{\pi^0})^{1/2} + b(\Delta m - m_{\pi^0}) + c(\Delta m - m_{\pi^0})^{3/2}$, where a, b, and c are the free parameters, and $a(\Delta m - m_{\pi^0})^{1/2} + b(\Delta m - m_{\pi^0})$, where a and b are the free parameters. We again repeat the analysis with the new normalizations and note the changes in our results. We take the larger excursion as our systematic uncertainty. The uncertainties from the changes to the Δm fit are shown in Table 5.3.

The final contribution to the systematic uncertainty from our combinatoric background estimate comes from the decays modes other than $D \to K\pi$ that are reconstructed in our $m_{K\pi}$ signal region. The specific modes were given in Table 4.8. We find the total contribution to our $D^{*0}\ell\nu$ yield from this source is $0.5{\pm}0.3\%$. We add the yield and uncertainty in quadrature to get a 0.6% uncertainty on our $B \to D^*\ell\bar{\nu}$ yield, which translates to a 0.3% uncertainty on $|V_{cb}|F(1)$.

We assign a total uncertainty of 2.24% to $|V_{cb}|F(1)$ from the combinatoric background. The systematic uncertainties from the combinatoric background are summarized in Table 5.4.

5.1.3 Uncorrelated Background

The uncertainties from the uncorrelated background come from the uncertainties on the normalizations we use for the various components. To determine the uncertainty on our results from these normalizations, we vary the D^* and lepton rates,

Table 5.3: The contributions to the systematic uncertainties from the combinatoric background due to the Δm fit.

Variation	$\lvert V_{cb}\rvert F(1)(\%)$	$\rho^2(\%)$	$\Gamma(B \to D^* \ell\nu)(\%)$
Δm Peak Smearing	0.16	0.19	0.48
Δm Peak Shift	0.01	0.08	0.40
Change from Background Functional Form:			
$a(\Delta m - m_{\pi^0})^{1/2} + b(\Delta m - m_{\pi^0}) + c(\Delta m - m_{\pi^0})^{3/2}$	-0.23	+0.41	-0.82
$a(\Delta m - m_{\pi^0})^{1/2} + b(\Delta m - m_{\pi^0})$	-0.27	+0.53	-1.01
Uncertainty from Functional Form	0.27	0.53	1.01
Δm Fit Uncertainty	0.31	0.57	1.19

Table 5.4: Summary of systematic uncertainties due to the combinatoric background. We add the components in quadrature to get the total.

Source	$\lvert V_{cb}\rvert F(1)(\%)$	$\rho^2(\%)$	$\Gamma(B \to D^*\ell\nu)(\%)$
Generic Monte Carlo Study	2.19	4.81	1.52
Δm Fit	0.31	0.57	1.19
Leakage from Other D Modes	0.30	0.0	0.60
Total Uncertainty	2.24	4.86	2.01

repeat our analysis, and note the change in our results. The variations we make are:

- We vary the contribution from upper-vertex D^*'s by 50% [41]. When decreasing the upper-vertex rate, we increase the lower-vertex D^* rate by 1.8% to keep the inclusive D^* rate constant. We do this separately for the low and high D^* momentum bins.

- We vary the inclusive D^* rate by one sigma separately for the low and high D^* momentum bins.

- We vary the primary lepton rate by one sigma, changing the secondary lepton rate by 29% to keep the total lepton rate (10.52$\pm$0.44%) constant. The change to the secondary rate is quite conservative, since the uncertainty on that rate is only 8/to do this because it makes the maximal change to the $\cos\theta_{B-D^*\ell}$ distribution.

- We vary the total lepton rate by one sigma.
- We vary the rate for K-π exchange in D^*'s by one sigma in each D^* momentum bin.
- We vary χ_d by one sigma.
- We vary the "miscellaneous" category by 100%.

The effects on the results and the total uncertainty from this background are shown in Table 5.5. We find an uncertainty of 0.79% from this background.

5.1.4 Correlated Background

Since the correlated background is so small, we vary the entire contribution by 50% to assess the systematic uncertainty. This results in a change in $|V_{cb}|F(1)$ of 0.13%, which is small compared to most of our other uncertainties. We could vary each mode individually by the measurement uncertainty on its branching fraction, since some of the modes have uncertainties less than 50%, but the improvement of our total uncertainty and would be minimal. The uncertainties from the correlated background are shown in Table 5.6.

5.1.5 Fake Lepton Background

We vary the measured electron and muon fake rates separately by 50%. This is conservative, but it has also almost no effect on our result; the total uncertainty on $|V_{cb}|F(1)$ is 0.04%. The uncertainties are shown in Table 5.7.

Table 5.5: The change in the results when we vary subtraction of the uncorrelated background. We add these changes in quadrature to get the total uncertainty.

Variation	$\sqrt{2f}\lvert V_{cb}\rvert h_{A_1}(1)(\%)$	$\rho^2(\%)$	$2f\Gamma(B \to D^*\ell\nu)(\%)$
Upper-vertex D^* down 50% (low p_{D^*})	+0.60	+0.91	+0.37
Upper-vertex D^* down 50% (high p_{D^*})	+0.06	+0.01	+0.11
Inclusive D^* down 1 stat σ (low p_{D^*})	+0.26	+0.43	+0.14
Inclusive D^* down 1 stat σ (high p_{D^*})	+0.03	-0.01	+0.09
Primary lepton down 1 σ	+0.24	+0.31	+0.20
Total lepton down 1 σ	+0.26	+0.36	+0.20
$K-\pi$ exchange down 1 σ (low p_{D^*})	+0.24	+0.39	+0.13
$K-\pi$ exchange down 1 σ (high p_{D^*})	+0.00	+0.03	+0.02
χ_d down 1 σ	+0.09	+0.13	+0.06
Miscellaneous zero	+0.03	+0.16	-0.10
Total	0.79	1.20	0.53

Table 5.6: The uncertainties from the correlated background.

	$\lvert V_{cb}\rvert F(1)(\%)$	$\rho^2(\%)$	$\Gamma(B \to D^* \ell\nu)(\%)$
Uncertainty	0.13	0.43	0.64

Table 5.7: The changes to our result with variations of the lepton fake rates. We add the changes together in quadrature to get the total uncertainty from the fake lepton background.

Variation	$\lvert V_{cb}\rvert F(1)(\%)$	$\rho^2(\%)$	$\Gamma(B \to D^* \ell\nu)(\%)$
Vary electron fake rate 50%	+0.01	+0.01	+0.01
Vary muon fake rate 50%	+0.04	+0.01	+0.08
Total Uncertainty	0.04	0.01	0.08

5.2 Efficiency Uncertainties

In this section we describe uncertainties to our results that come from uncertainties in the $D^{*0}\ell\nu$ efficiency.

5.2.1 Slow-π^0 Efficiency

The efficiency for reconstructing slow π^0's is the largest source of uncertainty in our analysis. It is tricky to determine this uncertainty with precision because the reconstruction efficiency of these low-energy particles is quite sensitive to the details of our simulation. We have done an extensive study, described in Appendix B, that both improves the simulation of slow π^0's and decreases the efficiency uncertainty

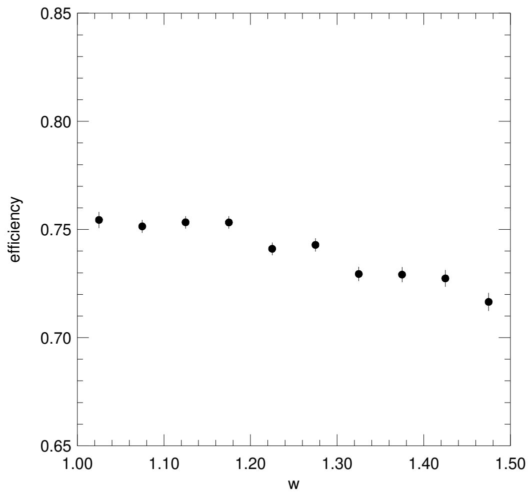

Figure 5.1: The efficiency for reconstructing Monte Carlo π^0's versus w in the region $|\cos\theta| < 0.7071$ for simulated events where the π^0 is the only particle.

(compared to the previous CLEO $|V_{cb}|$ analysis [42]). In this section we give a brief review of our method and the uncertainties on our results caused by uncertainties in the slow-π^0 efficiency.

Neutral slow pions decay to two low-energy photons (30-230 MeV) that are detected in the calorimeter, so unlike charged particles they can be reconstructed all the way down to zero momentum. The lowest-momentum π^0's decay almost back-to-back, with the photons depositing energy about equally in the calorimeter. As the π^0 momentum increases over the $D^{*0}\ell\nu$ range, the photon energies become less symmetric, which tends to push some of the lower-energy photons below our minimum energy requirement of 30 MeV. The neutral slow pion efficiency therefore drops slowly as w increases, as shown in Figure 5.1.

We have explored the slow pion efficiency as a function of many variables in the simulation of CLEO II. The slow pion efficiency depends on the exact placement and amount of the material in the simulation. The photons can interact with any of the material in the detector, which means that they start their showers before reaching the calorimeter. When the photons interact with material at radii smaller than the outer boundary of the DR ("inner material"), either none of the photon's energy travels out to the calorimeter, or not enough of the energy is deposited in the calorimeter to pass our energy cut or to make the proper $m_{\gamma\gamma}$. When the photons interact with material at or outside the outer boundary of the DR ("outer material"), the showers usually are reconstructed, but they may not pass our cuts on the shape (`E9/E25`). Some of the energy is also lost, which affects $m_{\gamma\gamma}$ and gives the $m_{\gamma\gamma}$ distribution an asymmetric tail on the low side. The amount of outer material affects the shape of the low-side tail and therefore the efficiency for reconstructed π^0's to pass our requirement on $m_{\gamma\gamma}$. The π^0 efficiency depends also on the amount of noise in the calorimeter. We simulate two categories of calorimeter noise: "incoherent" noise, which is applied crystal-by-crystal, and "coherent" noise, which is applied to groups of crystals with neighboring electronics connections. We have adjusted the incoherent noise in the simulation, but there is statistical uncertainty on amount that it should be increased that adds uncertainty to our efficiency correction. We have this statistical uncertainty because we adjust the noise based on comparisons of data and Monte Carlo distributions. Likewise, there is a statistical uncertainty on the amount of smearing that we add to the gain of the calorimeter electronics. Finally, the energy down to which our simulation follows photons is important because it can affect the shape of the showers in the calorimeter.

We determine our sensitivity to the uncertainty on the efficiency correction by repeating our embedding procedure using six separate samples of π^0's. Each sample is different from the baseline sample as follows:

- (1) We vary the incoherent noise by the statistical uncertainty on its adjustment;
- (2) We vary the crystal gain smearing by the statistical uncertainty on its adjustment;
- (3) We vary the coherent noise by 25% [43];
- (4) We vary the inner material by 10% based on a study of the material in the simulation comparing the polar angle distribution of data and simulated $\gamma\gamma$ events [44];
- (5) There is some certainty about the outer DR cathode material because the inner DR cathodes are probed in the study of inner material, but the rest of the outer material has not been studied, so we vary the outer material by 15%;
- (6) We lower the energy down to which our simulation follows photons to 0.1 MeV.

We calculate new efficiency corrections for each of the six variations and recompute the efficiency matrix. The efficiency correction in w bins for each variation is given in Table 5.8. We then repeat the $|V_{cb}|$ fit using these new efficiencies and take the changes in our results as the uncertainty. We take all of the uncertainties to be symmetric, including the uncertainty from the photons cutoff. While it is only reasonable to lower the photon cutoff, not raise it, in the end the difference between our total uncertainties up and down would be small, so we add it in quadrature with the rest of the uncertainties. We include in our total the statistical uncertainty on our studies and a small uncertainty based on the fact that we add two showers to events when we embed π^0's for our efficiency study. The slow pion efficiency may change differently for data and simulated events when we embed these extra showers in the events; we find no statistically significant evidence of this in our studies, but we include a small uncertainty (0.34% on $|V_{cb}|F(1)$) to cover this effect. Table 5.9 shows the changes to our results with the efficiency correction variations, the contribution to our uncertainty from the statistics of our study and "number of showers" effect, and the total uncertainty from the slow-π^0 efficiency, which comes to 3.11% on $|V_{cb}|F(1)$.

5.2.2 Lepton Identification Efficiency

The electron identification efficiency for Monte Carlo electrons is an input parameter to `driver`, the program that processes `ROAR` files. When the user examines `R2ELEC` for a Monte Carlo track, `driver` first looks to see if that track was created by an electron. If so, `driver` looks up the efficiency for electrons of that momentum. By tossing a random number, `driver` determines if that track will be identified as an electron or not.

Table 5.8: The $B \to D^{*0} \ell \nu$ efficiency correction as computed for the six variations to the simulation. The first column lists the w range for each bin. The second through seventh columns show the uncertainties in percent for the variations in incoherent noise (IN), crystal gains (CG), coherent noise (CN), inner material (IM), outer material (OM), and `CUTGAM` (GAM). The last column gives the statistical uncertainty for each variation.

w	IN	CG	CN	IM	OM	GAM	Uncertainty
1.05-1.10	0.9	-5.8	-3	-7.4	-4.1	-4.9	-2.2
1.10-1.15	-7.5	-3.2	-1.5	6.4	-4.5	-4.5	-2.6
1.15-1.20	-7.7	-6.7	-5.1	-4.9	0	-3.8	-1.3
1.20-1.25	-2.4	-3.8	-7.1	-1.8	-5.1	-5.3	4.6
1.25-1.30	0.7	5.7	3.9	7.3	5.5	2.4	3.9
1.30-1.35	-3.7	-1.6	2.3	-3.3	2.5	-4.8	8.8
1.35-1.40	-5.5	-7	-3.1	-3.3	0.5	-5.3	4.2
1.40-1.45	-4.9	-1.2	-11	1.6	3.3	4.2	5.4
1.45-1.51	-1.1	-6.5	0.2	-6.1	-5.6	-1.3	-0.8

Table 5.9: The changes to our results from the variations in the slow-π^0 efficiency correction and the uncertainties from the statistics of our slow-π^0 study and the number of showers. We add these together in quadrature to get the total uncertainty from the slow-π^0 reconstruction efficiency.

Mode	$\lvert V_{cb}\rvert F(1)$ (%)	ρ^2(%)	$\Gamma(B \to D^* \ell\nu)$(%)
Incoherent Noise up 1 σ	+0.81	-2.55	+3.95
Gain Smearing down 1 σ	+0.78	-1.02	+2.49
Coherent Noise up 25%	+0.52	-0.82	+1.78
Inner Material up 10%	-0.98	-2.68	+0.39
Outer Material up 15%	-0.41	-1.40	+0.42
γ Cutoff down	+1.54	+0.93	+2.25
Statistics of Study	2.13	3.31	2.73
Number of showers in events	0.34	0.00	0.68
Total Uncertainty	3.11	5.40	6.18

We determine the electron identification efficiency of the data by embedding data electrons in data events [45]. Events are selected from all data sets with the requirements that there be at least one lepton in the event, that $H_2/H_0 < 0.4$, and that the center-of-mass energy is greater than 5.28 GeV. Electron tracks are selected from data radiative Bhabha events. The track must meet our tracking criteria detailed in Section 4.3, and in addition the dot product between the isolated track and the embedded track must be greater than 0.996. Also, we require that the total energy near the track in the calorimeter (known as `PVERTX`) be less than 3 GeV. Embedded electrons are then found by requiring `R2ELEC`≥ 3.

There are several sources of uncertainty on the electron identification uncertainty. The efficiency is sensitive to the requirements made on the electron tracks including `PVERTX` (0.3%) and the dot product (0.2%). The electrons selected for embedding may be systematically different than $B \to D^* \ell \bar{\nu}$ electrons. We have studied this by comparing the `R2ELEC` distributions for electrons from Monte Carlo radiative Bhabha events to electrons generated in events with no other particles. We assign an error of 0.6% to this effect. Two different methods are compared for selecting the electron tracks from the radiative Bhabha events which result in slightly different samples; a 2.0% uncertainty is assigned to this difference. The radiative Bhabha events must meet a requirement on the energy and momentum visible in the event; the uncertainty from this requirement is 0.6%. The efficiency determined from isolated electrons matches that from embedded electrons to 1.0%. The efficiency distribution versus momentum showed variations between data sets; this difference adds a 1.0% uncertainty. Finally, an embedding study done with

Monte Carlo electrons and events shows that the embedding procedure determines the correct efficiency for $B \to D^* \ell \bar{\nu}$ electrons to 0.6%. We add these errors in quadrature to get an electron identification efficiency uncertainty of 2.6%.

Chaouki Boulahouache has determined the the efficiency for muons in radiative $\mu^+\mu^-$ events in data. Comparing this efficiency to the efficiency for muons in our $B \to D^* \ell \bar{\nu}$ Monte Carlo, and taking into account the momentum distribution of of $B \to D^* \ell \bar{\nu}$ muons, we find that the ratio of data to Monte Carlo efficiencies is 1.009±0.013. We take the 0.9/identification efficiency uncertainty of 1.6%.

We weight the electron and muon efficiency uncertainties by the relative abundance of each species in our $B \to D^* \ell \bar{\nu}$ yield to get an overall uncertainty of 2.2%.

5.2.3 Track-Finding Efficiency

We determine the tracking efficiency uncertainties for the lepton and the K and π forming the D^0 with an embedding study similar to the study of slow-π^0 efficiency, but performed with charged pions with momenta between 0.5 and 2.0 GeV/c [46]. We find an efficiency uncertainty of 0.7% each for the K and π and 0.5% for the lepton. We combine these uncertainties linearly to get a total efficiency uncertainty of 1.9%, which implies an uncertainty of 0.95% on $|V_{cb}|F(1)$. These uncertainties are confirmed in a study of 1-prong versus 3-prong τ decays [47].

5.3 Uncertainties from Constants

In this section we describe the uncertainty on our results from the uncertainty on the many constants we use is our $|V_{cb}|$ fit.

5.3.1 $R_1(1)$ and $R_2(1)$

The form factor ratios $R_1(1)$ and $R_2(1)$ affect the lepton spectrum and therefore the fraction of events satisfying our 0.8 GeV/c electron and 1.4 GeV/c muon momentum requirements. To estimate the uncertainty due to the measurement uncertainties on $R_1(1)$ and $R_2(1)$, we begin by repeating our analysis while varying the values of $R_1(1)$ and $R_2(1)$ by their measurement uncertainties of 0.32 and 0.23, respectively. We vary $R_1(1)$ up and down by one sigma and keep $R_2(1)$ fixed, and then we keep $R_1(1)$ fixed and vary $R_2(1)$ up and down by one sigma. From these results we calculate $\partial P/\partial R_1(1)$ and $\partial P/\partial R_2(1)$, where P stands for the parameter ($|V_{cb}|F(1)$, $\rho^2_{A_1}$, or $\Gamma(B \to D^*\ell\nu)$) whose uncertainty we are calculating. We calculate the uncertainty as

$$\sigma_P^2 = \sum_{i,j=1}^{2} \frac{\partial P}{\partial R_i(1)} \frac{\partial P}{\partial R_j(1)} E_{ij} \tag{5.1}$$

where $E_{ii} = \sigma_i^2$ and $E_{ij} = \rho_{ij}\sigma_i\sigma_j$ (where $\rho_{12} = -0.82$ is the correlation coefficient from the $R_1(1)$ and $R_2(1)$ measurement). The uncertainties from this source are given in Table 5.10; we assign an uncertainty of 1.07% to $|V_{cb}|F(1)$ from this source.

Table 5.10: The variation in the results with $R_1(1)$ and $R_2(1)$. The total uncertainty reported for each fit takes into account the correlation between $R_1(1)$ and $R_2(1)$ in the original measurement.

Variation	$\lvert V_{cb}\rvert F(1)$ (%)	$\rho^2(\%)$	$\Gamma(B \to D^*\ell\nu)(\%)$
$R_1(1)$ down	+1.86	-1.64	+2.95
$R_1(1)$ up	-1.78	+1.83	-2.32
$R_2(1)$ down	+1.17	+11.87	+1.22
$R_2(1)$ up	-1.31	-13.73	-1.19
Uncertainty	1.07	14.26	1.78

5.3.2 B Momentum and Mass

The $\cos\theta_{B-D^*\ell}$ distribution depends on the B momentum and mass that we use to construct this variable. We know the exact value of the momentum and mass in our Monte Carlo, but there is measurement uncertainty on the data values. To determine the uncertainty from this source, we vary the B momentum and mass separately by their measurement uncertainties and take the change in our results as our uncertainty. We find an uncertainty of 0.55% on $|V_{cb}|F(1)$ from this source. The changes and uncertainty are given in Table 5.11.

5.3.3 Number of $B\overline{B}$ Events

The uncertainty of the number of $B\overline{B}$ events in our data sample has been determined as 1.8% [48], which leads to an uncertainty of 0.9% on $|V_{cb}|F(1)$.

Table 5.11: The changes in our results when we vary the B momentum and mass. We add the results in quadrature to get the uncertainty.

Variation	$\|V_{cb}\|F(1)$ (%)	ρ^2(%)	$\Gamma(B \to D^*\ell\nu)$(%)
B momentum down 1 σ	+0.53	+0.44	+0.66
B mass down 1 σ	+0.16	-0.10	+0.40
Total Uncertainty	0.55	0.45	0.77

5.3.4 Branching Fractions and Lifetimes

The fractional uncertainties on the $D^{*0} \to D^0\pi^0$ branching fraction (4.7%) and the $D^0 \to K^-\pi^+$ branching fraction (2.3%) contribute the same fractional uncertainty to $\Gamma(B \to D^*\ell\nu)$, half of that to $|V_{cb}|F(1)$ because of the square root, and none to $\rho^2_{A_1}$, which is not affected by changes to the overall normalization of $d\Gamma/dw$.

The uncertainty to the B lifetimes enters in more obliquely because of our constraint on f_{+-}. To determine the uncertainty from the lifetimes, we vary the lifetimes by their uncertainty and repeat the $|V_{cb}|$ fit. This gives us an uncertainty of 0.82% on $|V_{cb}|F(1)$. The changes and uncertainty are given in Table 5.12.

5.4 Other Uncertainties

5.4.1 Final-State Radiation

The final-state radiation model has a small effect on our $D^*\ell\nu$ yields because it affects the $D^{*0}\ell\nu$ $\cos\theta_{B-D^*\ell}$ distributions. Because we require the emitted photon

Table 5.12: The changes in our results from modification of the B lifetimes and the uncertainty we assign from this source.

Variation	$\lvert V_{cb}\rvert F(1)$ (%)	ρ^2(%)	$\Gamma(B \to D^*\ell\nu)$(%)
B^+ lifetime up 1 σ	-0.54	0.00	-0.85
B^0 lifetime up 1 σ	-0.62	0.00	-1.00
Total Uncertainty	0.82	0.00	1.31

Table 5.13: The change in our results when we do not include radiative $D^{*0}\ell\nu$ events in our $D^{*0}\ell\nu$ Monte Carlo and the uncertainty that we assign due to the final-state radiation model.

	$\lvert V_{cb}\rvert F(1)$ (%)	ρ^2(%)	$\Gamma(B \to D^*\ell\nu)$(%)
Change	-0.53	-0.74	-0.41
Uncertainty	0.16	0.22	0.12

to have energy less than 100 MeV, the model also affects the $D^{*0}\ell\nu$ efficiency. The final-state radiation model is estimated by the authors of PHOTOS to be good to 30%. We determine our sensitivity to the model by repeating our analysis without including radiative $D^{*0}\ell\nu$ decays in our $D^{*0}\ell\nu$ Monte Carlo. We then take 30% of the change to our results as our uncertainty. This leads to a 0.16% uncertainty on $|V_{cb}|F(1)$. The changes and uncertainties are given in Table 5.13.

5.4.2 $D^*X\ell\nu$ Model

With the exception of the $B \to D_1\ell^-\bar{\nu}$ mode, which has been measured by CLEO and ALEPH [49], the modes that contribute to the $D^*X\ell\nu$ background have not been exclusively reconstructed. For this reason, we have little direct knowledge of the $D^*X\ell\nu$ form factors or branching fractions. Since we allow the $D^*X\ell\nu$ contribution to float in our $\cos\theta_{B-D^*\ell}$ fits, the poor knowledge of the inclusive $D^*X\ell\nu$ branching fraction does not effect us; however, the $\cos\theta_{B-D^*\ell}$ distributions that we use in our fits are affected by the model uncertainties of the ISGW2 model [31].

With little or no data to compare to predictions, it is difficult to know what is a reasonable variation of the ISGW2 model. Instead, we assume that the changes to the $\cos\theta_{B-D^*\ell}$ distribution from the model uncertainty is smaller than the difference in the $\cos\theta_{B-D^*\ell}$ distribution of the different modes. We find that the two modes with the combination of the largest contribution to the $\cos\theta_{B-D^*\ell}$ distribution and the most different $\cos\theta_{B-D^*\ell}$ distributions are $B \to D^{*0}\pi\ell\bar{\nu}_\ell$ and $B \to D_1^{*0}\,\ell\bar{\nu}_\ell$. The $\cos\theta_{B-D^*\ell}$ distribution of these modes are shown in Figure 5.2. To assess our uncertainty from the $D^*X\ell\nu$ model, we repeat our analysis, replacing the $D^*X\ell\nu$ $\cos\theta_{B-D^*\ell}$ distribution in the fits with the $\cos\theta_{B-D^*\ell}$ distribution of $B \to D^{*0}\pi\ell\bar{\nu}_\ell$ or $B \to D_1^{*0}\,\ell\bar{\nu}_\ell$. We take the larger excursion as our systematic uncertainty. We assign an uncertainty of 1.15% on $|V_{cb}|F(1)$ from the $D^*X\ell\nu$ model. The effect of the separate modes on our results and the systematic uncertainties are given in Table 5.14.

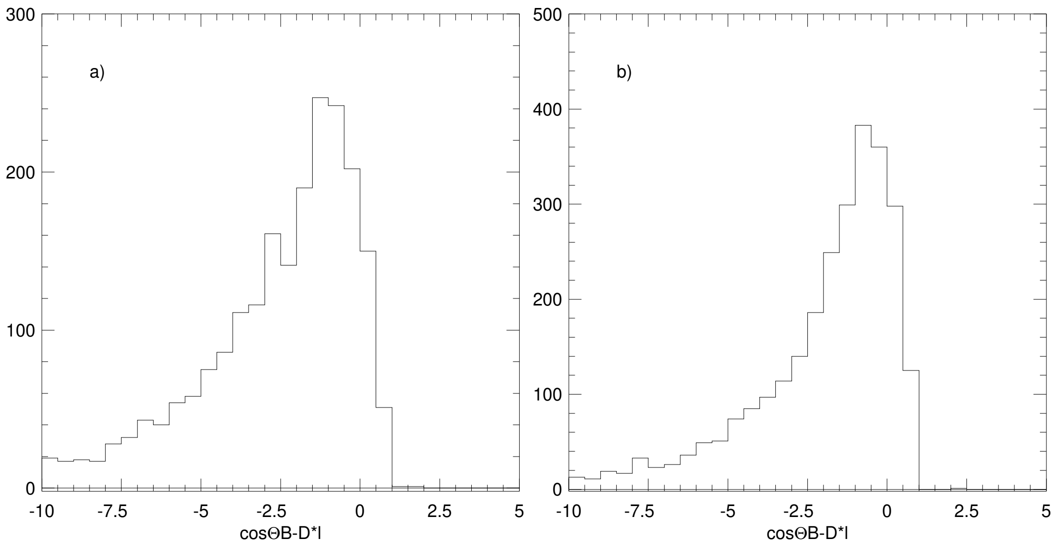

Figure 5.2: The $\cos\theta_{B-D^*\ell}$ distribution of (a) the $B \to D^{*0}\pi\ell\nu$ and (b) the $B \to D_1\ell\nu$ events contributing to the $D^*X\ell\nu$ sample for $D^{*0}\ell\nu$.

Table 5.14: The variation in the results with the $D^*X\ell\nu$ model and the uncertainties we assign.

Mode	$\|V_{cb}\|F(1)$ (%)	ρ^2(%)	$\Gamma(B \to D^*\ell\nu)$(%)
$B \to D^*\pi\ell\nu$	+1.15	+2.69	-0.02
$B \to D_1\ell\nu$	-0.03	-0.67	+0.52
Uncertainty	1.15	2.69	0.52

5.5 Total Uncertainty

All of the sources of uncertainty are listed in Table 5.15. We find the total uncertainty by adding the separate uncertainties in quadrature. We find a total systematic uncertainty of 5.4% on $|V_{cb}|F(1)$, 16.3% on $\rho^2_{h_{A_1}}$, and 9.4% on the decay width $\Gamma(B \to D^* \ell \nu)$.

Table 5.15: The fractional systematic uncertainties for the $D^{*0}\ell\nu$ results.

Source	$\|V_{cb}\|F(1)(\%)$	$\rho^2(\%)$	$\Gamma(B \to D^*\ell\nu)(\%)$
Continuum background	0.2	0.3	0.0
Combinatoric background	2.2	4.9	2.0
Uncorrelated background	0.8	1.2	0.5
Correlated background	0.1	0.4	0.6
Fake Lepton background	0.0	0.0	0.1
Slow-π^0 Efficiency	3.1	5.4	6.1
Lepton identification	1.1	0.0	2.2
K, π & ℓ finding	1.0	0.0	1.9
$R_1(1)$ and $R_2(1)$	1.1	14.3	1.8
B Momentum and Mass	0.6	0.5	0.8
Number of $B\bar{B}$ events	0.9	0.0	1.8
$\mathcal{B}(D^{*0} \to D^0\pi^0)$	2.4	0.0	4.7
$\mathcal{B}(D^0 \to K^-\pi^+)$	1.2	0.0	2.3
B lifetimes	0.8	0.0	1.3
Final State Radiation Model	0.2	0.2	0.1
$D^*X\ell\nu$ model	1.2	2.7	0.5
Total	5.4	16.3	9.4

CHAPTER 6

CONCLUSION

6.1 Final Results

We have measured $|V_{cb}|F(1)$ and $\rho^2_{h_{A_1}}$ from the width Γ from $D^{*0}\ell\nu$ decays. Our final results are

$$
\begin{aligned}
|V_{cb}|\mathcal{F}(1) &= 0.0427 \pm 0.0026 \pm 0.0023 && (6.1)\\
\rho^2_{h_{A_1}} &= 1.54 \pm 0.18 \pm 0.25 && (6.2)\\
\chi^2 &= 8.8/8\,\mathrm{dof}, && (6.3)
\end{aligned}
$$

where the first errors are statistical and and the second errors are systematic. The results These results imply the following:

$$
\begin{aligned}
\Gamma(B \to B \to D^*\ell\bar{\nu}) &= 0.0400 \pm 0.0027 \pm 0.0037 && (6.4)\\
\mathcal{B}(D^{*0}\ell\nu) &= 6.62 \pm 0.45 \pm 0.61, && (6.5)
\end{aligned}
$$

where again the errors are statistical and systematic. Using $\mathcal{F}(1) = 0.913 \pm 0.042$ [6], we find

$$
|V_{cb}| = 0.0468 \pm 0.0027 \pm 0.0025 \pm 0.0022, \qquad (6.6)
$$

where the first error is statistical, the second error is systematic, and the third error reflects the error on $\mathcal{F}(1)$. The total error on $|V_{cb}|$ is 9.2%.

6.2 Combined Fit with $D^{*+}\ell\nu$

An analysis of $D^{*+}\ell\nu$ decays has been done in parallel with this analysis [50]. That analysis uses the method described in Chapter 4 to extract $D^{*+}\ell\nu$ yields in bins of w. We do a combined fit for $|V_{cb}|F(1)$ and $\rho^2_{A_1}$ using the method described in Section 4.5, where the χ^2 that we minimize is the sum of the χ^2 term in Equation 4.8, a similar term related to the $D^{*+}\ell\nu$ yields, and a term constraining f_{+-}. In the fit we assume a common decay width $\Gamma(B \to B \to D^*\ell\bar{\nu})$ and a common $\mathcal{F}(w)$; we also assume $f_{+-} + f_{00} = 1$. From this combined fit, we find:

$$
\begin{aligned}
|V_{cb}|\mathcal{F}(1) &= 0.0422 \pm 0.0013 \pm 0.0018 && (6.7)\\
\rho^2_{h_{A_1}} &= 1.61 \pm 0.09 \pm 0.21 && (6.8)\\
\chi^2 &= 16.5/18\,\mathrm{dof}, && (6.9)
\end{aligned}
$$

where the first errors are statistical and and the second errors are systematic. These results imply the following:

$$
\begin{aligned}
\Gamma(B \to B \to D^*\ell\bar{\nu}) &= 0.0376 \pm 0.0012 \pm 0.0024 && (6.10)\\
\mathcal{B}(D^{*0}\ell\nu) &= 6.21 \pm 0.20 \pm 0.40, && (6.11)\\
\mathcal{B}(D^{*+}\ell\nu) &= 5.82 \pm 0.19 \pm 0.37, && (6.12)
\end{aligned}
$$

where again the errors are statistical and systematic. The errors for the branching fractions are completely correlated. From the combined results for $|V_{cb}|F(1)$ we find

$$|V_{cb}| \quad = \quad 0.0462 \pm 0.0014 \pm 0.0020 \pm 0.0022, \tag{6.13}$$

where the first error is statistical, the second error is systematic, and the third error reflects the error on $\mathcal{F}(1)$. The total error on $|V_{cb}|$ from the combined fit is 7.1%.

6.3 Comparison to Previous CLEO Measurement

The previous CLEO measurement [42] of $|V_{cb}|F(1)$ from $B \to D^*\ell\bar{\nu}$ was made using both $D^{*0}\ell\nu$ decays and $D^{*+}\ell\nu$ decays and a linear form of $\mathcal{F}(w)$. The constraints from dispersion relations allow a curvature, which tends to increase $|V_{cb}|F(1)$ by about 2.6% [51]. Making this correction, the result for $|V_{cb}|F(1)$ from the previous analysis is

$$|V_{cb}|\mathcal{F}(1) \quad = \quad 0.0360 \pm 0.0019 \pm 0.0018, \tag{6.14}$$

where the errors are statistical and systematic. The previous analysis also measured $\mathcal{B}(D^{*0}\ell\nu)$ from only $D^{*0}\ell\nu$ decays; modifying the previous result to use our values for $\mathcal{B}(D^{*0} \to D^0\pi^0)$ and $\mathcal{B}(D^0 \to K^-\pi^+)$ and the value of f_{+-} from our fit, we get

$$\mathcal{B}(B \to D^{*0}\ell\nu) \quad = \quad 5.45 \pm 0.57 \pm 0.68, \tag{6.15}$$

where the errors are statistical and systematic.

Both of the results from the previous measurement are somewhat lower than our results. Our data sample includes the data sample of the previous analysis and increases the number of $B\overline{B}$ events by roughly a factor of two. We have found that the new data favor larger values of $|V_{cb}|F(1)$ and the branching fraction, and also that results from the old data and the new data are consistent within uncorrelated systematic uncertainties. This work decreases the systematic uncertainty on the branching fraction by 26%, and our combined result on $|V_{cb}|F(1)$ decreases the systematic uncertainty by 24%.

6.4 Comparison to Other Measurements

6.4.1 $|V_{cb}|F(1)$ from Exclusive $B \to D^*\ell\bar{\nu}$

We compare our $D^{*0}\ell\nu$ and combined results to measurements of $|V_{cb}|F(1)$ from exclusive $B \to D^*\ell\bar{\nu}$ decays made at LEP [52] (an electron-positron collider in Switzerland) in Table 6.1. These results are plotted in Figure 6.1. The LEP results include results from the ALEPH, DELPHI, and OPAL experiments. The $|V_{cb}|$ Working Group at LEP has adjusted the separate measurements so that each measurement has the same input parameters. All of the LEP analyses use the same form factor constraints used in this analysis [10].

LEP generates B particles from e^+e^- collisions, but they run at a much higher center-of-mass energy than CESR. As a result, the B's detected in the various experiments have significant momentum, with an average value around 30 GeV/c. The advantage of this setup is that $B \to D^{*+}\ell\nu$ decays can easily be detected at low w because the boost of the B momentum raises the momentum of the π^+ from the decay of the D^{*+}. There are, however, several disadvantages. The high B

Table 6.1: Comparison of $|V_{cb}|F(1)$ and $\rho^2_{A_1}$ results. The "inclusive" and "exclusive" notation on the OPAL results refers to the D^0 decay.

Measurement	$\lvert V_{cb}\rvert F(1)$	$\rho^2_{A_1}$
This work	0.0427 ± 0.0035	1.54 ± 0.31
This work combined with $D^{*+}\ell\nu$	0.0422 ± 0.0022	1.61 ± 0.23
ALEPH	0.0330 ± 0.0026	0.74 ± 0.5
DELPHI	0.0345 ± 0.0029	1.22 ± 0.4
OPAL (exclusive)	0.0375 ± 0.0025	1.42 ± 0.3
OPAL (inclusive)	0.0379 ± 0.0027	1.21 ± 0.4

momentum leads to a much poorer resolution in w. The boost also makes it difficult to distinguish $D^*X\ell\nu$ decays from $D^*\ell\nu$ decays and increases the background from other B decays including $B \to D^*\tau\bar{\nu}$.

Our result is higher than all of the LEP results, but is fairly consistent with all of them. The main difference in method between our analysis and the LEP analyses lies in the treatment of the $D^*X\ell\nu$ background. The LEP analyses absolutely normalize the $D^*X\ell\nu$ contribution using a model [53] constrained by measured rates. The comparison suggests that this model may overestimate the contribution to the $D^*\ell\nu$ yield from $D^*X\ell\nu$ decays, or that it may have the wrong distribution in w. Since we allow the data to set the level of $D^*X\ell\nu$ decays in bins of w, we are not as sensitive to these model uncertainties.

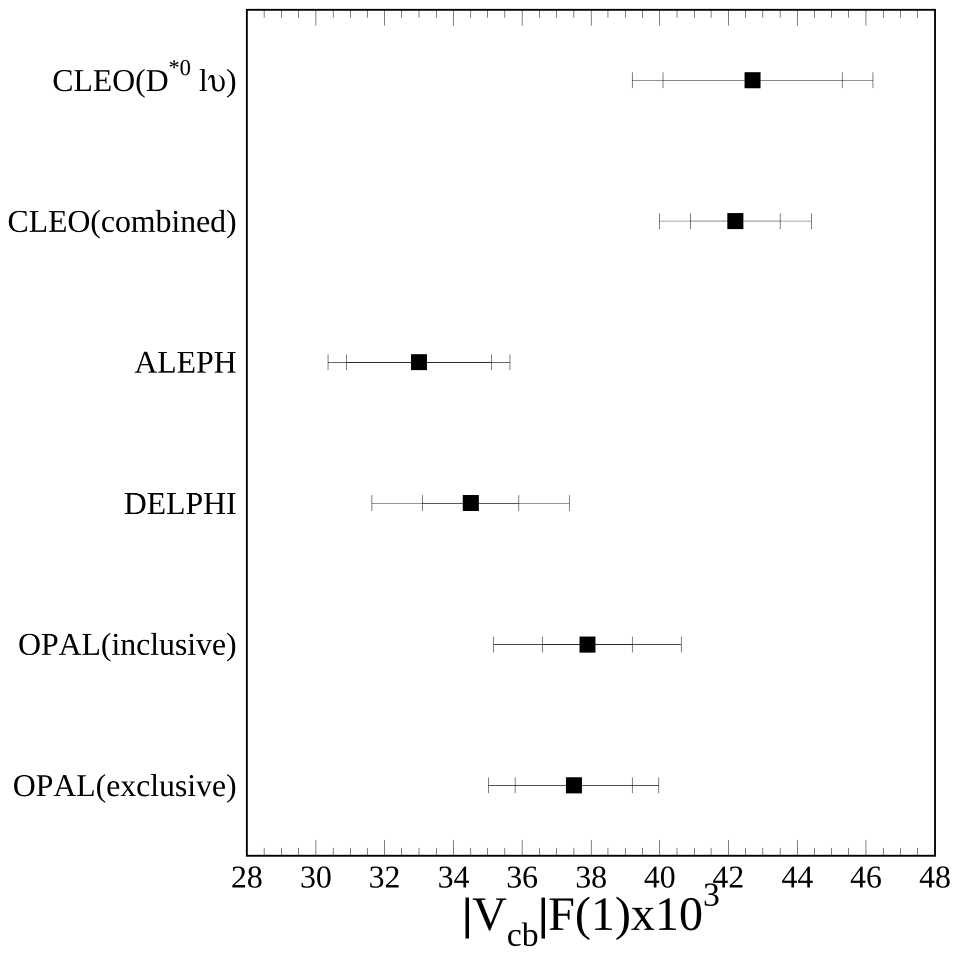

Figure 6.1: Measurements of $|V_{cb}|F(1)$ from exclusive $B \to D^* \ell \bar{\nu}$ decays, from Table 6.1. The inner error bars show the statistical error, and the outer error bars show the total error.

6.4.2 $|V_{cb}|$ from $B \to D\ell\bar{\nu}$ and Inclusive Measurements

Table 6.2 gives our combined measurement for $|V_{cb}|$ along with measurements of $|V_{cb}|$ from other kinds of analyses. Three of these results are from single analyses of the CLEO II dataset, and the fourth ($b \to c\ell\nu$) uses a data sample of comparable size. The $\Gamma(B \to X_c\ell\nu)$ analysis determines $|V_{cb}|$ from the inclusive partial width of semileptonic B decays. The $\Gamma(b \to c\ell\nu)$ comes from several LEP analyses which have determined the inclusive partial width of semileptonic decays of particles containing a b quark; at LEP these can include B ($u\bar{b}$), B_s ($s\bar{b}$), and baryons. The results are plotted in Figure 6.2.

There are several things worth noticing in Figure 6.2. First, with these data samples the results are all consistent, and $B \to D\ell\bar{\nu}$ clearly leads to the most imprecise measurement. Also, the error on the results from the inclusive methods are almost saturated by theoretical errors, and there is an additional unknown theoretical uncertainty from the assumption of quark-hadron duality that could be comparable to the error already reported. The total error on the $b \to c\ell\nu$ measurement is smaller than the total error on the $B \to D^*\ell\bar{\nu}$ measurement (without the duality error, if any), but the $b \to c\ell\nu$ measurement will not benefit from smaller experimental errors. From that it is clear that $B \to D^*\ell\bar{\nu}$ currently offers the best way to measure $|V_{cb}|$ if the experimental errors can be reduced.

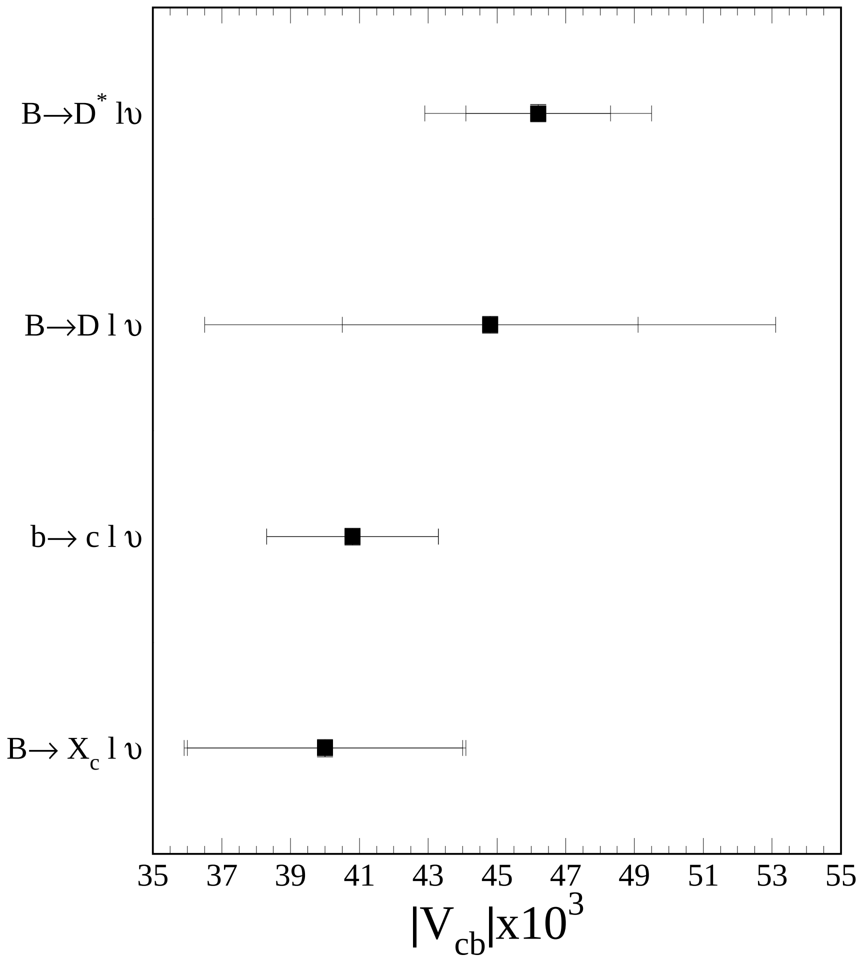

Figure 6.2: Measurements of $|V_{cb}|$ from exclusive and inclusive decays, Table 6.2. The inner error bars show the statistical error, and the outer error bars show the total error. The $b \to c\ell\nu$ measurement uses a slightly larger data sample than the rest.

Table 6.2: Comparison of our combined result to $|V_{cb}|$ determined from $B \to D\ell\bar{\nu}$ and inclusive semileptonic B decays.

This work combined with $D^{*+}\ell\nu$	0.0462±0.0033
CLEO $B \to D\ell\bar{\nu}$ [54]	0.0416±0.0072
$\Gamma(b \to c\ell\nu)$ [1]	0.0408±0.0025
$\Gamma(B \to X_c\ell\nu)$ [1]	0.0400±0.0026

6.4.3 $B \to D^{*0}\ell\nu$ Branching Fraction

The $B \to D^{*0}\ell\nu$ branching fraction has been measured by ARGUS [55]. They find

$$\mathcal{B}(B \to D^{*0}\ell\nu) = 6.6 \pm 1.6 \pm 1.5, \tag{6.16}$$

where the uncertainties are statistical and systematic. Our central value agrees well with theirs.

6.5 Future Measurements

In this work we have reported on the most precise measurement of the $B \to D^{*0}\ell\nu$ branching fraction. When we combine this analysis with a similar analysis of $B \to D^{*+}\ell\nu$ decays, we find the most precise measurement of $|V_{cb}|F(1)$. We extract a value of $|V_{cb}|$ where the largest error comes the theoretical uncertainty on the value of $\mathcal{F}(1)$.

Several experiments, including CLEO, are in the process of collecting larger samples of B decays. The BaBar experiment at the Stanford Linear Accelerator

Center hopes to collect at least $30\,\mathrm{fb}^{-1}$ of $\Upsilon(4S)$ decays, a data sample which would be about 10 times the size of the sample used in this measurement. This data sample would decrease the size of the statistical error on $|V_{cb}|$ by more than a factor of two, but determinations of $|V_{cb}|$ from exclusive $B \to D^* \ell \bar{\nu}$ decays are already limited by the systematic and theoretical uncertainties. In the case of this analysis, a larger data sample would do little to decrease the systematic error. Reducing the systematic error on $|V_{cb}|$ from its present level will therefore require a great deal more work, as will improvement of the theoretical uncertainties. The improvement is statistical error from the larger data samples of CLEO and the "B factories" will most likely be the next step in a more precise determination of $|V_{cb}|$.

APPENDIX A

A REVIEW OF THE STANDARD MODEL

The "Standard Model" [56] is the name physicists have given to a description of matter and all interactions between that matter. According to the Standard Model, all matter is made up of quarks and leptons, which are assumed to be elementary particles. While leptons can be observed individually, quarks are confined to bound states of two or three quarks, called hadrons. This makes it difficult to determine the masses of the quarks, since the masses can only be determined indirectly through their influence on the properties of the hadrons. The value attributed to the quark masses depend on how those masses are defined. The quark masses given here are ranges that depend on the particular schemes used to extract them. The quarks are listed in Table A.1 and the leptons in Table A.2 with their masses and electric charges. The quarks and leptons are divided into three "generations," with the d, u, e, and ν_e in the first generation, the s, c, μ, and ν_μ in the second generation, and the b, t, τ, and ν_τ in the third generation.

Each particle has an antiparticle with opposite charge but the same mass, represented by a "bar" over the quark symbol, as in $\bar{b}$. All quarks and leptons have a spin of $\frac{1}{2}$ and positive parity. Quarks are found in either a bound state of two quarks (one quark and one antiquark), known as a meson, or three quarks (any

Table A.1: The mass and charge of the six quarks in the Standard Model [1].

Name	Mass Range	Charge
d (down)	3-9 MeV/c^2	$-\frac{1}{3}e$
u (up)	1-5 MeV/c^2	$+\frac{2}{3}e$
s (strange)	75-170 MeV/c^2	$-\frac{1}{3}e$
c (charm)	1.15-1.35 GeV/c^2	$+\frac{2}{3}e$
b (bottom)	4.0-4.4 GeV/c^2	$-\frac{1}{3}e$
t (top)	165-180 GeV/c^2	$+\frac{2}{3}e$

combination of quarks and antiquarks), known as a baryon; mesons and baryons are known collectively as hadrons. The mesons important to this analysis are:

- B^-, made of a $\bar{u}$ and b quark;
- D^0, D^{*0}, made of a c and $\bar{u}$ quark, where the D^0 is the $J = 0$ state and the D^{*0} is the $J = 1$ state;
- K^-, made of a $\bar{u}$ and s quark;
- π^+, made of a u and $\bar{d}$ quark;
- π^0, which is a linear combination of the $u\bar{u}$ and $d\bar{d}$ states.

The charge conjugate particles (B^+, $\bar{D}^0$, etc.) have the same quark content with each quark (antiquark) replaced by its antiquark (quark).

Four forces describe all of the interactions between matter. The forces are:

Table A.2: The mass and charge of the six leptons in the Standard Model [1].

Name	Mass	Charge
e^- (electron)	0.511 MeV/c^2	-1
ν_e (electron neutrino)	< 3 eV/c^2	0
μ^- (muon)	106 MeV/c^2	-1
ν_μ (muon neutrino)	< 0.19 MeV/c^2	0
τ^- (tau)	1.78 GeV/c^2	-1
τ_μ (tau neutrino)	< 18 MeV/c^2	0

- Electromagnetic, which describes interactions between photons (the mediator of this force) and particles with non-zero electromagnetic charge;
- Weak, which describes quark-lepton interactions and is mediated by the W and Z particles;
- Strong, which describes quark-quark interactions and is mediated by gluons;
- Gravitational, which is mediated by gravitons.

The properties of the mediator particles are summarized in Table A.3. The order of relative strength of the forces, from strongest to weakest, is strong, electromagnetic, weak, gravitational. The strong and weak forces work only over very short distances (10^-15 m or less), while the range of the electromagnetic and gravitational forces appears to be infinite. At high enough energies, the electromagnetic and weak forces appear to have the same strength, unifying into one "electroweak"

Table A.3: The properties of the mediators of the four fundamental forces.

Mediator	Charge	J^P	Mass	Range
gluon (g)	0	1^-	0	10^{-15} m
photon (γ)	0	1^-	0	∞
$W^\pm$, Z^0	$\pm e$, 0	1	80, 91 GeV/c^2	10^{-18}
graviton (G)	0	2^+	0	∞

force, and there is reason to believe all of the forces are caused by a single interaction that breaks down to four at the current energy level of the universe. This is the motivating factor behind the search for so-called "Grand Unification Theories," but there is plenty of progress left to be made in the understanding of the individual forces.

APPENDIX B

SLOW π^0 EFFICIENCY STUDY

B.1 Introduction

We are motivated to study π^0 efficiency by a need to determine the reconstruction efficiency for $D^{*0}\ell\nu$ events, which we use to measure $|V_{cb}|$. We reconstruct D^{*0}'s through the decays $D^{*0} \to D^0\pi^0$, $D^0 \to K^-\pi^+$, and $\pi^0 \to \gamma\gamma$. The photons are detected as showers in the calorimeter, and π^0 candidates are formed from pairs of photon showers. The biggest contribution to the uncertainty on the $D^{*0}\ell\nu$ efficiency comes from the π^0 reconstruction. In the previous CLEO measurement of $|V_{cb}|$ from $D^{*0}\ell\nu$ events [42], the uncertainty assigned to slow π^0 efficiency was 8.6%; not only have we made a considerable improvement on this measurement, we have also found a way to improve the agreement of slow-π^0 Monte Carlo `E9/E25`, $m_{\gamma\gamma}$, and Δm ($\Delta m \equiv m_{K\pi\pi^0} - m_{K\pi}$) distributions with data.

The π^0's generated in $D^{*0}\ell\nu$ decays have momenta between 0 and 250 MeV/c, a range which is termed "slow" in CLEO lingo. The showers tend to have low energy, staying between 30 MeV (our lower cutoff) and 230 MeV. Because of the low momentum, the showers also stay well-separated in the calorimeter.

For this study, we use Recompress data and Monte Carlo, excluding the run regions in the 4s9 and 4sA datasets with calibration errors in the CC constants [57]. We use `CCFC` to reconstruct the photons from the π^0 decay, and we get π^0 candidates from `anlcp0.inc`.

Our goal is to find the difference between the efficiency for reconstructing π^0's in data and Monte Carlo, and the uncertainty on this difference. We find that the `E9/E25`, $m_{\gamma\gamma}$, and Δm distributions are not reproduced well in the Monte Carlo for slow π^0's. By correcting an error in the Time of Flight material and adjusting two Monte Carlo parameters, we find that we can largely correct these discrepancies. To study the π^0 efficiency, we first generate single π^0's using a modified Monte Carlo in which these problems have been corrected and embed these π^0's in data events. We also generate single π^0's using the default Monte Carlo which we embed in Monte Carlo events. We then find the π^0 efficiency difference for the two samples, which equals the efficiency difference between data and Monte Carlo. We vary six Monte Carlo parameters that affect π^0 efficiency to determine the uncertainty on the efficiency difference.

B.2 Comparing data and Monte Carlo π^0's

In our $D^{*0}\ell\nu$ analysis, we make the following requirements on π^0 candidates:

- $E_\gamma \geq 30\,\text{MeV}$
- $|cos\theta_\gamma| \leq 0.7071$

- no type 1 or type 2 match of shower to track
- no "bad" showers
- E9/E25 $\geq$ 99% efficient cut from `cce925`
- $0.120\,\mathrm{GeV}/c^2 \leq m_{\gamma\gamma} \leq 0.150\,\mathrm{GeV}/c^2$
- $0.1392\,\mathrm{GeV}/c^2 \leq \Delta m \leq 0.1452\,\mathrm{GeV}/c^2$

All of these cuts affect the π^0 efficiency, but the efficiency is more sensitive to some than others. The Monte Carlo is tuned to reconstruct both shower energy and direction correctly on average, but there could be small differences in efficiency in data and Monte Carlo if the event environment affects the shape of the reconstructed shower energy or direction differently. This effect, if there is one, is included in our study through embedding, which is described in Section B.4.3. To first order, we believe that the track-shower matching in Monte Carlo matches that in the data; any difference will have little effect on the π^0 efficiency, since our candidates are 98% efficient for passing that cut. The "bad" showers designation is exactly reproduced since it comes from a list of "bad" crystals. We will show, however, that the shapes of `E9/E25`, $m_{\gamma\gamma}$, and Δm are significantly different in data and Monte Carlo for slow π^0's due to low-level Monte Carlo parameters and event environment effects. Understanding how the distributions of `E9/E25`, $m_{\gamma\gamma}$, and Δm differ between data and Monte Carlo can give us a handle on how well the Monte Carlo simulates data π^0's.

B.2.1 E9/E25 and $m_{\gamma\gamma}$ for inclusive π^0's

We look at inclusive π^0's to get an idea how the distributions of E9/E25 and $m_{\gamma\gamma}$ compare between data and Monte Carlo. We are only interested in π^0's in events that are similar to $D^{*0}\ell\nu$ events, so we make the following requirements on both data and generic Monte Carlo events:

- KLASGL $= 10$
- R2GL≤ 0.4
- require an electron or muon with:
  - $0.8\,\mathrm{GeV}/c \leq p_{lepton} \leq 2.4\,\mathrm{GeV}/c$
  - $|\cos\theta_{lepton}| < 0.7071$
  - R2ELEC > 3 for electron
  - DPTHMU > 5 and MUQUAL $= 0$ for muon.

Additionally, we include only π^0's that pass our analysis cuts and have momentum less than $250\,\mathrm{MeV}/c$ in our study. We make no Δm cut since we are not forming D^{*0}'s.

We first compare E9/E25 for showers that make up slow π^0 candidates. We divide the showers into energy bins of 30 MeV, beginning with 30-60 MeV and going up to 210 MeV. We were unable to develop a way to subtract background events from the data E9/E25 distributions, so these plots include both real photon showers that make fake π^0's and fake photon showers. Using tagging for these showers in

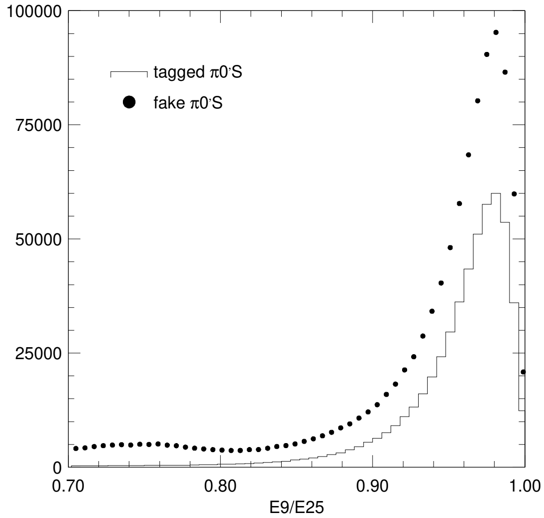

Figure B.1: The `E9/E25` distribution for tagged π^0's and tagged background from generic Monte Carlo. We include all showers from π^0's with momenta up to $250\,\mathrm{MeV}/c$ and with $0.1325\,\mathrm{GeV}/c^2 \leq m_{\gamma\gamma} \leq 0.1375\,\mathrm{GeV}/c^2$. The plots are absolutely normalized.

generic Monte Carlo, we determined that the fake π^0 background peaks in `E9/E25` in nearly the same way as showers from real π^0's (see Figure B.1). To minimize fake-π^0 background, we tighten the $m_{\gamma\gamma}$ cut to $0.1325\,\mathrm{GeV}/c^2 \leq m_{\gamma\gamma} \leq 0.1375\,\mathrm{GeV}/c^2$. We show the `E9/E25` distributions for data and generic Monte Carlo in the first four energy bins in Figure B.2. While the tails match surprisingly well, there is a clear difference in the shape of the main body of the distribution. We will quantify this difference in Section B.4.2; for now, we note that the shapes are significantly different in the region where we apply our `E9/E25` cut.

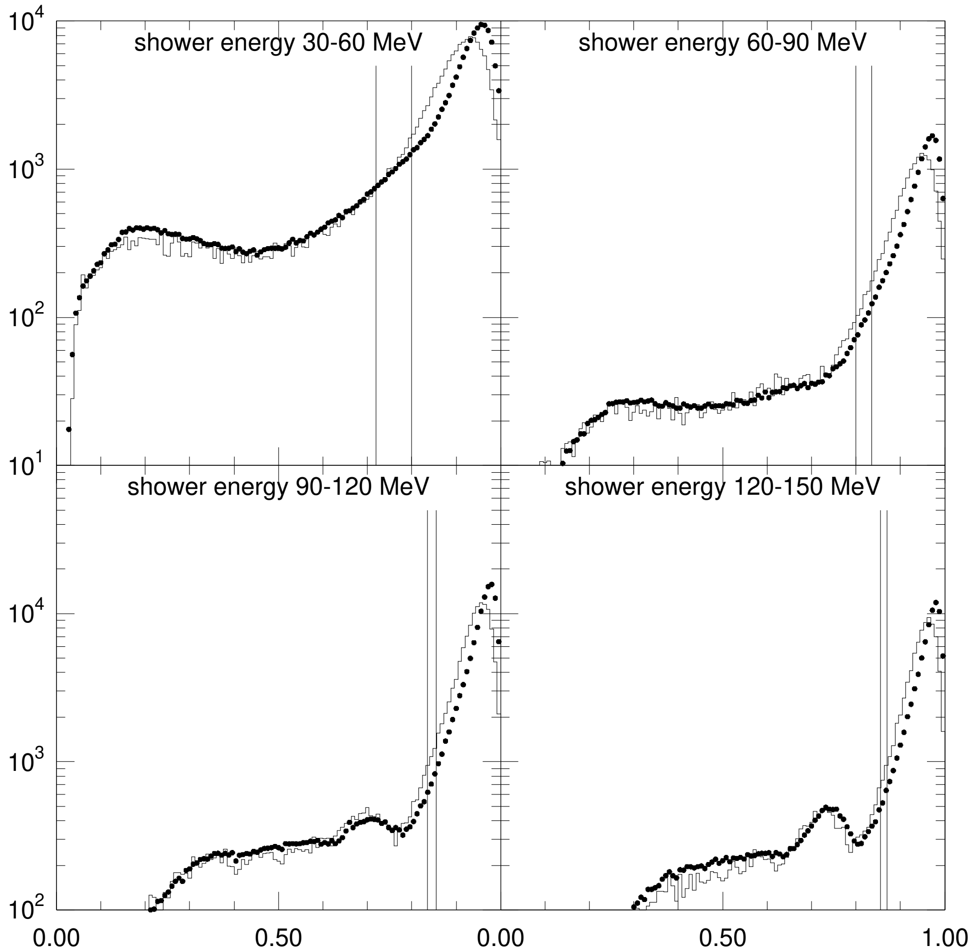

Figure B.2: The E9/E25 distributions for data (lines) and Monte Carlo (dots) inclusive π^0's in shower energy bins. The vertical lines represent the lowest and highest values of the E9/E25 cut for that energy bin. For photons with $|cos\theta_\gamma| \leq 0.7071$, the 99%-efficient cut value is calculated from $cut = 0.955E^{0.0065} - 0.004E^{-1} + (1.6 \times 10^{-8})E^{-4} - 0.018E^{-0.5}$, where E is the shower energy in GeV. The plots have been normalized to equal area in each energy bin.

We also look at $m_{\gamma\gamma}$ in inclusive π^0's. We divide the π^0's into 10 equal momentum bins between 0 and 250 MeV/c. We subtract the fake-π^0 background from data π^0's using tagged background from generic Monte Carlo π^0's; the details of this are described in Appendix C. We compare these background-subtracted data distributions with the tagged-π^0 $m_{\gamma\gamma}$ distributions from generic Monte Carlo. Figure B.3 shows this comparison for all momenta. The Monte Carlo distribution is substantially narrower and does not reproduce a feature on the high side of the data distribution.

B.2.2 Δm for $D^{*0}\ell\nu$ candidates

Finally, we look at Δm for $D^{*0}\ell\nu$ candidates in data and generic Monte Carlo. Figure B.4 shows a fit to the Δm distributions using the background function we use in our analysis[1] and a simple Gaussian shape for the signal peak. Unlike the cases of `E9/E25` and $m_{\gamma\gamma}$, where we intend to use our distributions to tune the Monte Carlo, for Δm we are merely checking for consistency. We find the width for the data Δm peak to be 0.850 ± 0.048 MeV/c^2, while we find a width of 0.743 ± 0.018 MeV/c^2 for the generic Monte Carlo, a difference of 0.41 ± 0.10 MeV/c^2 when the widths are subtracted in quadrature.

[1]The function is $n(\Delta m - m_{\pi^0})^a e^{b(\Delta m - m_{\pi^0})}$, where we vary n, a, and b.

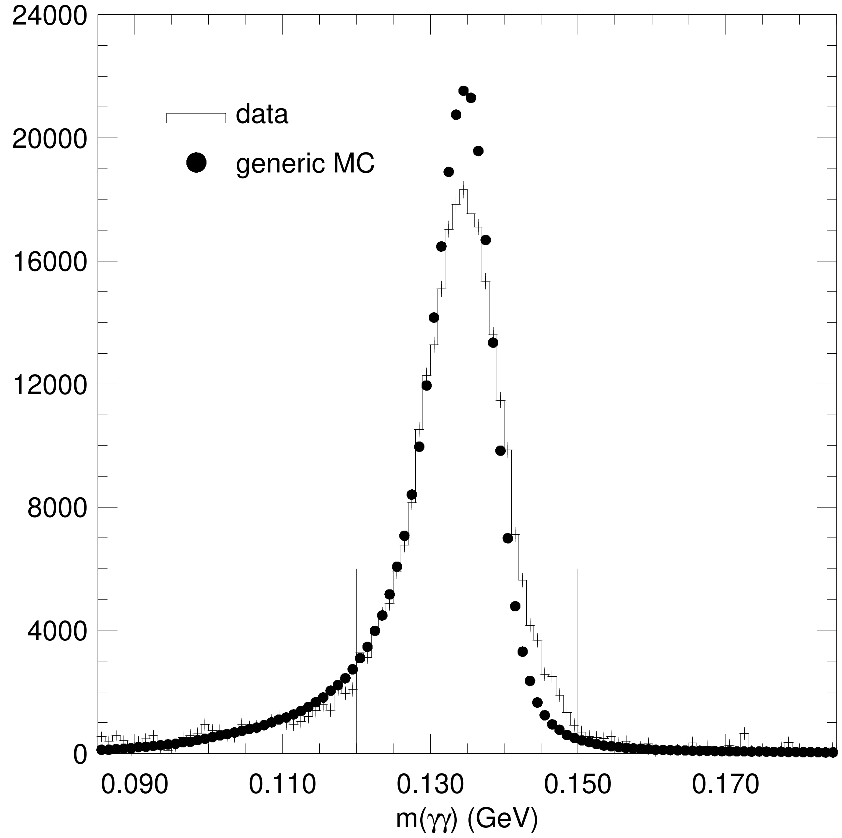

Figure B.3: The $m_{\gamma\gamma}$ distribution for data and Monte Carlo inclusive π^0's with momentum less than $250\,\mathrm{MeV}/c$. The vertical lines represent our cut. The Monte Carlo π^0's have been tagged; the fake-π^0 background has been subtracted from the data π^0 candidates. The plots have been normalized to equal area.

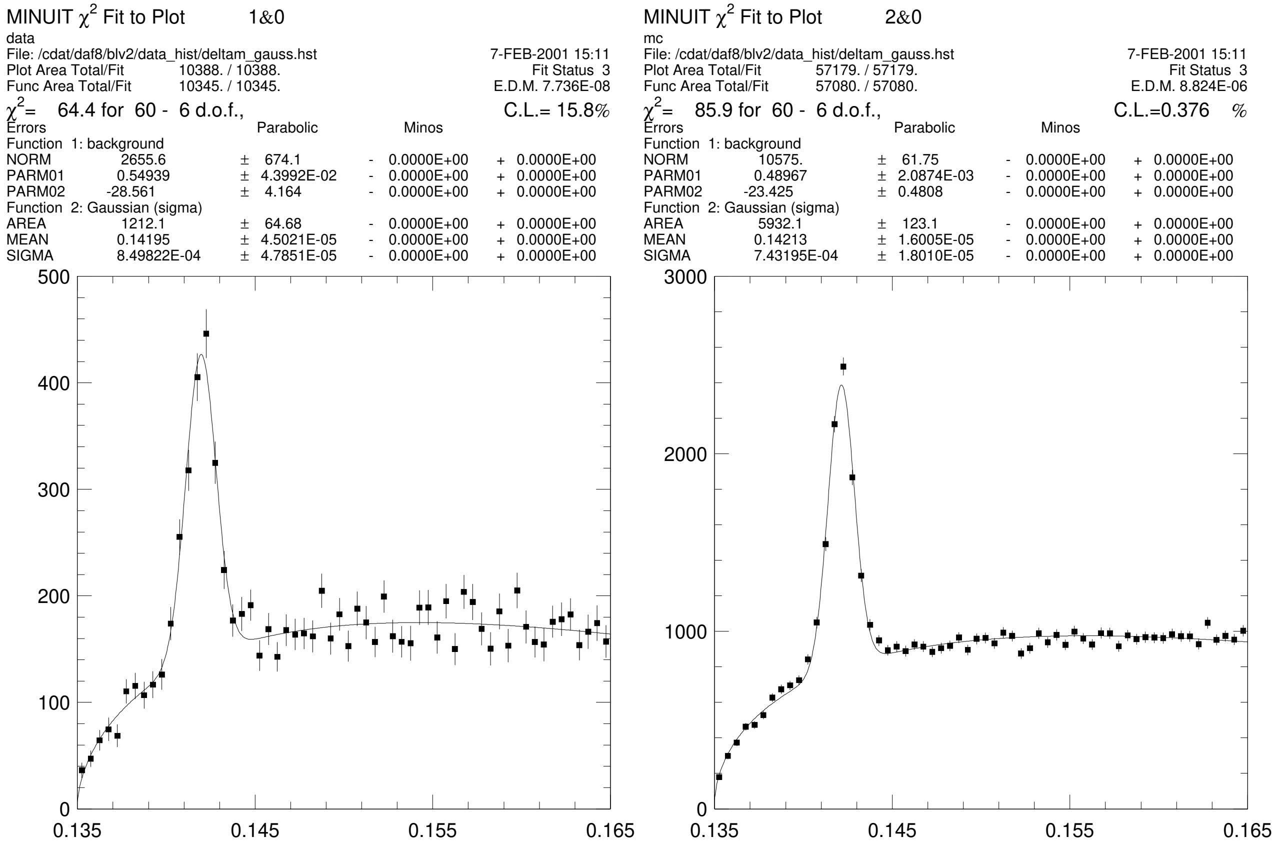

Figure B.4: Fits to the Δm distributions of $D^{*0}\ell\nu$ candidates for data (left) and generic Monte Carlo (right).

B.3 Monte Carlo parameters that affect slow-π^0 efficiency

Some Monte Carlo parameters strongly affect the shape of the `E9/E25` and $m_{\gamma\gamma}$ distributions; others may still affect slow-π^0 efficiency while having little effect on the shape of `E9/E25` and $m_{\gamma\gamma}$. We describe all such parameters here, noting which we can change to make the Monte Carlo `E9/E25` and $m_{\gamma\gamma}$ distributions a better match to the data.

B.3.1 Calorimeter noise

There are two categories of noise that are put on the calorimeter crystals. The first type, incoherent noise, is applied crystal by crystal. For each crystal, a random number is generated from a Gaussian distribution, multiplied by a constant σ for that crystal, and added to that crystal's signal. Changing this noise affects both `E9/E25` and $m_{\gamma\gamma}$.

The second type of noise is applied to groups of crystals and is termed coherent noise. The crystals are put in groups of 48 according to their hardware connections (i.e. half of the crystals connected to the same board). A random number is again generated from a Gaussian distribution, multiplied this time by a group σ, and then the same noise is added to each of the 48 crystals in that group. Changing this noise has small effects on `E9/E25` and $m_{\gamma\gamma}$.

B.3.2 Material

The material between the interaction point and the calorimeter affects the efficiency of the calorimeter. Photons that interact with material closer to the beam pipe tend to not be reconstructed in the calorimeter, while photons that interact with material closer to the calorimeter tend to deposit some fraction of their energy in the calorimeter and are still reconstructed. For that reason, we divide the material in `CLEOG` into "inner" material, which includes all material at radii smaller than the outer DR cathode, and "outer" material, which includes material from the outer DR cathode to the inner CC support structure. Since photons that interact in the inner material are generally not reconstructed, changing the inner material has little or no effect on `E9/E25` and $m_{\gamma\gamma}$. If a photon starts its shower outside the inner region but before it reaches the calorimeter, both the shape of the shower in the calorimeter and its reconstructed energy are affected. Changing the outer material changes the shape of the $m_{\gamma\gamma}$ low-side tail and makes fairly small changes to the `E9/E25` distribution.

B.3.3 Calorimeter crystal gains

The crystal gains (electronic-gain corrected ADC counts to energy conversion) are calibrated using showers with energies of about 5 GeV, which is much higher than the energies we see for slow π^0's (30-230 MeV). It is possible that a non-linearity exists that would make the gains depend on the shower (or crystal) energies. Comparison of Monte Carlo and data crystal response[2] leaves room for a small scattering in the crystal gains at low crystal energies that does not exist at higher energies.

Since we only use our modified Monte Carlo to generate slow π^0's, which have low-energy showers, we apply a scatter to the gain at all crystal energies.[3] We add this scatter in the subroutine `cceadc.F`. We multiply the gain of each crystal by $1 + rs$, where r is a Gaussian random number and different for each crystal, and s is the percent scatter divided by 100 (*e.g.* if we add a 3.2% scatter, we multiply times $1 + r(0.032)$). Adding a scatter to the crystal gains has a small effect on `E9/E25`, but a significant effect on the width of $m_{\gamma\gamma}$.

B.3.4 CUTGAM

In `CLEOG`, the parameter `CUTGAM` describes the lowest energy to which `GEANT` (through `CLEOG`) will track photons; when the energy of a photon falls below this cutoff, all of its energy is deposited in the current volume. The value of this cutoff can be changed at run-time with an `FFREAD` command (`CUTS 0.0001`). In the calorimeter, the value of this cutoff can affect the shape of showers by restricting the extent to which showers can spread out, thereby affecting the value of `E9/E25`. The default value of this cutoff is 1 MeV, which is chosen as a compromise between CPU time and accuracy. Lowering this cutoff can affect the shape of showers by allowing showers to expand further.

[2]Done by Brian Heltsley.

[3]In effect, we are only adding this scatter at low energies. This is not the correct thing to do in general, since it adds a scatter independent of crystal energy.

B.3.5 Event environment

Finally, the event environments in data and Monte Carlo can affect slow-π^0 efficiency differently. The effects of the event environment can be seen by comparing `E9/E25`, $m_{\gamma\gamma}$, and Δm for events with only slow π^0's and $D^{*0}\ell\nu$ signal Monte Carlo events. Figures B.5 and B.6 show these effects. While it is difficult to change the event environment in the Monte Carlo, we can gauge the effect of differences between the data and Monte Carlo events environments by embedding.

B.4 Method

Here we describe an error we found in the Time of Flight material definition in `CLEOG` and how we improve the agreement of the Monte Carlo `E9/E25` and $m_{\gamma\gamma}$ distributions with data. We also describe how we determine the efficiency correction for $D^{*0}\ell\nu$ π^0's and how we determine the uncertainty on this correction.

B.4.1 Correcting an error in the Time of Flight material

Before we tune `E9/E25` and $m_{\gamma\gamma}$, we first make a correction to the Time of Flight (TOF) material in `CLEOG`. After close inspection of the material in the outer detector (the outer DR cathodes and beyond), we discovered that the radiation length entered in the description of the TOF material for the TOF barrel and endcap detectors (`KMATBS` and `KMATES`) is too short. `GEANT` calculates the radiation length for each material based on the atomic weight and atomic number read in for that material. The default values entered for the scintillator material are $A = 20$ and

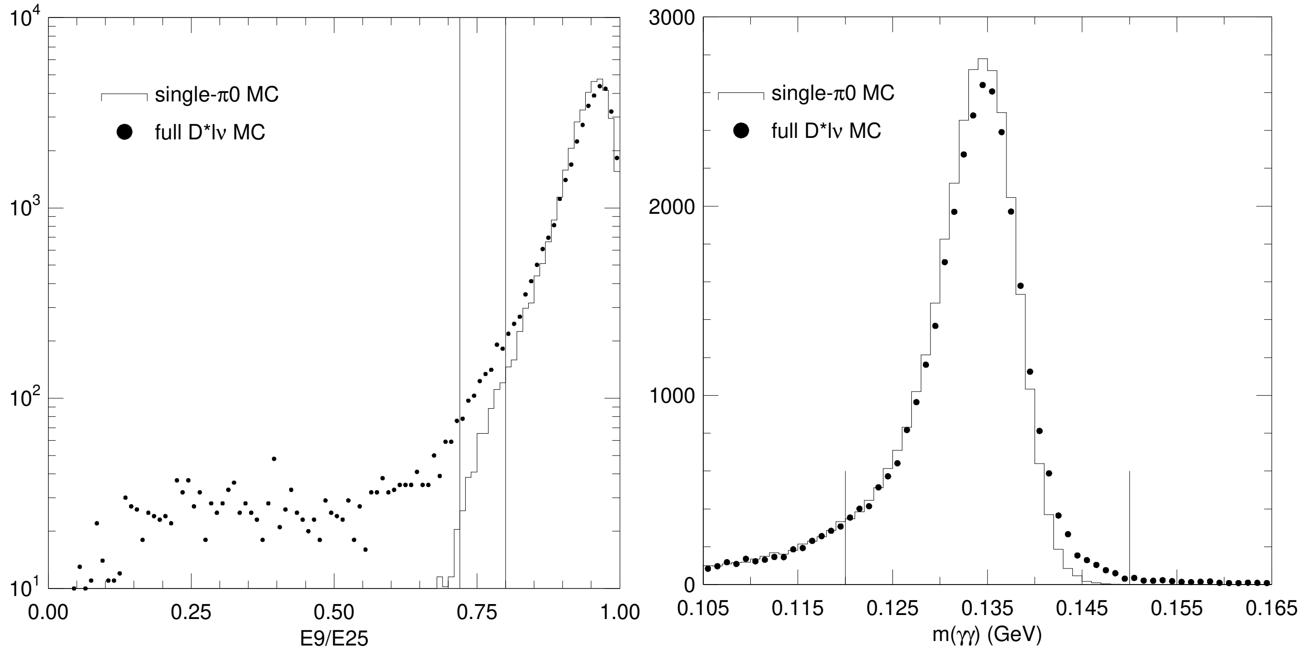

Figure B.5: The `E9/E25` (left) and $m_{\gamma\gamma}$ (right) distributions for π^0's from single-π^0 events and fully simulated tagged $D^{*0}\ell\nu$ events. The plots are normalized to equal area. The `E9/E25` plot includes only showers with energy less than 90 MeV. The vertical lines represent the lowest and highest values of the cut in this energy region for `E9/E25` and our cut limits for $m_{\gamma\gamma}$.

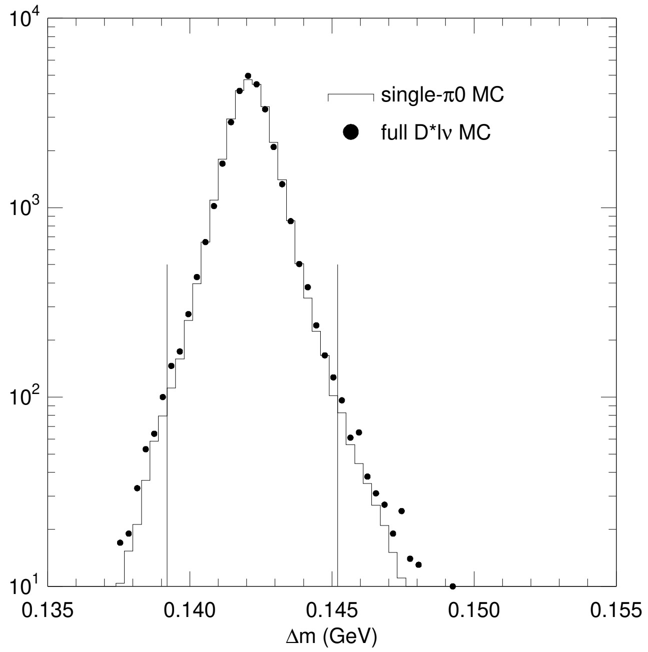

Figure B.6: The Δm distributions for π^0's from events with only π^0's (single-π^0 events) and fully simulated tagged $D^{*0}\ell\nu$ events. The vertical lines represent our cut limits. The plots are normalized to equal area.

$Z = 10$. This leads to a radiation length of 28.6 cm, which is quite different from the value of 43.8 cm quoted in the Particle Data Booklet for scintillator material.[4] The default values for the radiation length and the thickness of the TOF scintillator lead to the material in the TOF barrel detector making up 16.7% of a radiation length. Using the correct radiation length and making some assumptions about the amount of aluminum foil and electrical tape wrapped around each scintillator,[5] we calculate there should be 11.6% of a radiation length for the TOF, which corresponds to a radiation length of 41.2 cm. Accordingly, we change A and Z to 12 and 6, respectively, in `CLEOG`.[6] This change makes negligible difference to the `E9/E25` distribution, but significantly changes the shape of the low-side $m_{\gamma\gamma}$ tail. This is our first step, albeit backwards, towards matching the data distributions.

B.4.2 Tuning the Monte Carlo `E9/E25` and $m_{\gamma\gamma}$ distributions to the data

From the inclusive-π^0 `E9/E25` and $m_{\gamma\gamma}$ distributions, we determine by how much the distributions need to change. In the case of `E9/E25`, we find how much the peak of the distribution needs to be moved; for $m_{\gamma\gamma}$, we determine how much width needs to be added in quadrature. We next generate events containing only slow

[4]The PDG gives the radiation length for polyvinyltolulene with a carbon-to-hydrogen ratio essentially identical to that of the TOF scintillators.

[5]We use 0.015 cm aluminum and 0.096 cm carbon (for electrical tape). We got this from examining an actual endcap TOF counter, which had 2 layers of aluminum foil on each side and an average of 2 layers of electrical tape on each side. We assumed the same wrapping was used on the barrel counters.

[6]The endcap counters have the same thickness as the barrel counters, so the same changes should be made to A and Z in the endcap.

π^0's (called "single π^0's"from now on) with the default Monte Carlo. Then, we generate more single-π^0 events using a `CLEOG` where certain parameters have been modified. We compare the `E9/E25` and $m_{\gamma\gamma}$ distributions for the "default" events and the "modified" events. We vary our modifications until the difference between the "modified" and "default" π^0 distributions match the differences between the data and generic Monte Carlo inclusive π^0's. We end up with a version of Monte Carlo which does a better job of simulating the data `E9/E25` and $m_{\gamma\gamma}$ distributions. We use this Monte Carlo to generate π^0's, which we embed in data events. The `E9/E25` and $m_{\gamma\gamma}$ distributions of these embedded π^0's should then match those for real data π^0's.

We generate events containing only π^0's by generating $B^- \to D^{*0}\,\ell^-\,\bar{\nu}_l$ events and forcing the D^0, the lepton, and the other B in the event all to decay to neutrinos. We require the generated lepton to have a momentum between 0.8 and 2.4 GeV/c and to have $|\cos\theta_{lepton}| \leq 0.7071$. We also require both of the photons from the π^0 decay to be in the region $|\cos\theta_\gamma| \leq 0.7071$. This allows us to have a π^0 sample with the same momentum spectrum as the π^0's from $B^- \to D^{*0}\,\ell^-\,\bar{\nu}_l$ events. The momentum spectrum is shown in Figure B.7.

Both the incoherent calorimeter noise and `CUTGAM` have significant effects on the shape of `E9/E25`. The Monte Carlo has been calibrated with the default values for these parameters, and changing them throws the calibration off. While we can account for this for either parameter at some level (see Appendix E), changing the incoherent noise has more predictable effects, since it essentially adds a common amount of noise to all showers. Since our goal is to determine not just

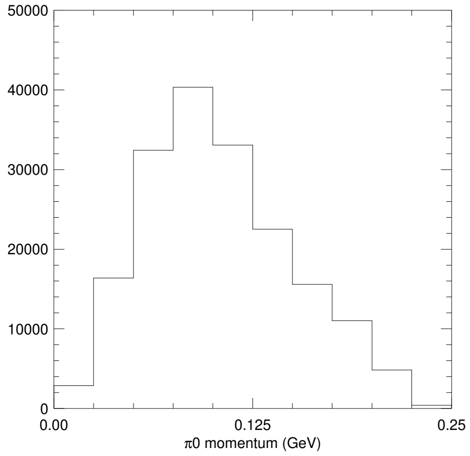

Figure B.7: The π^0 momentum spectrum for $D^{*0}\ell\nu$ Monte Carlo events with the cuts listed in the text.

an uncertainty but an efficiency correction, we choose to increase the amount of incoherent noise to match the `E9/E25` distributions and take the efficiency change from varying `CUTGAM` to be an uncertainty.

Looking at the shapes in Figure B.2, we quantify the shape difference by determining the peak of each distribution. These peak values are shown in Figure B.8. Also shown in Figure B.8 are the mean `E9/E25` values calculated for the range between an energy-bin-dependent lower cutoff[7] and 1. We use the means as a cross-check since the peaks are limited by statistics. We determine that we should increase the incoherent noise by 55±5% to match the `E9/E25` peaks. The peak

[7]The cutoffs are 0.80, 0.84, 0.88, 0.90, 0.92, and 0.94 for bins 1, 2,...6, where the bins are 30 MeV wide and start at 30 MeV.

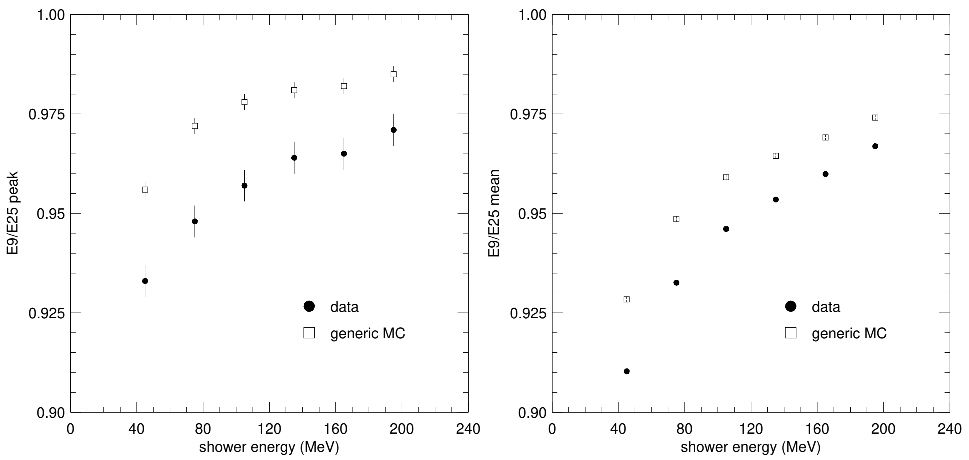

Figure B.8: The peak (left) and mean (right) values of `E9/E25` for data and generic Monte Carlo inclusive π^0's in energy bins.

shifts for Monte Carlo with the incoherent noise increased by 55% and 60% are shown in Figure B.9. Figure B.10 shows the mean shifts for the same noise increase.

Increasing the incoherent noise increases the width of $m_{\gamma\gamma}$, but not enough to match the data. We quantify the width difference by fitting the central part of the $m_{\gamma\gamma}$ distribution to a Gaussian. We then subtract the Monte Carlo widths from the data widths in quadrature. The widths and differences are listed in Table B.1. These widths already include any event environment effects which may increase the width, so we can use single-π^0 Monte Carlo to determine what modifications are necessary to match the width increases. To saturate the difference, we find we must add a scatter of 3.2$\pm$0.2% to the gains. The uncertainty includes the statistical uncertainty from the inclusive π^0's and our single-π^0 samples. The width added

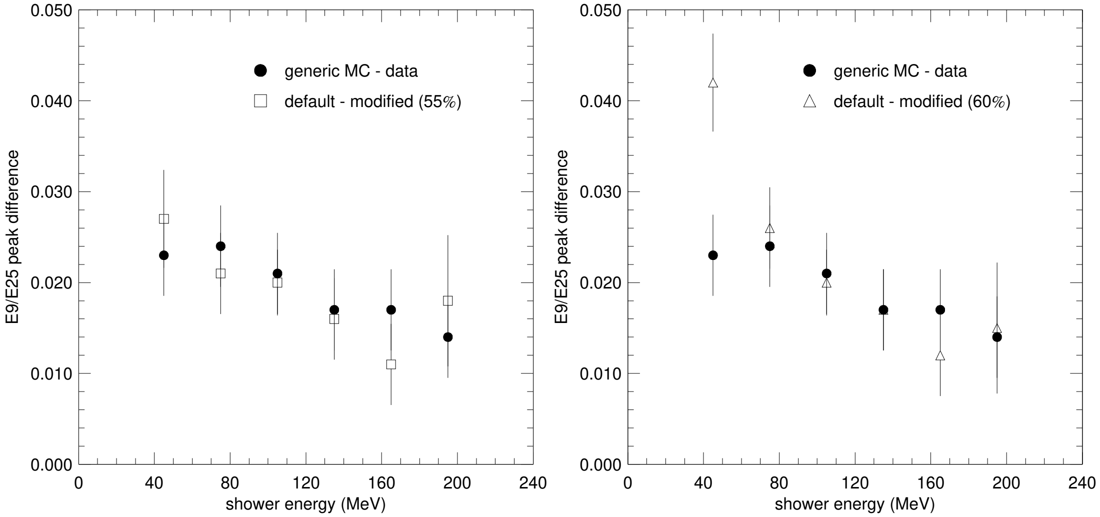

Figure B.9: The dots show the difference in the `E9/E25` peak values versus shower energy for data and Monte Carlo inclusive π^0's. The open symbols show the shift in the `E9/E25` peak values for single-π^0 Monte Carlo generated with the default incoherent noise value and with a modified value. The left plot shows the shift for an increase of 55%, and the right plot shows the shift for an increase of 60%.

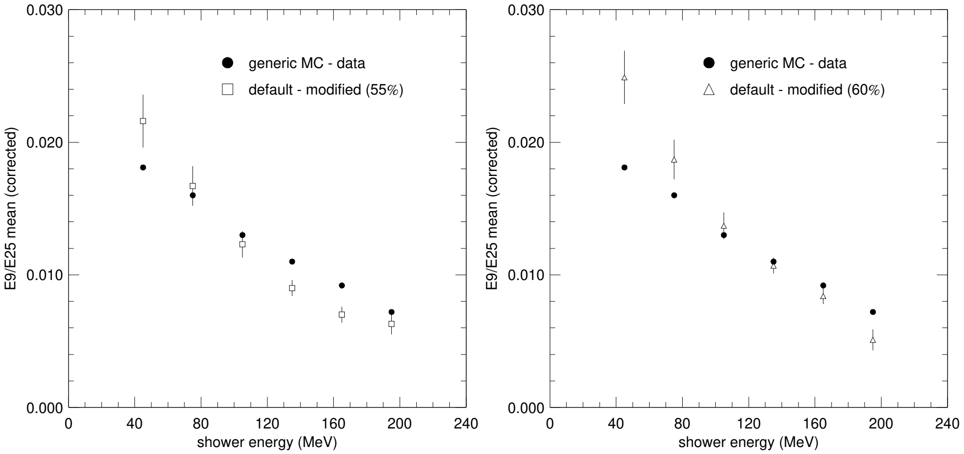

Figure B.10: The dots show the difference in the `E9/E25` mean values for data and Monte Carlo inclusive π^0's. The open symbols show the corrected shift in the `E9/E25` peak values for single-π^0 Monte Carlo generated with the default incoherent noise value and with a modified value. The left plots shows the shifts for an increase of 55%, and the right plot shows the shifts for an increase of 60%. The raw mean shifts (not shown) do not follow the same trend versus energy as the inclusive π^0 means; this difference seems to be entirely due to the fact that the single-π^0 Monte Carlo has no fake background tail to affect the mean. We have attempted to correct for this by artificially applying a tail to the single-π^0 `E9/E25` distributions. We describe how we apply this tail in Appendix D. Our method goes a long way towards compensating for this effect, but does not entirely remove it.

in Monte Carlo when we correct the TOF material, increase the incoherent noise, and add gain smearing is compared to the width we need to add in Figure B.11.

The three modifications to the Monte Carlo,

- correcting the radiation length of the TOF material,
- increasing the incoherent noise σ's by 55%, and
- adding a gain scatter of 3.2%,

make up what we from now on call the "Modified Monte Carlo". We call the Monte Carlo without these modifications the "Default Monte Carlo". We use both to determine an efficiency correction for slow π^0's, as we describe in the following section.

B.4.3 Finding the data-Monte Carlo efficiency difference

We choose to do our efficiency study by embedding Monte Carlo π^0's in both generic $B\bar{B}$ Monte Carlo and data events rather than using single-π^0 events so that the efficiency changes we measure include the effects of the event environment on the `E9/E25`, $m_{\gamma\gamma}$, and Δm shapes. We embed into events chosen with the same dataset balance as our data.

We run `CLEOG` to produce `.fzx` files of single-π^0 events. We use the `STRP` processor to get the information from the `.fzx` events, with one minor modification. `STRP` does not save the ADC count for a crystal; it instead converts the crystal ADC count to an energy. In the default `STRP`, the crystal energy information

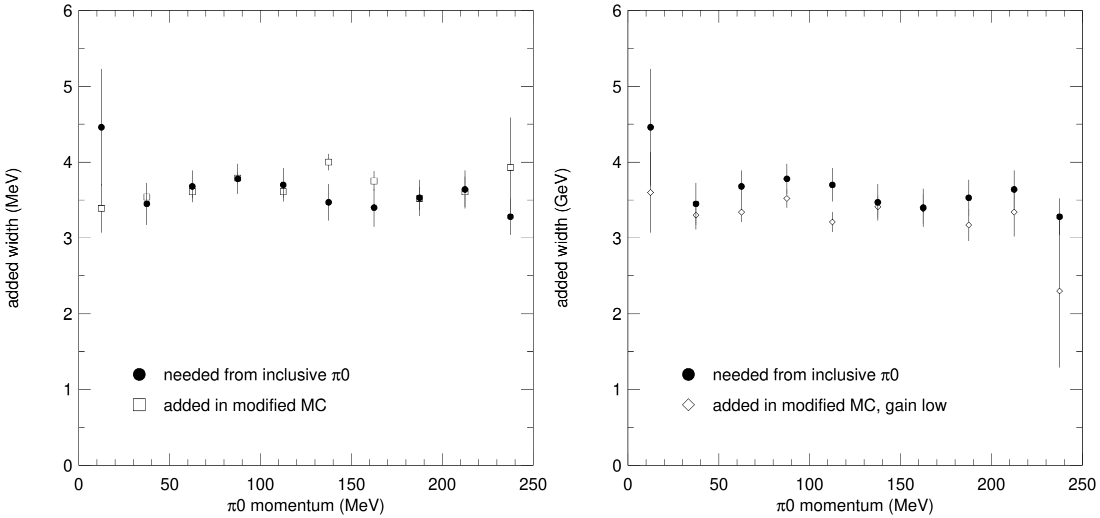

Figure B.11: The width that needs to be added to $m_{\gamma\gamma}$ from inclusive π^0's in momentum bins (filled circles) is plotted along with the width that is added by our Modified Monte Carlo. The left plot shows the added width for the changes from TOF material, incoherent noise, and a gain scatter of 3.2%. The right plot shows the added width for the same changes, except with a gain scatter of 3.0%. This 0.2% drop in scatter accounts for the uncertainty from the statistical uncertainty on the inclusive-π^0 widths and the single-π^0 widths.

Table B.1: The $m_{\gamma\gamma}$ widths from simple Gaussian fits to the inclusive π^0 distributions. The difference is calculated by subtracting the data and Monte Carlo widths in quadrature.

π^0 Momentum (MeV/c)	Data width (MeV/c^2)	Monte Carlo width (MeV/c^2)	Difference (MeV/c^2)
0-25	6.10±0.56	4.16±0.08	4.46±0.77
25-50	5.42±0.18	4.18±0.03	3.45±0.28
50-75	5.53±0.14	4.13±0.02	3.68±0.21
75-100	5.61±0.14	4.15±0.02	3.78±0.20
100-125	5.53±0.15	4.10±0.02	3.70±0.22
125-150	5.36±0.16	4.08±0.02	3.47±0.24
150-275	5.23±0.16	3.97±0.02	3.40±0.25
175-200	5.30±0.16	3.95±0.02	3.53±0.24
200-225	5.37±0.17	3.96±0.02	3.64±0.25
225-250	5.13±0.15	3.93±0.02	3.28±0.24

is truncated at 1 MeV. This systematically throws out on average 0.5 MeV per crystal; in a 1 GeV shower this loss is not important, but in a 30 MeV shower it is quite significant. To avoid this problem, we save crystal energies down to 10 keV.

Using the `MERG` processor, we merge the π^0 information into bed events selected from generic Monte Carlo, on-resonance data, and off-resonance data. We make one[8] minor modification to the `MERG` processor. `MERG` converts the crystal energies it gets from the `STRP` files back into ADC counts. Since the crystal energies get truncated in `STRP`, the reconstructed ADC count is always slightly smaller than the generated ADC count (e.g. 516.998 instead of 517.000). `MERG` truncates the reconstructed ADC count, so the reconstructed value usually comes out 1 ADC count below the generated value for each crystal hit in a shower, effectively lowering each crystal energy by about 0.2 MeV. The cumulative effect is that the embedded shower has an energy that is too low by about 1.5 MeV. The solution is simple; we modify `MERG` to round the reconstructed ADC count rather than truncating it. This change completely eliminates this error.

For a complete discussion of how bed events are selected, see Bruce Berger's CBX about charged slow pion efficiencies [46]. We use the same bed events as the charged slow pion study. Briefly, the criteria for bed events are as follows:

- `KLASGL` $= 10$
- $N_{tracks} > 4$
- `R2GL` ≤ 0.4

[8] It's really two, since we also have to change the energy-to-ADC conversion to be consistent with the change to `STRP`.

- Require electron or muon:
  - $0.8\,\mathrm{GeV}/c \le p_{lepton} \le 2.4\,\mathrm{GeV}/c$
  - $|\cos\theta_{lepton}| < 0.7071$
  - `R2ELEC` > 3 for electron
  - `DPTHMU` > 5 and `MUQUAL` $= 0$ for muon

We select bed events from on-resonance data, off-resonance data, and generic $B\bar{B}$ Monte Carlo.

Once we have the π^0's embedded within the bed events, we look at those events and see if we can find the embedded π^0's. To be "found", a π^0 must pass the cuts that we require on the π^0's in our $B^- \to D^{*0}\,\ell^-\,\bar{\nu}_l$ analysis. To make the Δm cut, we form Δm with the generator-level information for the D^0. As mentioned in Section B.4.2, our modifications to the default Monte Carlo parameters (*i.e.* constants) throws off the calibration of the Monte Carlo. As a result, some energy (about $1\,\mathrm{MeV}$) gets added to each shower, which also causes $m_{\gamma\gamma}$ to increase. Since this is a calibration issue, and not some profound change to the simulation, we correct for this energy change. We describe how we correct for this change in Appendix E.

A look at the Δm shape of embedded π^0 candidates (see Figure B.22) shows a peak at the expected value of Δm and a significant background. We subtract π^0 candidates that also appear in the bed events, so the background comes from one of the showers we have embedded combined with a random shower in the bed event. This background makes up about 20% of the π^0 candidates in the Δm

signal region in embedded events. Since this background also occurs in our $D^{*0}\ell\nu$ signal Monte Carlo, and to be consistent with our procedure for calculating the $D^{*0}\ell\nu$ efficiency, we perform a Δm sideband subtraction for our results in w bins.[9] We use $0.147\,\mathrm{GeV}/c^2 \leq \Delta m \leq 0.165\,\mathrm{GeV}/c^2$ as our sideband, and we normalize the sideband contribution using the combinatoric scale factors from our $D^{*0}\ell\nu$ analysis. This sideband subtraction leaves about 35% of this background, or 7% of the candidates in the signal region.

We calculate the efficiency for each bed type (on-resonance, off-resonance, and Monte Carlo) as follows for each w bin:

$$\begin{aligned} \epsilon_{type} \;=\; & [(N_{found(embed),sig} - N_{found(bed),sig}) \\ & -s(N_{found(embed),side} - N_{found(bed),side})]/N_{bed}, \end{aligned} \tag{B.1}$$

where ϵ_{type} is the efficiency, sig or $side$ means in the Δm signal (0.1392-0.1452) or sideband (0.147-0.165) region, s is the combinatoric scale factor from our $D^{*0}\ell\nu$ analysis, $N_{found(embed)}$ is the number of π^0's found in the embedded events, $N_{found(bed)}$ is the number of π^0's found in the bed events, and N_{bed} is the number of bed events.

We calculate the π^0 efficiency for data events from ϵ_{on} and ϵ_{off}:

$$\epsilon_{data} = \left(\frac{1}{x_{B\bar{B}}}\right)\epsilon_{on} - \left(\frac{1-x_{B\bar{B}}}{x_{B\bar{B}}}\right)\epsilon_{off}, \tag{B.2}$$

[9] In our $D^{*0}\ell\nu$ analysis, we divide the data into 10 bins of w, where w is defined as the dot product of the 4-velocities of the B and D^* and is equal to the D^*'s relativistic γ in the B rest frame.

where $x_{B\bar{B}} = .749$ comes from the on/off ratio and the efficiency difference for on- and off-resonance events to pass the bed event selection cuts. The statistical uncertainty on $x_{B\bar{B}}$ has a negligible effect on ϵ_{data}.

Finally, we compare the π^0 efficiencies for Modified π^0's embedded in data events and Default π^0's embedded in Monte Carlo events. We calculate the efficiency difference

$$\Delta\epsilon = \frac{\epsilon_{data} - \epsilon_{MC}}{\epsilon_{MC}}. \tag{B.3}$$

B.4.4 Variations on the Modified Monte Carlo

The Modified Monte Carlo represents our "best guess" for determining slow-π^0 efficiency; however, there are some uncertainties in this determination. We make six variations to the Modified Monte Carlo and determine how the efficiency difference changes with each variation. We take the change in the efficiency difference to be the systematic uncertainty.

The six variations are:

- incoherent noise (IN): there is an uncertainty of 5% on the increase in the incoherent noise σ's. We change this increase to 60%, and decrease the gain scatter to 3.1% to keep the $m_{\gamma\gamma}$ widths the same.

- crystal gains (CG): There is an uncertainty of 0.2% on the gain scatter. We decrease the gain scatter to 3.0%.

- coherent noise (CN): According to Jesse Ernst, it is possible that the coherent σ's are wrong by up to 25%. We increase these σ's by 25%, while changing the incoherent noise increase to 50% and the gain scatter to 3.0% to keep the `E9/E25` and $m_{\gamma\gamma}$ distributions the same.

- inner material (IM): We increase the inner material by 10% based on a study done by Brian Heltsley [44].

- outer material (OM): There are no studies of which we are aware that probe the level of accuracy of the outer material. There is some certainty about the outer DR cathode material, since the inner DR cathodes are probed in the study of inner material. The rest of the material is fairly simple, but, wary of the TOF mistake, we increase the outer material by 15% as a conservative measure. We change the incoherent noise increase to 50% and the gain scatter to 3.0%.

- gamma cutoff (GAM): We lower `CUTGAM` to 0.1 MeV. This has a fairly noticeable effect on `E9/E25`, and we must change the incoherent noise increase to 35% to keep the `E9/E25` peak in the right place. We also increase the gain scatter to 3.6%.

B.5 Results

In this section we present our results for the slow π^0 efficiency difference and the uncertainty on that difference.

B.5.1 Efficiency difference

We measure the following efficiencies using 1.6×10^4 embedded π^0's and performing the Δm sideband subtraction:

- $\epsilon_{on} = 0.5925 \pm 0.0038$,
- $\epsilon_{off} = 0.5873 \pm 0.0038$, and
- $\epsilon_{MC} = 0.5980 \pm 0.0038$,

where ϵ_{on} is the efficiency for Modified Monte Carlo π^0's embedded in on-resonance data events, ϵ_{off} is the efficiency for Modified Monte Carlo π^0's embedded in off-resonance data events, and ϵ_{MC} is the efficiency for Default Monte Carlo π^0's embedded in generic Monte Carlo events. From these we get $\epsilon_{data} = 0.5980 \pm 0.0060$, which implies a slow-$\pi^0$ efficiency difference of $-0.62 \pm 1.08\%$. The results are given in w bins in Table B.2 and plotted in Figure B.12.

B.5.2 Systematic uncertainty on the efficiency difference

There are two types of contributions to the systematic uncertainty on the efficiency difference. The first comes from the uncertainty on the values of the many `CLEOG` parameters, as we described in Section B.4.4. The second comes from the effect that the number of background showers has on π^0 efficiency and is described below.

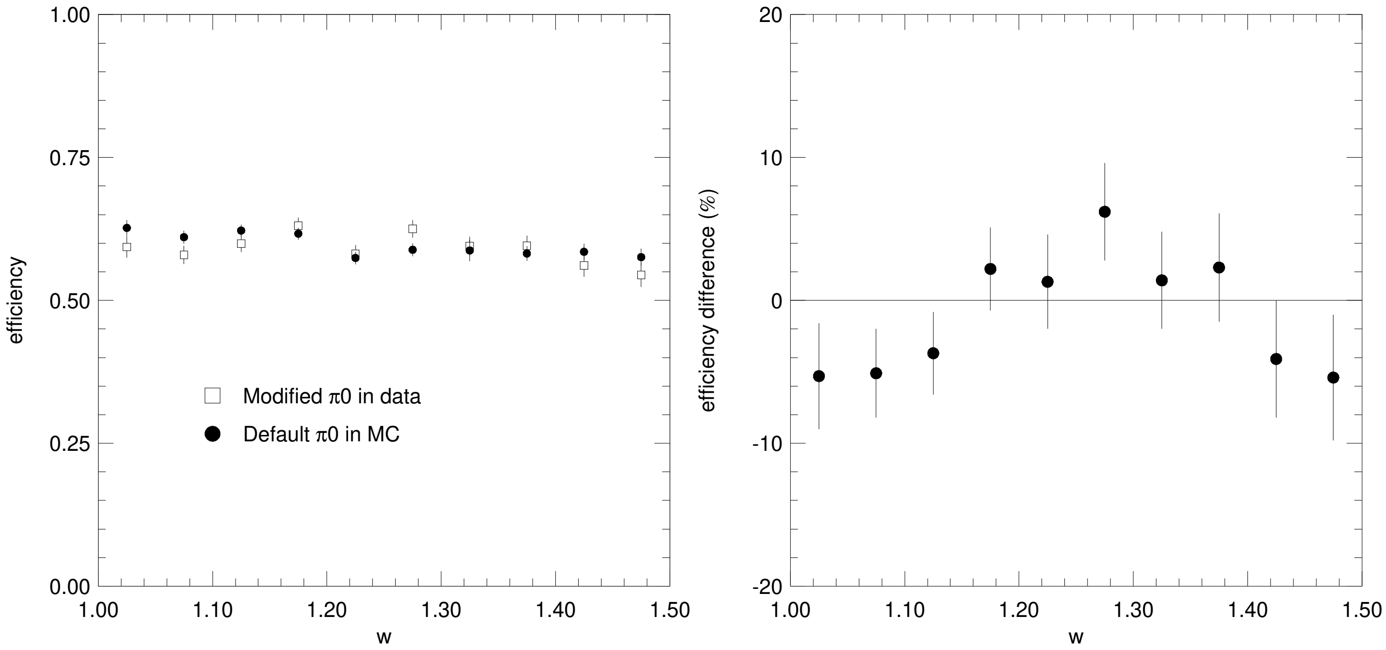

Figure B.12: The efficiency and efficiency difference, $(\epsilon_{data} - \epsilon_{mc)}/\epsilon_{mc}$, for reconstructing π^0's embedded in data and Monte Carlo in bins of w.

Table B.2: The data and Monte Carlo efficiencies and efficiency difference in w bins. The uncertainty on the efficiencies includes the statistical uncertainty from the combinatoric background scale factor, which largely cancels in the efficiency difference.

w	ϵ_{MC}	ϵ_{data}	Efficiency Difference (%)
1.00-1.05	0.6268±0.0149	0.5935±0.0198	-5.3±3.7
1.05-1.10	0.6106±0.0128	0.5797±0.0170	-5.1±3.1
1.10-1.15	0.6221±0.0122	0.5992±0.0159	-3.7±2.9
1.15-1.20	0.6167±0.0126	0.6305±0.0160	2.2±2.9
1.20-1.25	0.5742±0.0133	0.5818±0.0169	1.3±3.3
1.25-1.30	0.5885±0.0140	0.6250±0.0177	6.2±3.4
1.30-1.35	0.5873±0.0165	0.5953±0.0196	1.4±3.4
1.35-1.40	0.5820±0.0174	0.5955±0.0219	2.3±3.8
1.40-1.45	0.5850±0.0213	0.5611±0.0243	-4.1±4.1
1.45-1.51	0.5756±0.0219	0.5446±0.0256	-5.4±4.4
all	0.5980±0.0047	0.5943±0.0058	-0.6±1.1

Variations

We generate separate π^0 samples for each of the variations described in Section B.4.4. We embed each of these samples in data and recalculate the efficiency difference. We take the difference between the efficiency difference we calculate using the Modified Monte Carlo and the efficiency difference we calculate using a variation to be the systematic uncertainty due to that variation. The results of these variations are listed in Table B.3. Over all momenta, and with the Δm sideband subtraction, the changes in the efficiency difference are:

- incoherent noise: -3.5±0.8%
- crystal gains: -2.4±0.8%
- coherent noise: -2.0±0.8%
- inner material: -0.2±0.8%
- outer material: -0.4±0.8%
- `CUTGAM`: -2.1±0.8%

We take all of these uncertainties to be symmetric, with the exception of `CUTGAM` (there's clearly no benefit to raising `CUTGAM`). Adding the uncertainties in quadrature and including the statistical uncertainty, we get a total uncertainty from the variations of $^{+5.1}_{-5.6}\%$.

Table B.3: The systematic uncertainties in bins of w on the efficiency difference (includes Δm sideband subtraction) due to parameter uncertainty. The first column lists the w range for each bin. The second through seventh columns show the uncertainties in percent for the variations in incoherent noise (IN), crystal gains (CG), coherent noise (CN), inner material (IM), outer material (OM), and `CUTGAM` (GAM). The last column gives the statistical uncertainty for each variation.

w	IN	CG	CN	IM	OM	GAM	Uncertainty
1.00-1.05	6.2	-0.5	2.3	-2.1	1.2	0.4	3.1
1.05-1.10	-2.4	1.9	3.6	11.5	0.6	0.6	2.5
1.10-1.15	-4.0	-3.0	-1.4	-1.2	3.7	-0.1	2.4
1.15-1.20	-4.6	-6.0	-9.3	-4.0	-7.3	-7.5	2.4
1.20-1.25	-0.6	4.4	2.6	6.0	4.2	1.1	2.6
1.25-1.30	-9.9	-7.8	-3.9	-9.5	-3.7	-11.0	2.6
1.30-1.35	-6.9	-8.4	-4.5	-4.7	-0.9	-6.7	2.8
1.35-1.40	-7.2	-3.5	-13.1	-0.7	1.0	1.9	3.1
1.40-1.45	3.0	-2.4	4.3	-2.0	-1.5	2.8	3.3
1.45-1.51	-4.7	3.4	3.9	5.8	-1.2	4.4	3.7
all	-3.5	-2.4	-2.0	-0.2	-0.4	-2.1	0.9

Number of Showers

The number of showers in our bed events and in $B \to D^* \ell \bar{\nu}$ candidate events are quite similar for data and Monte Carlo (see Figure B.13). When we embed showers, however, we increase the number of showers in an event by 2 (on average). If the data and Monte Carlo efficiencies somehow depend differently on the number of showers, this difference could add a bias to our efficiency measurements.

To estimate the uncertainty due to this source, we calculate the efficiency for finding embedded π^0's in bins of the number of showers in the bed events for both data and Monte Carlo events. We fit the results to a straight line, as shown in Figure B.13. We use the slope from the fit to calculate the change in efficiency due to the difference in the number of showers. The numbers for this calculation are shown in Table B.4. We find that this effect changes the efficiency difference by 0.58±0.35%, which we take as an uncertainty of 0.68%.

B.5.3 Total π^0 efficiency uncertainty

We find an efficiency difference of $-0.6 \pm 1.1\%$, an uncertainty from the variations of $^{+5.1}_{-5.6}\%$, and an uncertainty from the number of showers of 0.7%. This leads to a total efficiency difference and uncertainty of $-0.6^{+5.3}_{-5.7}\%$.

B.6 Cross checks

We compare the `E9/E25` and $m_{\gamma\gamma}$ distributions for both the embedded Default and Modified Monte Carlo with data distributions. We also check to see if the

Table B.4: The efficiencies and slopes used to calculate the uncertainty due to the change in the number of showers. The second column (ϵ_{all}) gives the overall π^0 efficiency. The third and fourth columns give the mean number of showers in embedded events and $D^{*0}\ell\nu$ candidate events, respectively. The fifth column gives the correction we make to the number of showers. The sixth column gives the slope from a fit to the efficiency versus number of showers. The seventh column gives the correction we make to the efficiency, $\Delta\epsilon = \Delta N_{shower} \times slope$. The last column gives the percent change in the efficiency, $\Delta\epsilon/\epsilon$. The relative change in the efficiencies is $(1.59 \pm 0.24) - (1.01 \pm 0.25)$, or 0.58 ± 0.35.

	ϵ_{all}	N_{shower} Embed	N_{shower} $D^*\ell\nu$	Diff	Slope ($\times 10^{-4}$)	$\Delta\epsilon$	Δ_ϵ/ϵ (%)
data	0.5943	24.3	21.4	-1.9	-5.02 ± 0.75	0.0094 ± 0.0014	1.59 ± 0.24
MC	0.5980	27.2	25.2	-2.0	-3.05 ± 0.75	0.0060 ± 0.0015	1.01 ± 0.25

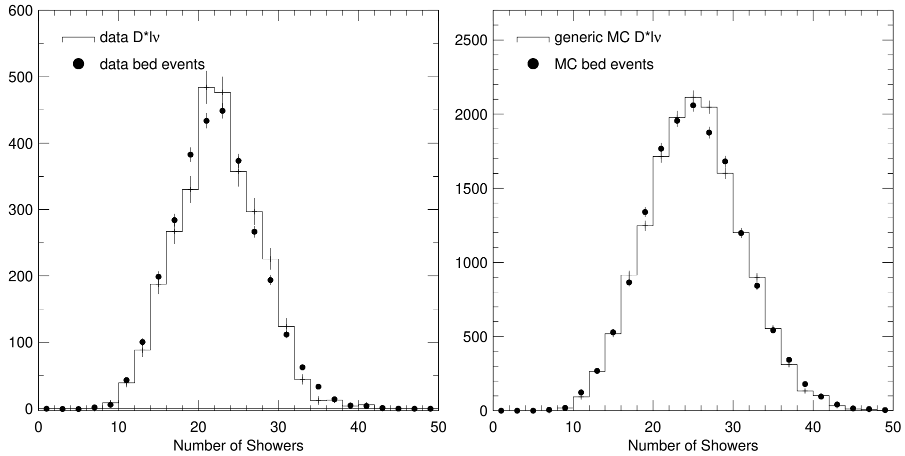

Figure B.13: The number of showers in $D^{*0}\ell\nu$ candidate events and our selected bed events for data (left) and Monte Carlo (right). The $D^{*0}\ell\nu$ candidates have all analysis cuts applied to them.

Modified Monte Carlo shows any increase in the width of the Δm peak. Finally, we check that the peak of $m_{\gamma\gamma}$ falls in the same place for data and Monte Carlo inclusive π^0's.

B.6.1 `E9/E25` and $m_{\gamma\gamma}$ distributions

Figures B.15 and B.16 show the `E9/E25` distributions for embedded π^0's and $D^{*0}\ell\nu$ candidates from data in two shower energy bins. There is a clear improvement in agreement between the Default and Modified π^0's. The `E9/E25` shape for the Modified Monte Carlo in the 90-180 MeV bin is not quite in agreement with the data, but the difference is covered by the change in shape with the variations. Fig-

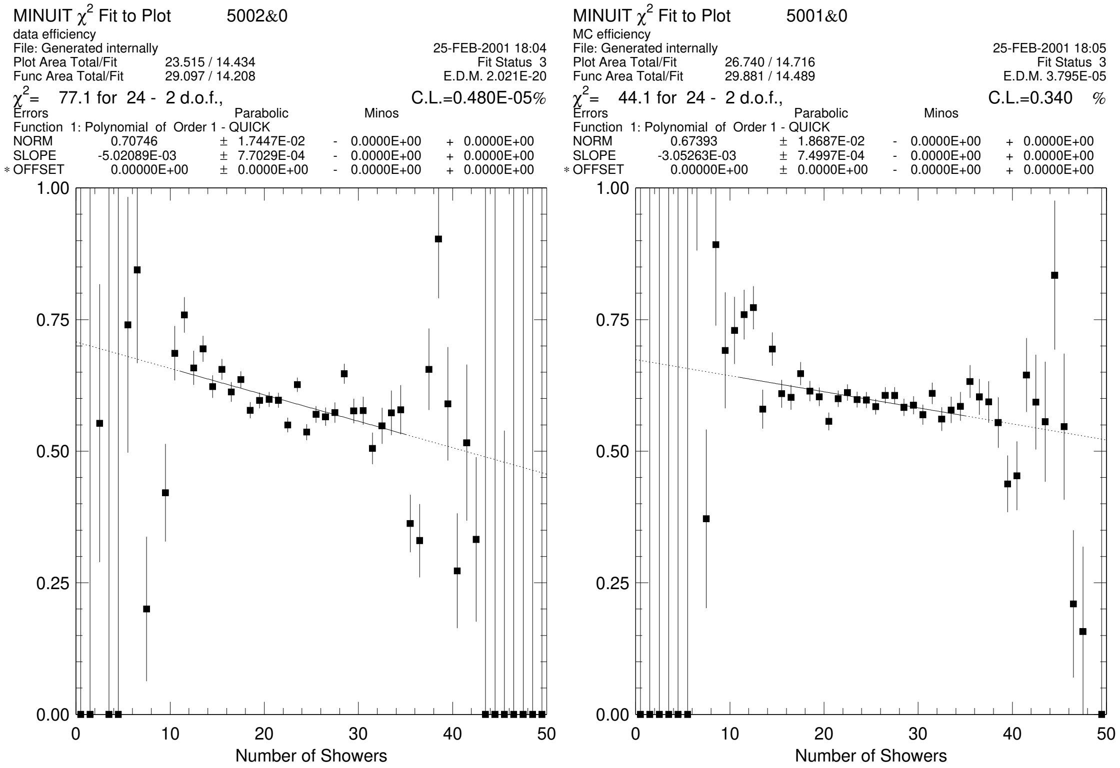

Figure B.14: The efficiency for embedded π^0's versus number of showers in the bed event for Modified π^0's embedded in data events (left) and Default π^0's embedded in Monte Carlo events (right).

ures B.17 and B.18 show how the `E9/E25` distribution changes with the variations to the Modified Monte Carlo.

The background in embedded events that comes from one of the showers we have embedded combined with a random shower in the bed event makes it difficult to directly compare the $m_{\gamma\gamma}$shape for real inclusive π^0's with correctly-reconstructed embedded π^0's. For calculating the efficiency in w bins, we subtract these background events using the Δm sideband, but it turns out that the component of this background that falls in the Δm sideband does not have the same shape in $m_{\gamma\gamma}$ as the component in the Δm signal region. The difference occurs primarily in the low-side-tail region of $m_{\gamma\gamma}$ ($0.120\,\mathrm{GeV}/c^2$ and less). We have tried to compensate using a tagged $m_{\gamma\gamma}$ shape for this background from $D^{*0}\ell\nu$ signal Monte Carlo, but this is not a perfect solution, since the energy distribution of the background showers in the signal Monte Carlo is not the same as the bed events (although it is close for the Monte Carlo bed events). The result is that the background-subtracted $m_{\gamma\gamma}$ shape for embedded events is lower than it should be for the low-side region, while the high-side shape is fine. We compensate by also plotting $m_{\gamma\gamma}$ for single π^0's, where the low-side tail is fine, but which we know does not have the correct high-side tail shape (which comes from the event environment). Figures B.19 and B.20 show the $m_{\gamma\gamma}$ distribution for Default and Modified π^0's and inclusive data π^0's. Looking at the low side of the single-π^0 plots (left plots) and the high side of the embedded-π^0 plots (right plots), we see that the agreement is good between data and the Modified Monte Carlo. Figure B.21

shows how the $m_{\gamma\gamma}$ distribution changes with the variations to the Modified Monte Carlo.

B.6.2 Δm width

Figure B.22 shows the Δm distribution for Modified Monte Carlo π^0's embedded in data events and Default Monte Carlo π^0's embedded in Monte Carlo events. From a fit to these distributions similar to the fits in Figure B.4, we find that the width of the Δm peak increases in quadrature by $0.507 \pm 0.041\,\mathrm{MeV}/c^2$. As reported in Section B.2.2, the generic Monte Carlo $D^{*0}\ell\nu$ candidates lacked $0.41 \pm 0.10\,\mathrm{MeV}/c^2$ in width. The fact that our modifications cause the Δm width to increase by the correct amount (within errors) is a great verification that our modifications are valid since we do not explicitly tune the width of this variable.

B.6.3 $m_{\gamma\gamma}$ peak

The efficiency for passing the $m_{\gamma\gamma}$ cut depends partly on where the peak of the $m_{\gamma\gamma}$ distribution falls. If the Monte Carlo and data were to have the exact same shape in $m_{\gamma\gamma}$ but were displaced, the π^0 efficiency for Monte Carlo and data would be different. Since our study deals exclusively with Monte Carlo π^0's, we were concerned that we might be overlooking a source of efficiency difference.

To compare the location of the $m_{\gamma\gamma}$ peak for data and Monte Carlo, we examine the means from the Gaussian fits to the $m_{\gamma\gamma}$ shapes used to determine the widths for data and Monte Carlo inclusive π^0's (Section B.4.2). We find that, over all momentum bins, the means are different by $0.01 \pm 0.02\,\mathrm{MeV}/c^2$, a difference to which our analysis is quite insensitive.

B.7 Conclusion

We find a π^0 efficiency difference and uncertainty of $-0.6^{+5.3}_{-5.7}\%$ for $D^{*0}\ell\nu$ π^0's. Using π^0 momentum bins, where we do not do a Δm sideband subtraction, our result is $-0.7^{+4.9}_{-5.3}\%$. These results are valid only for the particular π^0 momentum spectrum that we used, but we have included a way to calculate the uncertainty given a different momentum spectrum. This result is a large improvement over the previous best uncertainty measurement of 8.6% [42].

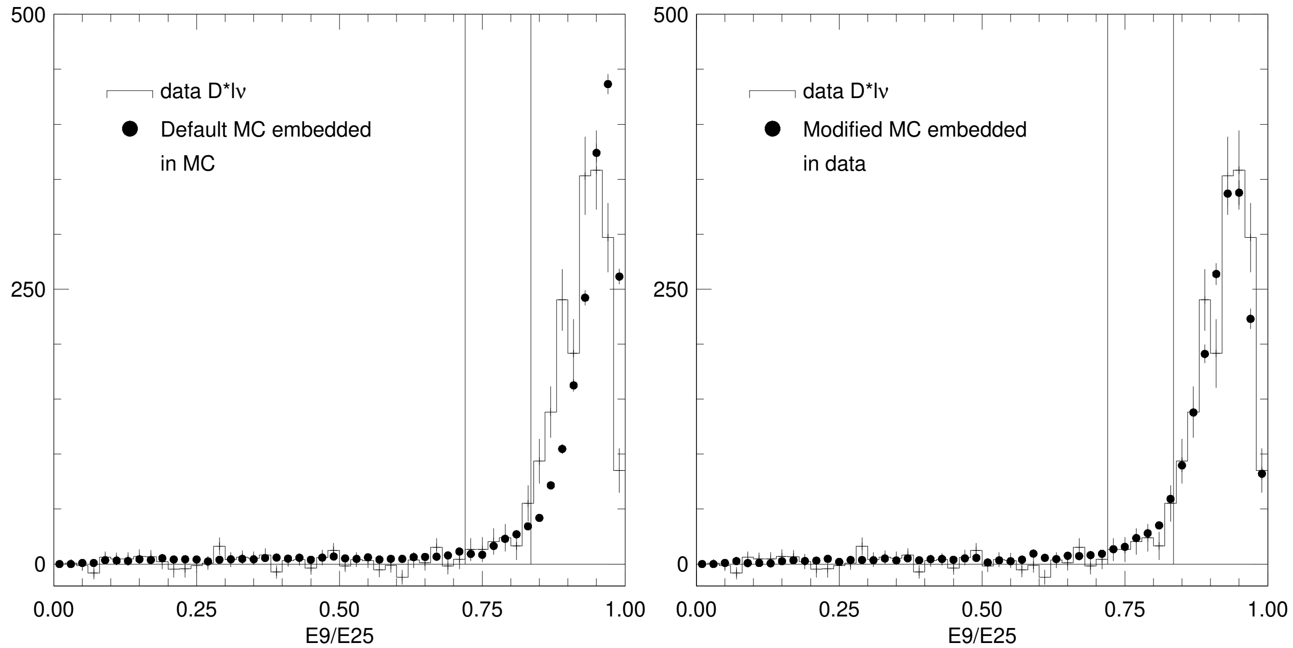

Figure B.15: The `E9/E25` distributions from π^0 candidate showers with momentum between 50 and 125 MeV/c and for showers with energy between 30 and 90 MeV from $D^{*0}\ell\nu$ data π^0's and embedded Monte Carlo π^0's. The left plot shows Default Monte Carlo π^0's embedded in Monte Carlo events. The right plot shows Modified Monte Carlo π^0's embedded in data events. The vertical lines show the lower and upper limits of the `E9/E25` cut for this shower energy range.

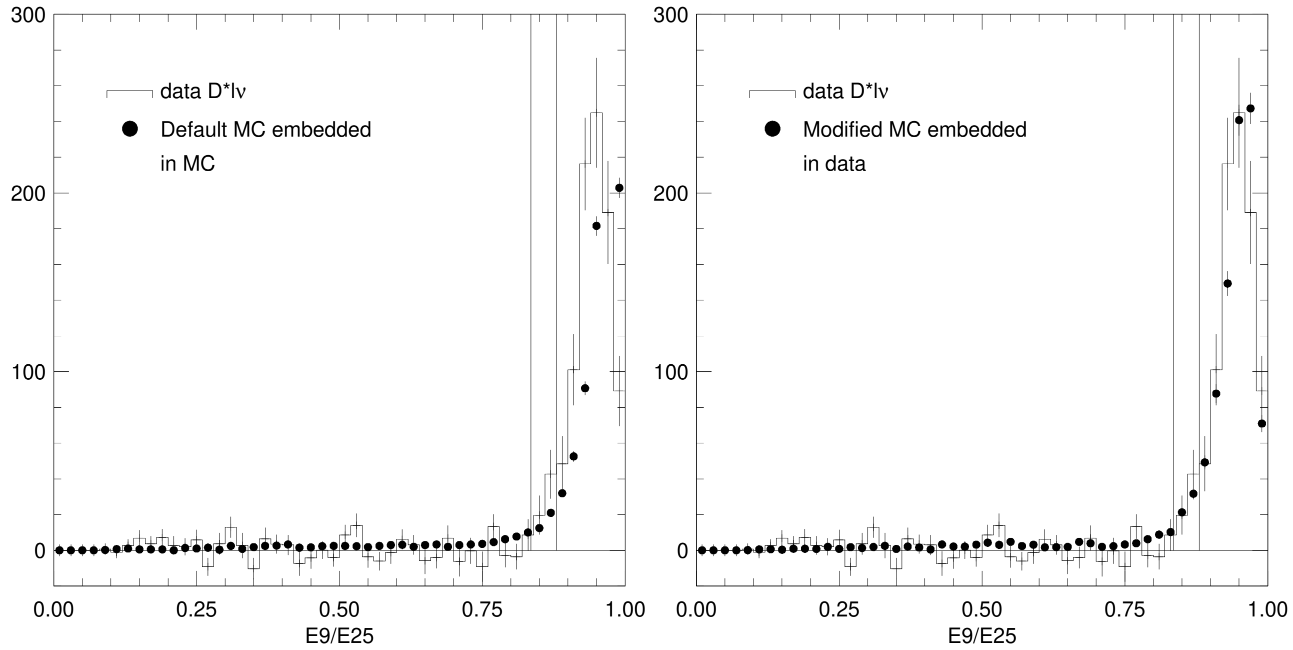

Figure B.16: The `E9/E25` distributions from π^0 candidate showers with momentum between 50 and 125 MeV/c and for showers with energy between 90 and 180 MeV from $D^{*0}\ell\nu$ data π^0's and embedded Monte Carlo π^0's. The left plot shows Default Monte Carlo π^0's embedded in Monte Carlo events. The right plot shows Modified Monte Carlo π^0's embedded in data events. The vertical lines show the lower and upper limits of the `E9/E25` cut for this shower energy range.

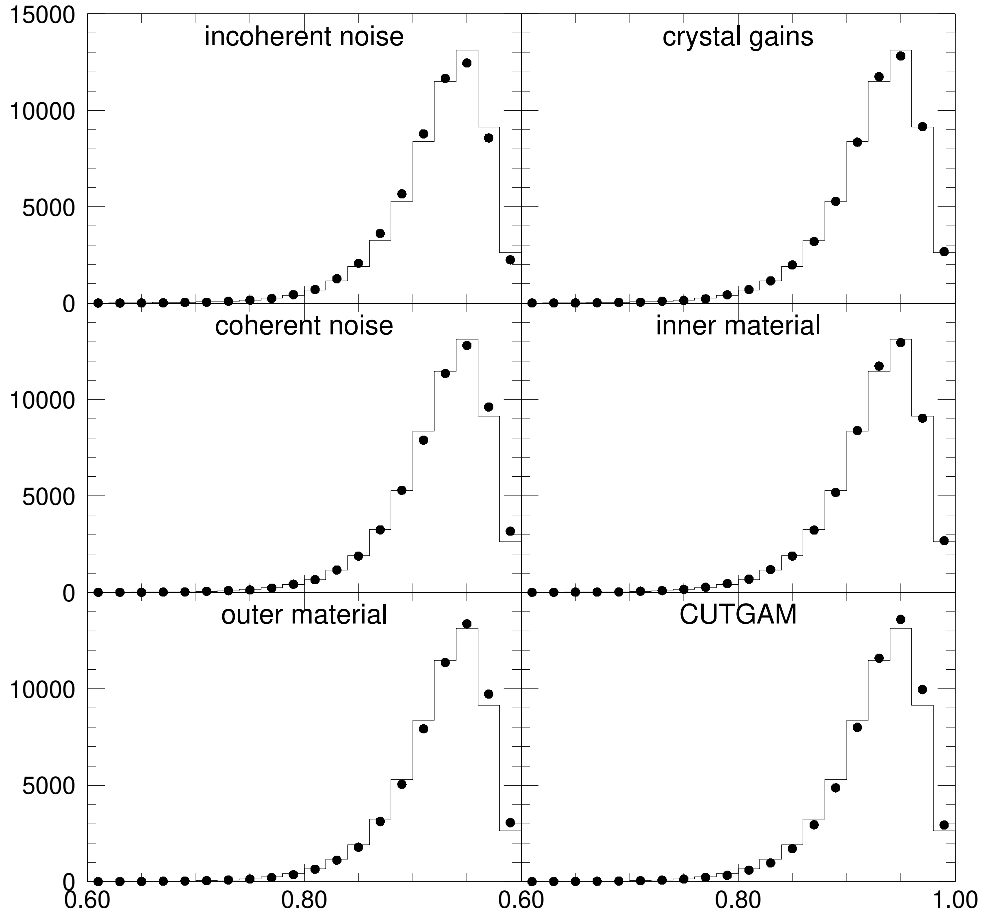

Figure B.17: The change in `E9/E25` for showers with energy between 30 and 90 MeV and with π^0 momenta between 50 and 125 MeV/c for the six variations (dots) compared to the Modified Monte Carlo (line). The plots are made from unembedded π^0's.

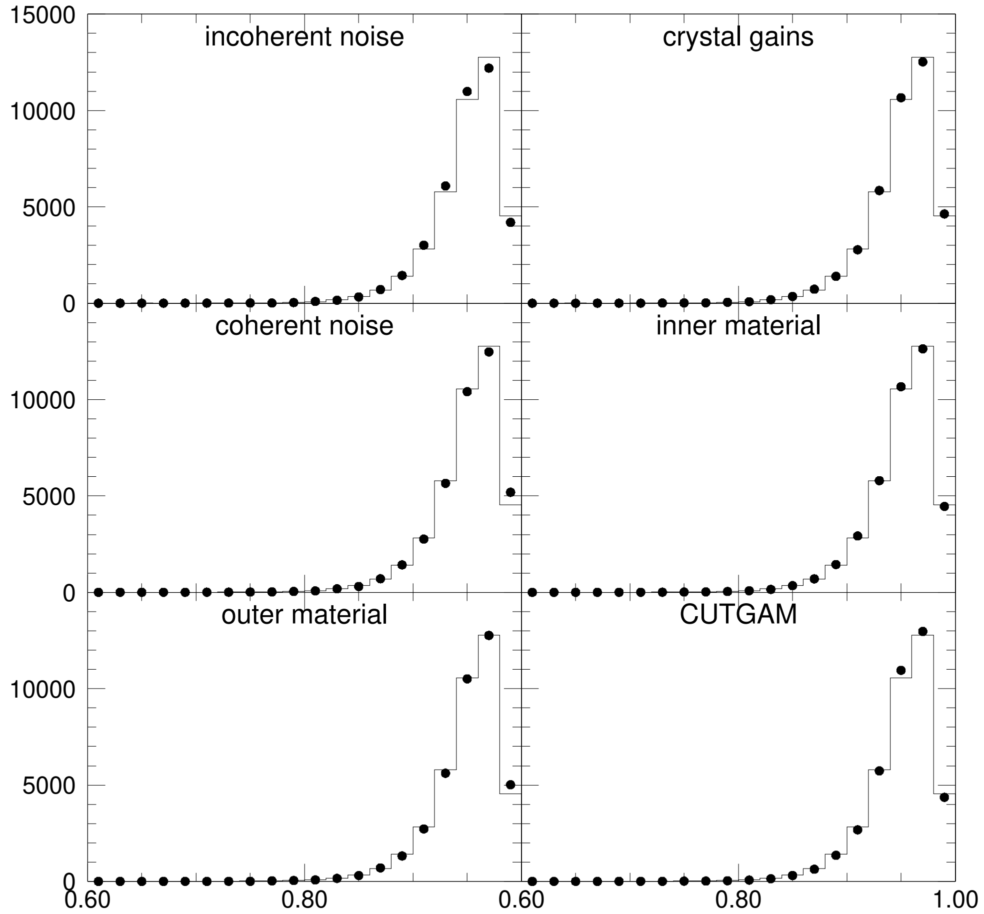

Figure B.18: The change in `E9/E25` for showers with energy between 90 and 180 MeV and with π^0 momenta between 50 and 125 MeV/c for the six variations (dots) compared to the Modified Monte Carlo (line). The plots are made from unembedded π^0's.

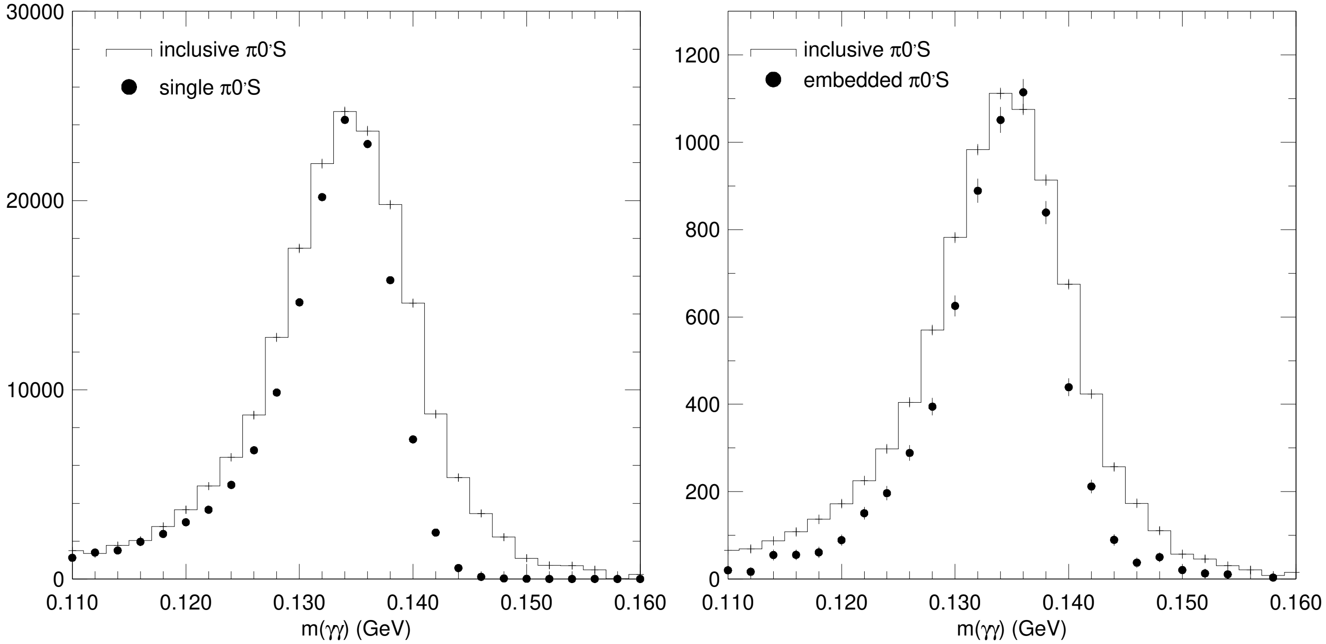

Figure B.19: The left plot shows the $m_{\gamma\gamma}$ distribution for data inclusive π^0's and Default single π^0's. The right plot shows $m_{\gamma\gamma}$ for data inclusive π^0's and embedded π^0's. The low-side tail of the embedded π^0's is discussed in the text.

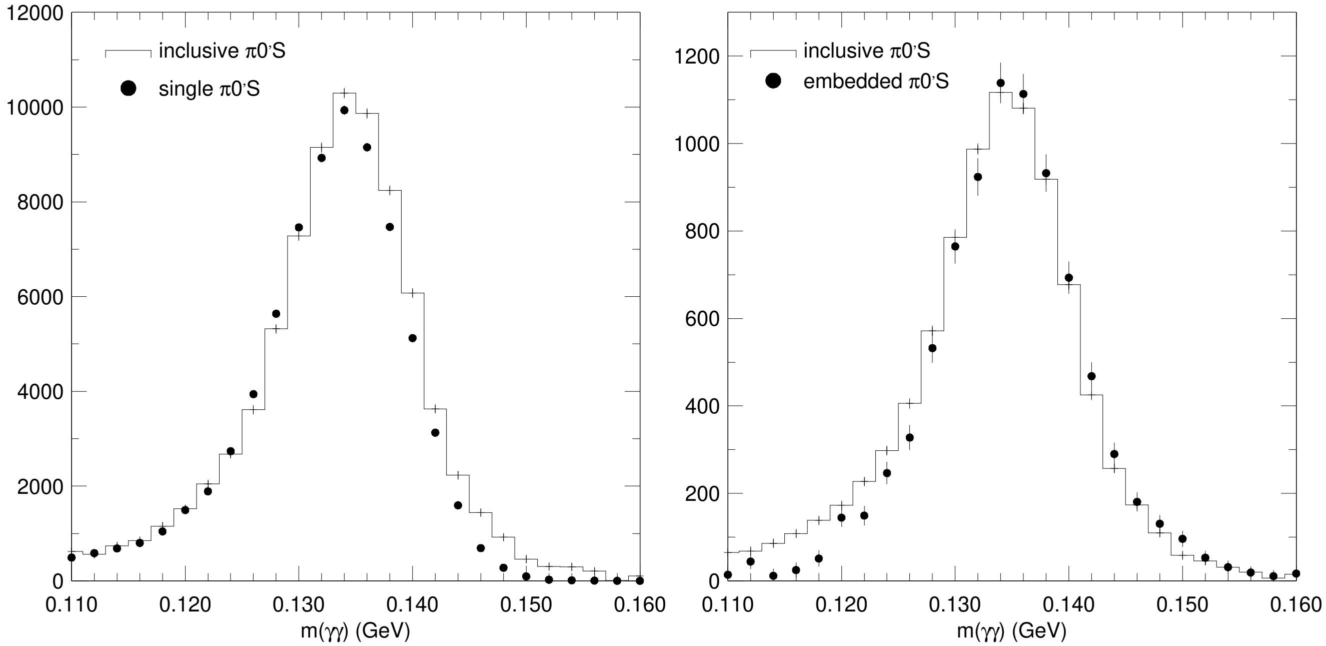

Figure B.20: The left plots shows the $m_{\gamma\gamma}$ distribution for data inclusive π^0's and Modified single π^0's. The right plot shows $m_{\gamma\gamma}$ for data inclusive π^0's and embedded π^0's. The low-side tail of the embedded π^0's is discussed in the text.

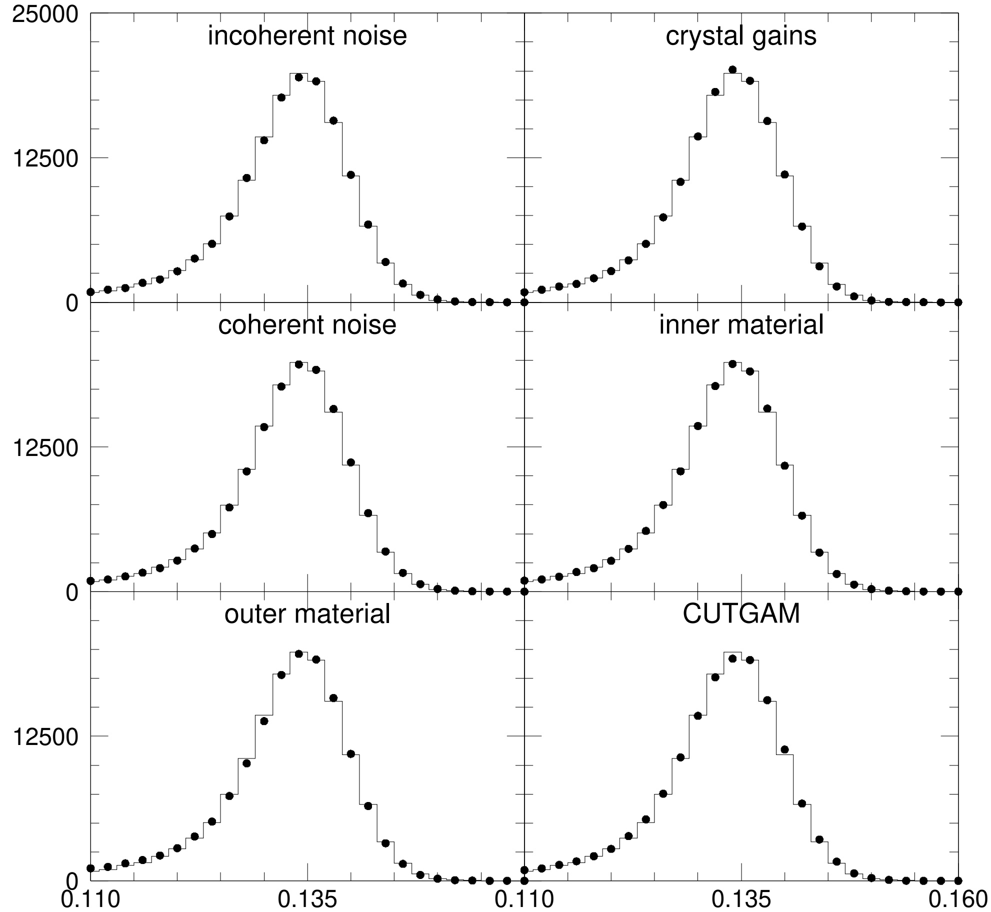

Figure B.21: The change in $m_{\gamma\gamma}$ for the six variations (dots) compared to the Modified Monte Carlo (line) over all π^0 momenta. The plots are made from unembedded π^0's.

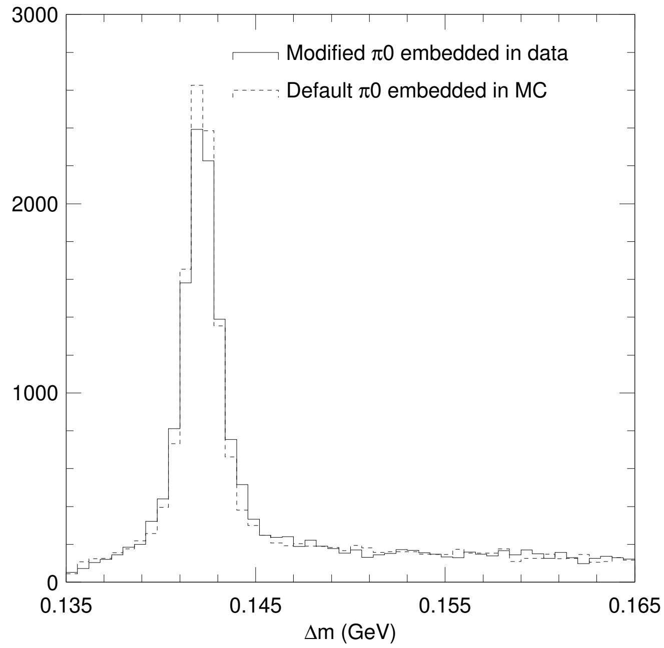

Figure B.22: TheΔm distributions for Modified π^0's embedded in data and Default π^0's embedded in Monte Carlo. The plots are normalized to equal area.

APPENDIX C

BACKGROUND SUBTRACTION FOR INCLUSIVE π^0 $m_{\gamma\gamma}$ DISTRIBUTIONS

The $m_{\gamma\gamma}$ background shape of Monte Carlo is different from that of data, but not radically (see Figure C.1). We postulate that this difference is due entirely to the different number of low-energy showers, an assumption that we will re-evaluate below. If we reweight the fake π^0's from generic Monte Carlo based on their shower energies, the reweighted fake-π^0 $m_{\gamma\gamma}$ distribution from Monte Carlo should look exactly like the fake-π^0 distribution in data. We subtract the reweighted fake-π^0 distribution from the data distribution to get the $m_{\gamma\gamma}$ distribution from real data π^0's. We do this in 10 equal bins of π^0 momentum from 0 to 250 MeV/c.

First, we plot the total number of showers in all events versus energy for data and generic Monte Carlo. The showers must pass all of the cuts listed in Section B.2 with the exception of the $m_{\gamma\gamma}$ and Δm cuts. We subtract continuum background from all data candidates using off-resonance data. These distributions are shown in Figure C.2.

We then normalize the Monte Carlo distribution based on the relative number of $B\overline{B}$'s in the data and generic Monte Carlo samples. This normalization turns

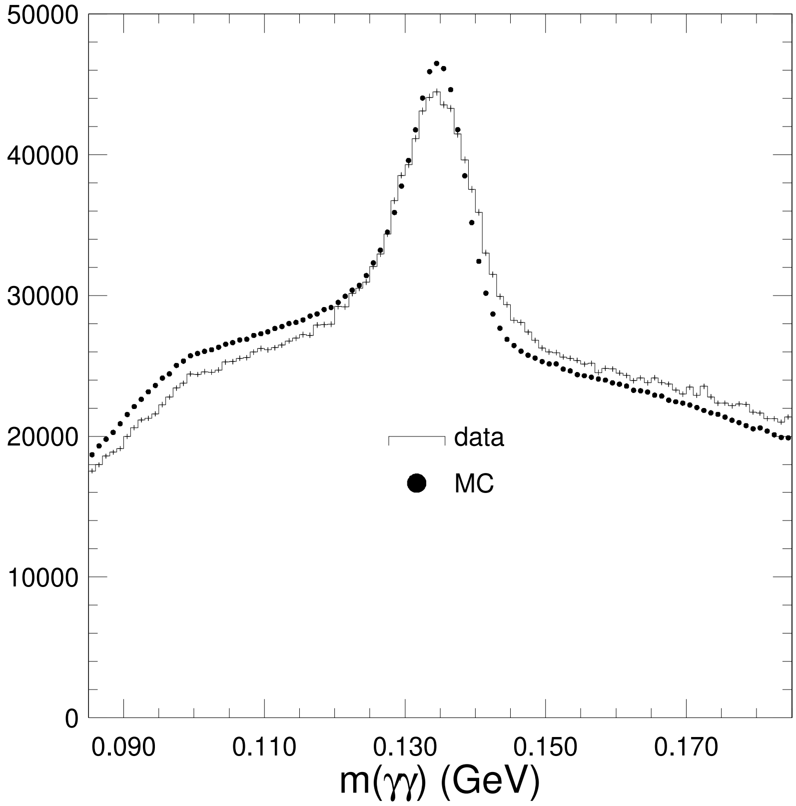

Figure C.1: The $m_{\gamma\gamma}$distributions for all inclusive slow-π^0 candidates from data and Monte Carlo. The plots are normalized to equal areas. The fact that the Monte Carlo is high on the low side and low on the high side implies a different energy spectrum for the Monte Carlo background showers.

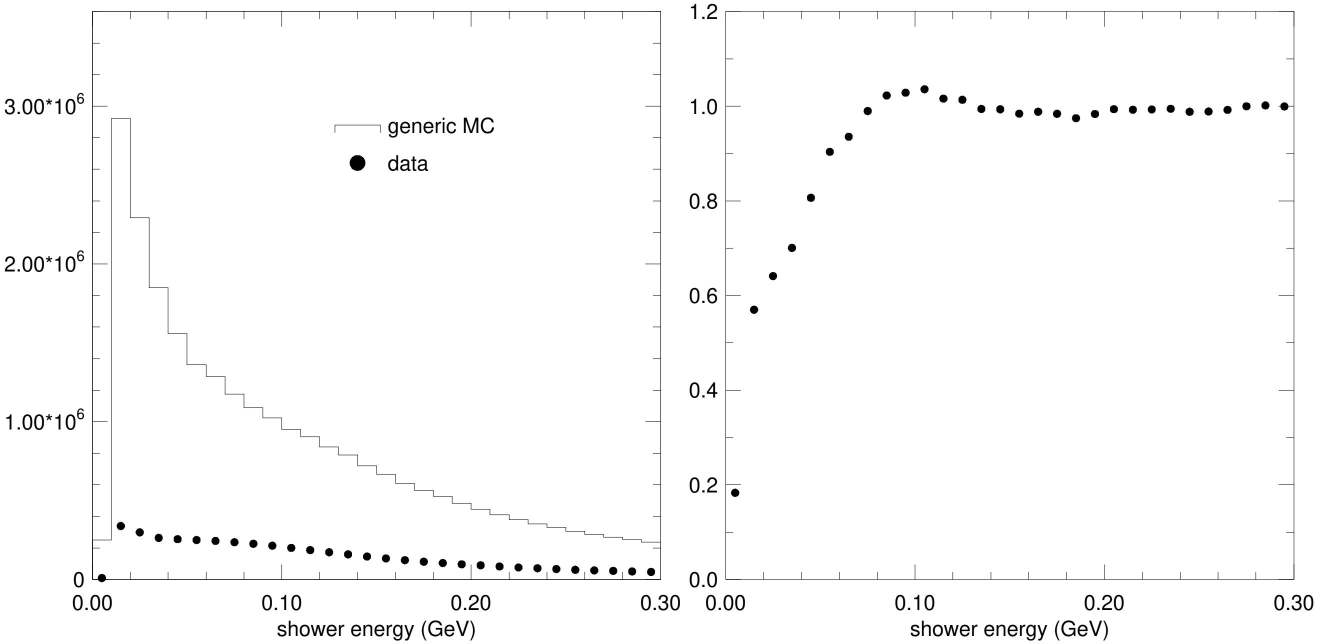

Figure C.2: The left plot shows the distribution of showers in the good barrel region ($|\cos\theta_\gamma| \leq 0.7071$) for data and generic Monte Carlo. The right plot shows the reweighting factors for showers in background π^0's.

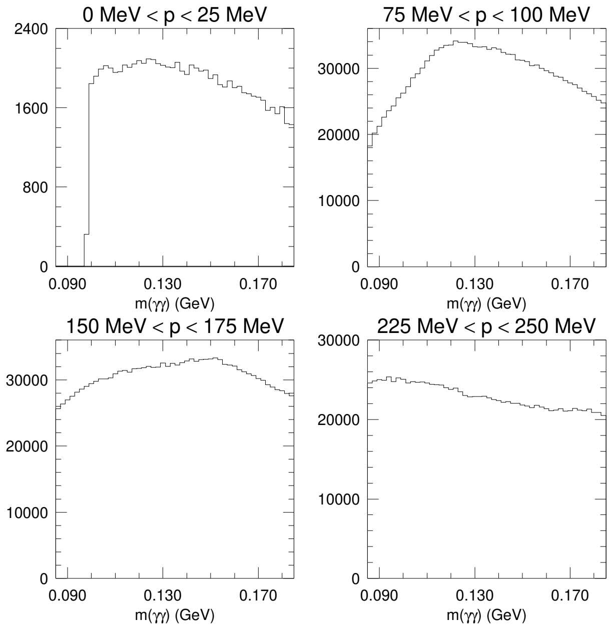

Figure C.3: The $m_{\gamma\gamma}$ shape of the π^0 background from re-weighted generic Monte Carlo for four of the ten momentum bins.

out to be 0.2036$\pm$0.0037, where the uncertainty comes from the 1.8% uncertainty on the number of $B\overline{B}$'s in the data, slightly different than the normalization based on all hadron events (0.192) because of a slight difference in efficiency for passing the event cuts listed above. We divide the data distribution by the renormalized Monte Carlo distribution; the resulting reweighting factors are shown in Figure C.2.

We tag fake π^0's in generic Monte Carlo for the background $m_{\gamma\gamma}$ shape. We re-weight the contribution of each fake π^0 to the $m_{\gamma\gamma}$ distribution by the product of the re-weighting factors for each shower based on its energy. This gives us background $m_{\gamma\gamma}$ distributions, which are shown in Figure C.3.

Figure B.3 shows that the tagged Monte Carlo π^0's do not go much above $0.155\,\mathrm{GeV}/c^2$ in $m_{\gamma\gamma}$. If we use the normalization of 0.2036 for the re-weighted Monte Carlo background, the data $m_{\gamma\gamma}$shape has a considerable tail above $0.155\,\mathrm{GeV}/c^2$ (see Figure C.4), when we have no reason to expect this tail. We instead find the normalization by fitting the background shape over all momenta to the data shape over all momenta in the region $0.155\,\mathrm{GeV}/c^2 \leq m_{\gamma\gamma} \leq 0.185\,\mathrm{GeV}/c^2$. This fit is shown in Figure C.4.

We use the background shapes to subtract the background from the data $m_{\gamma\gamma}$ shapes, shown in Figure C.5. We normalize the backgrounds using the common normalization from the fit to $m_{\gamma\gamma}$. The subtracted shapes are shown compared to the tagged Monte Carlo shapes in Figure C.6.

We have a reason to believe that this method does not do an entirely correct job of subtracting the fake π^0's. The normalization we get from the high-side $m_{\gamma\gamma}$ fit (0.2056 ± 0.0008) and from the number of $B\overline{B}$'s in the data and generic Monte Carlo samples (0.2036 ± 0.0037) agree within uncertainties, so there is no cause for concern there. While we do not expect that the normalization should be a function of π^0 momentum if it only depends on the number of $B\overline{B}$'s, this is exactly what we see. Figure C.7 shows the results of the $m_{\gamma\gamma}$ fit in momentum bins; it is clearly not a flat distribution. This leads us to believe that our assumption that the difference in the $m_{\gamma\gamma}$ background shapes comes solely from a difference in the number of low-energy showers in data and Monte Carlo is not quite correct. We do believe that our background subtraction is accurate to several percent, which is good enough

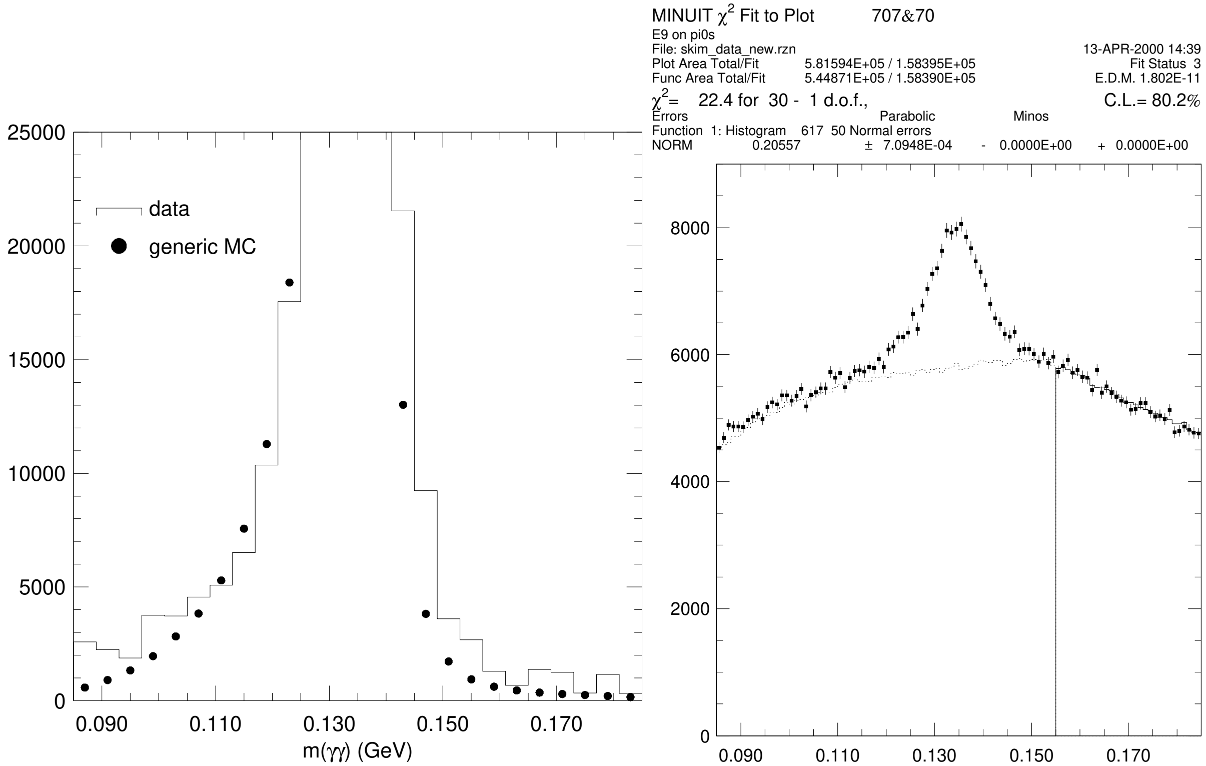

Figure C.4: The left plots shows the $m_{\gamma\gamma}$ distribution for data and Monte Carlo using the normalization from the number of $B\overline{B}$'s. The bin size has been increased to highlight the excess of the data distribution in the region $0.155\,\mathrm{GeV}/c^2 \leq m_{\gamma\gamma} \leq 0.185\,\mathrm{GeV}/c^2$. The right plot shows the fit to the high side of $m_{\gamma\gamma}$ using the data (squares) and the tagged Monte Carlo background (histogram).

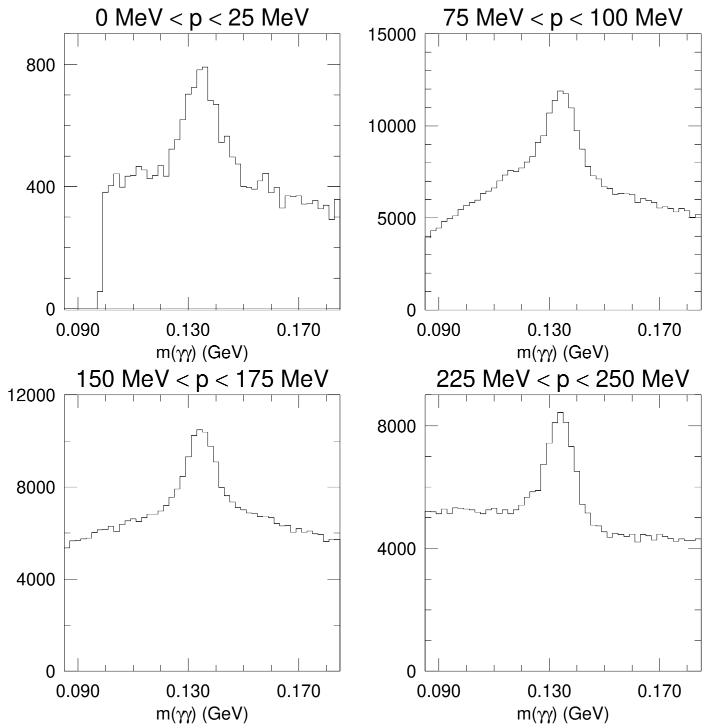

Figure C.5: The $m_{\gamma\gamma}$ shape of the data π^0 candidates for four of the ten momentum bins. Continuum background has been subtracted.

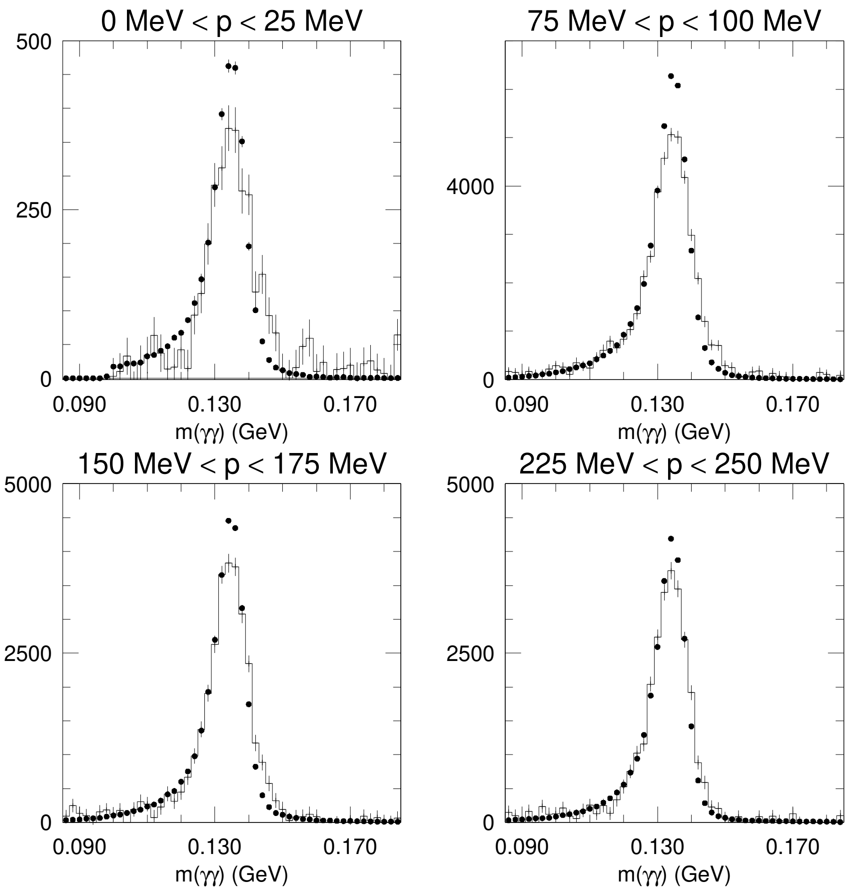

Figure C.6: The $m_{\gamma\gamma}$ shape of data (line) and tagged generic Monte Carlo (dots) π^0's for four of the ten momentum bins.

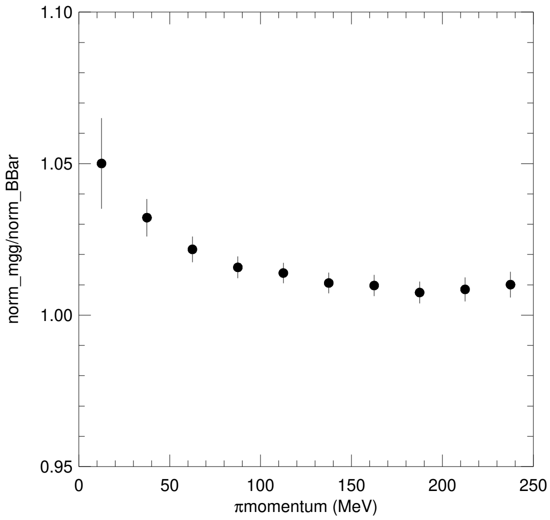

Figure C.7: The ratio of normalizations from fits to $m_{\gamma\gamma}$ in π^0 momentum bins to the normalization from the number of $B\overline{B}$ events.

for the purpose of comparing the $m_{\gamma\gamma}$ shapes, but further development of this background-subtraction technique would be necessary to decrease the uncertainty.

APPENDIX D

APPLYING A TAIL TO THE SINGLE-π^0 E9/E25 DISTRIBUTIONS

We compare the E9/E25 means for generic Monte Carlo inclusive π^0 candidates and single π^0's in Table D.1. Our first step towards adding a tail is to assume that the inclusive-π^0 E9/E25 distribution has a spike from real π^0's of area 100 at the mean E9/E25 value for single-π^0's. (This approach obviously has little to do with what the distribution actually looks like.) We then attribute the difference in means to a spike at 0.8. We calculate the area of this second spike as

$$A_2 = 100\frac{M_s - M_i}{M_i - 0.8}, \tag{D.1}$$

where A_2 is the area of the second spike, M_s is the E9/E25 mean from single-π^0 Monte Carlo, and M_i is the E9/E25 mean from inclusive π^0 Monte Carlo. We then insert this second spike into an imaginary distribution for the modified single π^0 Monte Carlo, which has a spike of area 100 at its measured mean. From that distribution, we can calculate a corrected mean, shown in Table D.2. We compare the corrected mean (M_c) to the inclusive-π^0 mean (M_i) to get the final change in the mean, $M_i - M_c$. These corrected mean changes are plotted in Figure B.10.

Table D.1: The mean values of `E9/E25` calculated for six shower energy bins. The second column gives the range over which the mean was calculated. The third and fourth columns give the means for showers from inclusive generic Monte Carlo slow π^0's and from Default single π^0's, respectively.

Shower Energy (MeV)	`E9/E25` Range	Inclusive π^0	Default Single π^0
30-60	0.80-1.0	0.9284	0.9418
60-90	0.84-1.0	0.9486	0.9552
90-120	0.88-1.0	0.9591	0.9634
120-150	0.90-1.0	0.9645	0.9645
150-180	0.92-1.0	0.9691	0.9716
180-210	0.94-1.0	0.9741	0.9752

Table D.2: The mean of `E9/E25` measured for Modified single π^0's (second column) and corrected using the method in Appendix D.

Shower Energy (MeV)	Modified Single π^0	Corrected Mean
30-60	0.9180	0.9068
60-90	0.9378	0.9319
90-120	0.9508	0.9468
120-150	0.9583	0.9555
150-180	0.9645	0.9621
180-210	0.9689	0.9678

APPENDIX E

SHOWER ENERGY AND $m_{\gamma\gamma}$ CORRECTIONS FOR MODIFIED MONTE CARLO

`CLEOG` is calibrated such that the energy of photons reconstructed in the calorimeter matches their generated energy on average. When we change the calibration constants, as we do when changing the noise levels, or when we change `CUTGAM`, the reconstructed energies become shifted from the generated energies. This shift in shower energies also affects $m_{\gamma\gamma}$. If we ignore this effect, it biases the efficiency for showers passing the shower energy, `E9/E25`,[1] and $m_{\gamma\gamma}$ cuts.

We correct for the shift in shower energy by examining the reconstructed shower energy versus the generated energy for single π^0 events generated with the Modified Monte Carlo and for each variation. We find that, except in the case of the `CUTGAM` variation, the energy shift is consistent with being flat (see Figure E.1). We fit the shift to a constant, which we then use to correct the reconstructed shower energies in the embedded events. In the case of the `CUTGAM` variation, we fit the shift to a line and apply an energy-dependent correction to the shower energies.

[1]The `E9/E25` cut value depends on the shower's energy. The dependence is given in the caption to Figure B.2.

The amounts that we correct the shower energies in the Modified Monte Carlo and the variations are listed in Table E.1.

Since the shower energies change, the peak of $m_{\gamma\gamma}$ also moves. We make a correction similar to the correction to the shower energies, except that we compare the peak of $m_{\gamma\gamma}$ in the Modified Monte Carlo (or variations) to the peak of $m_{\gamma\gamma}$ in the Default Monte Carlo in π^0 momentum bins. We fit the difference versus momentum to a straight line, and use the results of the fit to correct $m_{\gamma\gamma}$ based on the momentum of the π^0 candidate. The normalizations and slopes for the $m_{\gamma\gamma}$ corrections are also listed in Table E.1.

We assess the uncertainty of these corrections by varying the results of each fit (shower energy shift, $m_{\gamma\gamma}$ peak difference) by its statistical uncertainty. We also try correcting $m_{\gamma\gamma}$ in momentum bins instead of using the fit. We find that each change to the correction makes less than 0.1% difference in the resulting Modified-Default efficiency difference. We neglect these uncertainties, since they are at least an order of magnitude smaller than any statistical uncertainty in our study.

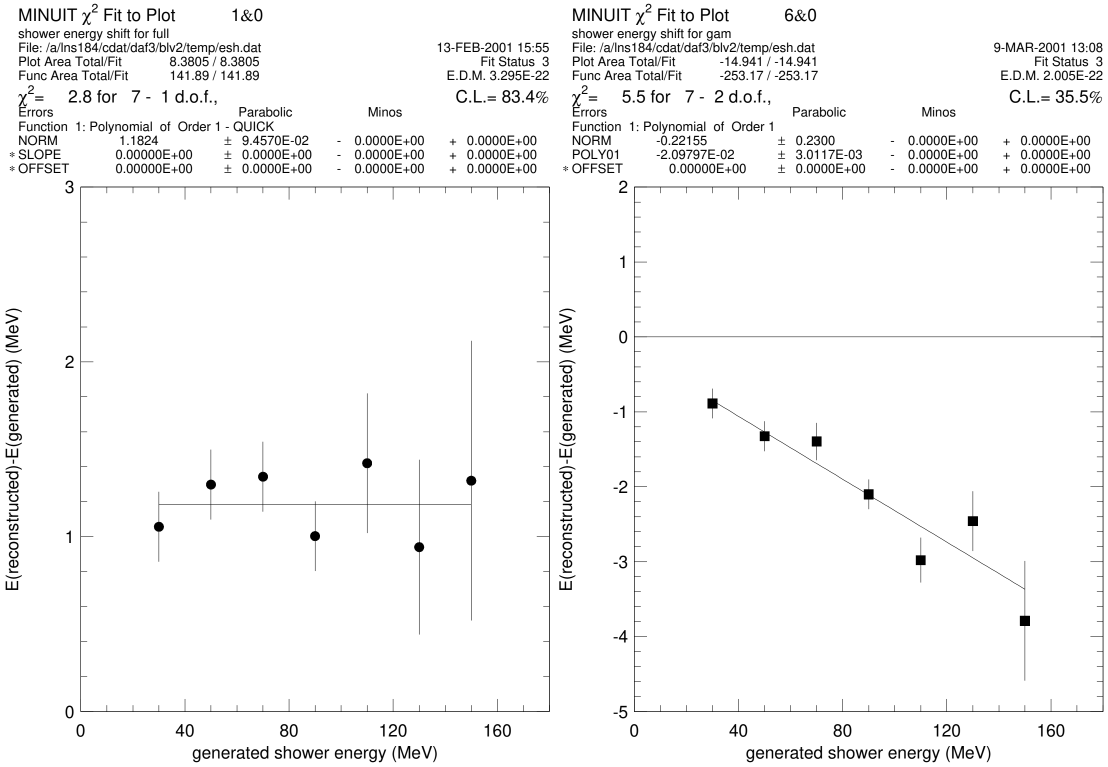

Figure E.1: The left plot shows a fit to the shift in shower energy versus generated shower energy for the Modified Monte Carlo. The right plots shows the shift versus shower energy for the `CUTGAM` variation.

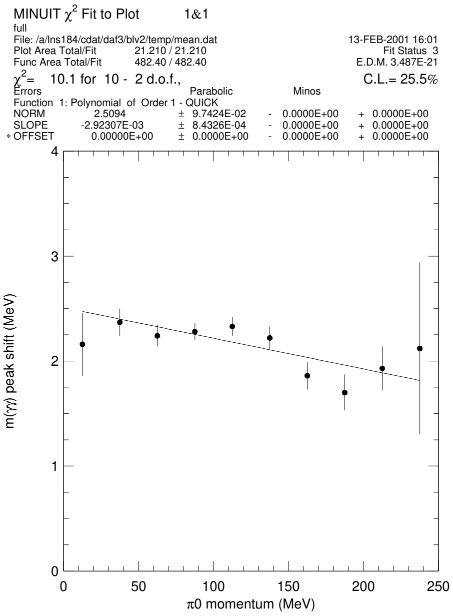

Figure E.2: The fit to the shift in the $m_{\gamma\gamma}$ peak versus π^0 momentum between the Modified and Default Monte Carlos.

Table E.1: The constants used to correct the shower energies and $m_{\gamma\gamma}$ in the Modified Monte Carlo and the variations. The second column gives the correction to the reconstructed shower energy for the variation listed in the first column. The third and fourth columns give the normalizations and slopes of the line fits for the $m_{\gamma\gamma}$ correction (input momentum in MeV/c, get correction in MeV). We use the same corrections for Modified and inner material reconstruction. The `CUTGAM` variation introduces an energy-dependent shift to the reconstructed shower energy; we fit this shift to a straight line and make an energy-dependent correction to the shower energies.

Variation	Shower Energy Correction (MeV)	$m_{\gamma\gamma}$ Norm (MeV)	$m_{\gamma\gamma}$ Slope ($\times 10^{-3}$)
Modified	1.182±0.095	2.513±0.098	-2.97±0.85
incoherent noise	1.142±0.098	3.182±0.098	-6.20±0.85
crystal gains	1.055±0.092	2.917±0.098	-6.02±0.85
coherent noise	1.113±0.096	2.332±0.098	-2.96±0.85
inner material	1.182±0.095	2.513±0.098	-2.97±0.85
outer material	1.107±0.092	2.547±0.098	-6.01±0.85
`CUTGAM`	$norm{:}-0.22\pm0.23$ $slope{:}-2.10\pm0.30\times10^{-2}$	-2.725±0.098	0.68±0.0.85

REFERENCES

[1] D.E. Groom *et al.*, The European Physical Journal **C15** (2000) 1.

[2] N. Cabibbo, Phys. Rev. Lett. **10**, 531 (1963); M. Kobayashi and T. Maskawa, Prog. Theor. Phys. **49**, 652 (1973).

[3] L. Wolfenstein, Annu. Rev. Nucl. Part. Sci. **36**, 137 (1986).

[4] J.D. Richman and P.R. Burchat, Rev. Mod. Phys. **67** (1995) 893.

[5] P. Drell, Invited Talk at the XVIII International Symposium on Lepton-Photon Interactions, CLNS 97/1521.

[6] BaBar Physics Book, PF Harrison and HR Quinn, editors, SLAC-R-504 (1998).

[7] M. Neubert, Physics Reports, **245**, 259 (1994).

[8] J.G. Körner and G.A. Schuler, Z. Phys. C 38 (1988) 511.

[9] N. Isgur and M.B. Wise, Phys. Lett. **B232**, 113 (1989); Phys. Lett. **B237**, 527 (1990).

[10] I Caprini,L Lellouch and M Neubert, Nucl. Phys. B **530**, 153 (1998) (hep-ph/9712417).

[11] C.G. Boyd, B. Grinstein, and R.F. Lebed, Nucl. Phys. B **461**, 493 (1996); Phys. Rev. **D56**, 6895 (1997) (hep-ph/9705252).

[12] J. Duboscq *et al.*(CLEO Collaboration) Phys. Rev. Lett. **76**, 3898 (1996).

[13] M.E. Luke, Phys. Lett. **B252**, 447 (1990).

[14] D. Andrews *et al.*, Phys. Rev. Lett. **44**, 1108 (1980); T. Bohringer *et al.*, Phys. Rev. Lett. **44**, 1111 (1980).

[15] D. Andrews *et al.*, Phys. Rev. Lett. **45**, 219 (1980); C. Finocchario *et al.*, Phys. Rev. Lett. **45**, 222 (1980).

[16] JP Alexander *et al.*(CLEO Collaboration), CLNS 00/1670 (2000).

[17] D. Atwood and W. Marciano, Phys. Rev. **D41**, 1736 (1990).

[18] G Fox and S Wolfram, Phys. Rev. Lettt. **41**, 1581 (1978).

[19] Y. Kubota *et al.* (CLEO Collaboration), Nucl. Instrum. Methods Phys. Res., Sect. A **320**, 66 (1992).

[20] SE Csorna *et al.*(CLEO Collaboration), Phys. Rev. D **61**, 111101 (2000)(hep-ex/0001013).

[21] K. Berkelman, CBX 95-342.

[22] S. Roberts *et al.*, CBX 96-103.

[23] R. Kutschke and A. Ryd, CBX 96-20

[24] B.K. Heltsley, CBX 92-108.

[25] Some analyses "reconstruct" the neutrino by attributing any unmeasured energy in an event to the neutrino; see for example K. Bloom *et al.*, CBX 97-21.

[26] B. Gittelman, C. O'Grady, and M. Sapper, CBX 91-82.

[27] T. Skwarnicki, CSN 90-301; T. Haupt, CBX 91-78.

[28] R. Brun *et al.*, GEANT 3.15, CERN DD/EE/84-1.

[29] E Barberio and Z Was, Comput. Phys. Commun. **79**, 291 (1994).

[30] JL Goity and W Roberts, Phys. Rev. D **51**, 3459 (1995).

[31] D Scora and N Isgur, Phys. Rev. D **52**, 2783 (1995); N Isgur *et al.*, Phys. Rev. D **39**, 799 (1989).

[32] SE Csorna *et al.*(CLEO Collaboration), Phys. Rev. D **61**, 111101 (2000)(hep-ex/0001013).

[33] V. Fadeyev and R. Stroynowski, CBX 00-43.

[34] Routine HMCLNL, described in the HBOOK manual(CERN); Roger Barlow and Christine Beeston, Comp. Phys. Comm. **77**, 219 (1993).

[35] B Barish *et al.* (CLEO Collaboration), Phys. Rev. Lett. **76**, 1570 (1996).

[36] BH Behrens *et al.*(CLEO Collaboration), CLNS 00/1668.

[37] T. Riehle and R. Poling, to be published as a CBX note.

[38] D.S. Akerib *et al.* (CLEO Collaboration), Phys. Rev. Lett. **71**, 3070 (1993).

[39] R. Barate *et al.* (ALEPH Collaboration) Phys. Lett. **B403**, 367 (1997).

[40] Monte Carlo study by Karl Ecklund.

[41] The variation is based on a discussion with Roy Briere.

[42] B Barish *et al.*(CLEO Collaboration), Phys. Rev. **D 51**, 1014 (1995).

[43] Based on a discussion with Jesse Ernst.

[44] B. Heltsley *etal.*, CBX 95-35. See endnote number 18.

[45] This work was done by the Cornell Electron ID Group.

[46] B. Berger, CBX 00-32.

[47] J. Urheim, CBX 99-53.

[48] Dave Besson, electronic mail to CLEO collaboration.

[49] A. Anastassov *et al.* (CLEO Collaboration), Phys. Rev. Lett. **80**, 4127 (1998); D. Buskulic *et al.* (ALEPH Collaboration), Z. Phys. C **73**, 601 (1997); D. Buskulic *et al.* (ALEPH Collaboration), Phys. Lett. **B345**, 103 (1995).

[50] K. Ecklund, B. Valant-Spaight, B. Berger, R. Patterson, CBX 2001 (number to be assigned).

[51] S. Stone, "Probing the CKM Matrix with b decays" in *Proceedings of the Albuquerque Meeting*, ed. S. Seidel, World Scientific, Singapore (1994), p. 871.

[52] From the Winter 2001 averages of the LEP $|V_{cb}|$ Working Group, `http://lepvcb.web.cern.ch/LEPVCB`.

[53] A. K. Leibovich *et al.*, Phys. Rev. **D57**, 308 (1998).

[54] J. Bartlett /etal/ (CLEO Collaboration), Phys. Rev. Lett. **82**, 3746 (1999).

[55] Albrecht *et al.* (ARGUS Collaboration), Phys. Lett. **B275**, 195 (1992).

[56] S. Weinberg, Phys. Rev. Lett. **49**, 652 (1973).

[57] See `http://www.lns.cornell.edu/~bkh/cc4s9AFix.html`. The run range we exclude is 59630-61778.